YUKAWA INSTITUTE FOR THEORETICAL PHYSICS

DOCTORAL THESIS

Lattice QCD studies on baryon resonances and pentaquarks from meson-baryon scatterings

---

Author: Kotaro Murakami

A thesis submitted in fulfillment of the requirements for the degree of Doctor of Science

in the

Department of Physics
Kyoto University

December 21, 2022

Abstract

In this thesis, motivated by the advantage of the HAL QCD method among the approaches using lattice QCD for systems involving baryons, we attempt to study baryon resonances and pentaquarks in the HAL QCD method. To this end, we analyze meson-baryon scatterings that have quark pair creation and annihilation processes, where we need to calculate all-to-all propagators. We utilize the calculation technique that combines the stochastic approximation with the covariant-approximation averaging (CAA), which has been suggested to be efficient in the HAL QCD method. We calculate the leading-order (LO) potentials in the derivative expansion using the time-dependent HAL QCD method and then extract physical observables by solving the Schrödinger equations with the potentials.

We first investigate the S-wave nucleon-kaon (NK) scatterings, which allow no quark pair creation and annihilation, as a test of the efficiency of the technique for meson-baryon systems. We employ all-to-all propagators to put the zero momentum hadron operators both at source and sink and then use the one-end trick and the CAA. In this study, the pion mass $m_\pi \approx 570$ MeV. We have observed that the $I = 1$ potential is more repulsive than the $I = 0$. The scattering phase shifts are qualitatively consistent with both the experimental data and the previous theoretical results, which suggests that the calculation technique in this work is useful for meson-baryon scatterings in the HAL QCD method. Furthermore, we have found no signals of resonances or bound states corresponding to $\Theta^+(1540)$ in the phase shifts at $m_\pi \approx 570$ MeV.

We next study Δ and Ω baryons from $I = 3/2$ nucleon-pion ($N\pi$) and $I = 0$ Ξ baryon-antikaon ($\Xi\bar{K}$) scatterings, respectively. This is the first study on meson-baryon scatterings having the quark pair creation and annihilation in the HAL QCD method. We use a 3-quark-type source operator with zero momentum at $m_\pi \approx 410$ MeV and $m_K \approx 635$ MeV, where Δ as well as Ω baryons are stable. We use the conventional stochastic technique combined with the CAA for the calculation of all-to-all propagators. We have found that the $\Xi\bar{K}$ system has a weaker attraction than the $N\pi$ system while the binding energy from the threshold is larger for Ω than for Δ. In addition, the root-mean-square distance of $\Xi\bar{K}$ bound state is smaller than that of $N\pi$. These suggest that an inequality $m_N + m_\pi - m_\Delta < m_\Xi + m_{\bar{K}} - m_\Omega$ comes mainly from a smaller spatial size of a $\Xi\bar{K}$ bound state due to a larger reduced mass, rather than its interaction. Results of binding energies agree with those obtained from temporal 2-point functions within large systematic errors, which are mainly caused by the lattice artifact at short distances.

We finally show the preliminary analysis of S-wave meson-baryon scatterings in the two octet representations and one singlet representation in the flavor SU(3) limit, which have been suggested to couple to $\Lambda(1405)$ in the previous studies using the chiral unitary model. We calculate an all-to-all propagator to employ a 3-quark-type source operator with zero momentum, using the conventional stochastic technique together with the CAA. The octet meson mass $m_M \approx 670$ MeV in our setup. We have found that the 3-point correlation functions have a zero point in a short distance, which leads to a singular behavior of the LO potentials. The ground state in every channel seems to be unphysical and may be raised by the singular potential. One possible reason for such problematic behavior is that the NBS wave function has a $1/r^3$ behavior in a very short distance together with analytic behavior in a middle and a long distance with opposite signs to each other. To overcome this problem, we should calculate the 4-point correlation function in addition to the 3-point to suppress the $1/r^3$ behavior, which is left for our future works.

Contents

List of Publications

Papers related to the thesis

1. Kotaro Murakami, Yutaro Akahoshi, Sinya Aoki,
   S-wave kaon–nucleon potentials with all-to-all propagators in the HAL QCD method,
   PTEP **2020**, no.9, 093B03 (2020).

Chapter 1

Introduction

A number of hadrons, which are composed of quarks and gluons, have been discovered until today. Since the quarks and gluons are described by Quantum chromodynamics (QCD), which is the Yang-Mills theory [1] with SU(3) gauge symmetry, it is supposed to predict the existence and properties of all hadrons. However, understanding QCD in a low-energy region, where the confinement of quarks occurs and hadrons are constructed, is difficult because QCD is asymptotically free [2, 3] and the perturbation technique cannot be applied.

Instead, hadrons have been studied by effective models of QCD such as the quark model [4–6], which describes hadrons as bound states of constituent quarks, and the chiral perturbation theory (ChPT) [7], which is the low-energy effective field theory that has the same degree of freedoms as those of hadrons. The quark model characterizes most hadrons as mesons or baryons, which are composite particles of a quark and an antiquark ($q\bar{q}$) and three quarks (qqq), respectively, although QCD itself also allows n-quark hadrons with $n \geq 4$. Several recent experiments have discovered hadrons that cannot be predicted by the ordinary quark model, called exotic hadrons [8]. They are the candidates of 4-quark hadrons ($qq\bar{q}\bar{q}$) called tetraquarks or 5-quark hadrons ($qqq\bar{q}\bar{q}$), called pentaquarks. There are various approaches both on the theoretical and experimental sides to studying exotic hadrons, but they are still controversial. With this situation, exploring exotic hadrons is one of the biggest issues in hadron physics.

Lattice QCD [9] is one of the possible non-perturbative calculations of QCD and has successfully predicted the dynamics of hadrons. For example, it provides the spectrum of light hadrons consistent with the experimental results [10, 11]. The lattice QCD studies of exotic hadrons as well as hadron resonances from the corresponding hadron scatterings play a very important role in understanding their properties and predicting other exotic hadrons that have never been found in experiments.

There are two available methods to analyze hadron scatterings in lattice QCD; one is the finite-volume method [12, 13], which relates energies on finite volume(s) to scattering amplitudes on the infinite volume, and the other is the HAL QCD method [14–16], which extracts interaction potentials directly in lattice QCD and then obtain scattering amplitudes from potentials by solving the Schorödinger equations in the infinite volume. Many studies in the finite-volume method have been conducted on meson-meson scatterings such as $\pi\pi$ scattering which couples to ρ resonance [17], while its application to systems including baryons is quite challenging due to the difficulty of isolating a specific eigenstate of the system [18]. On the other hand, the time-dependent HAL QCD method [16] can reduce this difficulty. For this reason, various kinds of studies on baryon-baryon scatterings in the HAL QCD method have been performed so far (for a recent review, see Ref. [19]).

In nature, hadron resonances and part of exotic hadrons are often observed in the scatterings which allow quark pair creation and annihilation processes. Studying such scatterings in lattice QCD requires all-to-all propagators, which are too time-consuming to calculate exactly, and

therefore are evaluated approximately. The first attempt at the study of resonances in the HAL QCD method is the investigation of the ρ resonance from P-wave $I = 1$ $\pi\pi$ scatterings using the LapH method [20], which has found that the technique is not applicable because it worsens the truncation approximation of the derivative expansion of the non-local potential. There is also work for the same scattering system which employs the hybrid method [21], concluding that this is not useful in the HAL QCD method due to its large fluctuation coming from the noise vectors. Recently, Akahoshi et al. proposed an improved calculation technique for all-to-all propagators to avoid these difficulties as much as possible, in which they use the one-end trick combined with the covariant-approximation averaging (CAA). The authors also applied it to the P-wave $I = 1$ $\pi\pi$ scatterings [22], and then extracted the signal of the ρ resonance successfully. This work plays a role in opening a new frontier of the studies on meson resonances and tetraquarks using the HAL QCD method, which, together with the studies in the finite-volume method, will develop the understanding of their properties.

In our studies, towards the researches of baryon resonances and pentaquarks, we try to analyze meson-baryon scatterings having quark pair creation and annihilation using a similar technique to Ref. [22]. Since the HAL QCD method is advantageous compared with the finite-volume method in that it can avoid the problem due to the existence of a baryon, it is worth analyzing such scattering systems from the approach of the HAL QCD method. As a first step, we investigate the $S = +1$ S-wave nucleon-kaon (NK) scatterings, which allow no quark pair creation and annihilation. This study has the aspect of a test of the efficiency of the technique for the meson-baryon systems. We employ all-to-all propagators together with the one-end trick and the CAA as a calculation technique for the propagators. Thanks to the all-to-all propagators, we can use the hadron operators with zero momenta at both source and sink together with the smeared quark operators at the source in this study.

The next study in this thesis is the analysis of P-wave $I = 3/2$ nucleon-pion ($N\pi$) and $I = 0$ Ξ baryon-antikaon ($\Xi\bar{K}$) scatterings, which couple to Δ and Ω baryons, respectively. This is the first study on meson-baryon scatterings having the quark pair creation and annihilation in the HAL QCD method. In order to reduce computational costs, we employ the heavy quark masses, where u, d quark masses are close to the s quark mass. In this case, Δ baryon exists as a stable particle as well as Ω, which is more or less far from the situation in nature. We use a 3-quark-type source operator with zero momentum, which requires an all-to-all propagator, and then employ the conventional stochastic technique together with CAA.

Furthermore, in this thesis, we show the preliminary study on $\Lambda(1405)$, one of the exotic hadrons, in the flavor SU(3) limit. As is the case of the analysis of the $N\pi$ and $\Xi\bar{K}$ scatterings, we introduce an all-to-all propagator to use a 3-quark-type source operator with zero momentum, and then we employ the conventional stochastic technique together with CAA.

This thesis is organized as follows. In Chapter 2, we define the lattice QCD theory and review how to calculate the correlation functions in lattice QCD. Then in Chapter 3, we derive an asymptotic behavior of the Nambu-Bethe-Salpeter wave function and introduce the HAL QCD method. In Chapter 4, we express the all-to-all propagator techniques that we use in our studies: the stochastic estimation and the one-end trick, and then explain the covariant approximation averaging, which is an efficient method to increase statistics. We show our studies of S-wave NK scatterings in Chapter 5, and P-wave $N\pi$ and $\Xi\bar{K}$ scatterings in Chapter 6. In Chapter 7, we present our preliminary study on meson-baryon scatterings to study $\Lambda(1405)$ in flavor SU(3) limit. Chatper 8 is devoted to the summary and discussion.

Chapter 2

Lattice QCD

In this chapter, we review the general aspects of lattice QCD. We first define QCD theory in continuous spacetime, and then we construct the discretized action of the gauge fields followed by that of the fermion fields. After that, we introduce the path-integral formula of general correlation functions in lattice QCD and their calculations and then explain several variations of fermion operators. For the notation and derivation in this chapter, we refer to Ref. [23].

2.1 QCD in continuum

In this thesis, we consider the QCD theory of Euclidean spacetime.

QCD is a quantum field theory describing quarks and gluons. The quark field is represented by the Dirac fermions $\psi^{(f)}_{a,\alpha}(x)$, $\bar{\psi}^{(f)}_{a,\alpha}(x)$, the gluon field is represented by the gauge field $(A_\mu)_{ab}(x)$. Here, we represent the subscripts as follows.

- $\alpha = 1, 2, 3, 4$: spinor index,
- $a, b = 1, 2, 3$: color index,
- $f = 1, 2, 3 \cdots N_f$: index for the quark flavor,
- $\mu = 1, 2, 3, 4$: index for the spacetime direction.

In this thesis, we take summation over the same subscript appearing in the equation. Although we take $N_f = 6$ in the Standard Model, it is sufficient to consider only light quarks ($N_f = 2$ or $N_f = 3$, etc.) in low-energy regions. Furthermore, we show the fermion fields with the specific flavor instead of $\psi^{(f)}_{a,\alpha}(x)$ as, for example, $u_{a,\alpha}(x)$ for the up quark, $d_{a,\alpha}(x)$ for the down quark, $s_{a,\alpha}(x)$ for the strange quark.

The QCD action in continuous spacetime is defined by

$$\begin{aligned} S &= S_F[\psi, \bar{\psi}, A] + S_G[A], \\ S_F[\psi, \bar{\psi}, A] &= \sum_{f=1}^{N_f} \int d^4x \, \bar{\psi}^{(f)}(x)(\gamma_\mu D_\mu(x) + m^{(f)})\psi^{(f)}(x), \\ S_G[A] &= \frac{1}{2g^2} \int d^4x \, \mathrm{tr}[F_{\mu\nu}(x)F_{\mu\nu}(x)]. \end{aligned} \tag{2.1}$$

Here, $m^{(f)}$ is the quark mass, g is the coupling constant of the gauge field, and $D_\mu(x)$ and $F_{\mu\nu}(x)$ are given by

$$\begin{aligned} D_\mu(x) &= \partial_\mu + iA_\mu(x), \\ F_{\mu\nu}(x) &= -i[D_\mu(x), D_\nu(x)] = \partial_\mu A_\nu(x) - \partial_\nu A_\mu(x) + i[A_\mu(x), A_\nu(x)]. \end{aligned} \tag{2.2}$$

Also, $\mathrm{tr}[\cdot]$ in $S_G[A]$ denotes the trace in the color space. γ_μ is the gamma matrix in the Euclidean spacetime satisfying the following equation:

$$\{\gamma_\mu, \gamma_\nu\} = 2\delta_{\mu\nu}\mathbf{1}. \tag{2.3}$$

The action Eq. (2.1) is invariant under the gauge transformation given by

$$\begin{aligned} \psi(x) \to \psi' &= \Omega(x)\psi(x), \\ \bar{\psi}(x) \to \bar{\psi}' &= \bar{\psi}(x)\Omega(x)^\dagger, \\ A_\mu(x) \to A'_\mu(x) &= \Omega(x)A_\mu(x)\Omega(x)^\dagger + i(\partial_\mu\Omega(x))\Omega(x)^\dagger, \end{aligned} \tag{2.4}$$

where $\Omega(x)$ is the SU(3) gauge transformation matrix.

2.2 QCD action on lattice

We formulate the QCD action on the discretized spacetime which satisfies the following criteria.

- In the continuous limit ($a \to 0$ for the lattice spacing), the lattice action becomes the continuous one.
- The lattice action is Hermitian.
- The lattice action has the same symmetry as that in continuum. If it cannot, it is instead supposed to have an approximate symmetry which becomes the continuous one in the continuum limit.

The first two are obviously necessary. For the third one, the gauge symmetry can be requested on a lattice while the rotation symmetry of spacetime cannot be defined. Thus the symmetry of swapping the two axes is instead requested. We note that the lattice QCD action is not determined uniquely by the above request.

2.2.1 Gauge action on lattice

Gauge field on lattice

First, we note that we cannot introduce a gauge field on a lattice in the same way as that in continuous spacetime. This is because the gauge fields in continuous spacetime are associated with the transformation of the internal degrees of freedom for the Dirac fermions $\psi^{(f)}_{a,\alpha}(x)$ under the infinitesimal translations in spacetime, which cannot be defined on a lattice. Instead, we define gauge fields on the lattice as transformation matrices under the translation by the smallest unit a. That is, we define $(U_\mu)_{cb}(x)$ such that $(U^\dagger_\mu)_{ab}(x)\psi^{(f)}_{b,\alpha}(x)$ transforms in the same way

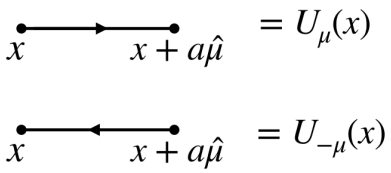

FIGURE 2.1: Graphical representation of the link variables.

as that of $\psi^{(f)}_{a,\alpha}(x + a\hat{\mu})$ under gauge transformation. Thus the gauge transformation of such variables is given by

$$U_\mu(x) \to \Omega(x) U_\mu(x) \Omega^\dagger(x + a\mu). \tag{2.5}$$

The field $U_\mu(x)$ is called a linked variable. On the lattice embedded in continuous spacetime, it can be represented as a Wilson line along a straight line from x to $x + a\hat{\mu}$ as

$$U_\mu(x) = P \exp\left(i \int_x^{x+a\hat{\mu}} A \cdot ds \right), \tag{2.6}$$

where P denotes the path-order product. When a is sufficiently small, we have the behavior of the link variable in the continuum limit $a \to 0$ as

$$U_\mu(x) \approx \exp(iaA_\mu(x)) + \mathcal{O}\left(a^2\right). \tag{2.7}$$

For convenience, we introduce the link variable in the negative direction $U_{-\mu}(x)$ as

$$U_{-\mu}(x) = U_\mu(x - a\hat{\mu})^\dagger, \tag{2.8}$$

which transforms under the gauge transformation as

$$U_{-\mu}(x) \to \Omega(x) U_{-\mu}(x) \Omega^\dagger(x - a\mu). \tag{2.9}$$

We represent the link variables graphically in Figure 2.1.

Wilson gauge action

We construct the lattice gauge action using the link variable $U_\mu(x)$. First, we define the following variable:

$$U_{\mu\nu}(x) = U_\mu(x) U_\nu(x + a\hat{\mu}) U_{-\mu}(x + a\hat{\mu} + a\hat{\nu}) U_{-\nu}(x + a\hat{\nu}), \tag{2.10}$$

called the plaquette variable. This is shown graphically in Fig. 2.2. The Wilson gauge action [9] is defined as

$$S_G[U] = \frac{2}{g^2} \sum_x \sum_{\mu<\nu} \mathrm{Re}(\mathrm{tr}[\mathbf{1} - U_{\mu\nu}(x)]). \tag{2.11}$$

This is invariant under the gauge transformation because the trace of the plaquette variable is invariant. The Wilson gauge action is also Hermitian and symmetric with respect to the swapping of the axes in the spacetime. Furthermore, when a is small enough, using Eq. (2.7), the action

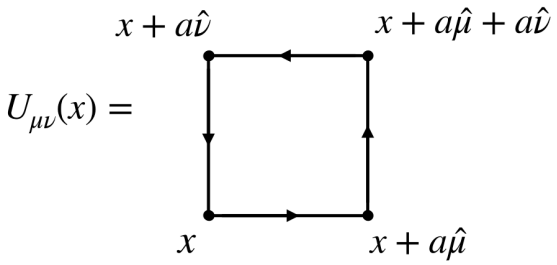

FIGURE 2.2: Diagrammatic picture of the plaquette.

reads

$$\begin{aligned} S_G[U] &= \frac{a^4}{2g^2}\sum_x\sum_{\mu,\nu}\mathrm{tr}[(F_{\mu\nu}(x))^2] + o(a^5) \\ &\underset{a\to 0}{\to} \frac{1}{2g^2}\int d^4x\ \mathrm{tr}[F_{\mu\nu}(x)F_{\mu\nu}(x)], \end{aligned} \tag{2.12}$$

which is the same as that in continuous spacetime.

2.2.2 Fermion action on lattice

Naive fermion action

We first consider a naive discretization of the fermion action in continuous spacetime. Here, we assume $N_f = 1$ for simplicity.

Changing the integral to the summation and the derivatives to the difference, we get the free fermion action. We then obtain the action with the interaction by inserting a link variable $U_\mu(x)$ between the two fermions so that the action is gauge invariant. The explicit form is described as

$$S_F[\psi,\bar{\psi},U] = a^4\sum_x\ \bar{\psi}(x)\Big(\sum_\mu \gamma_\mu \frac{U_\mu(x)\psi(x+a\hat{\mu}) - U_{-\mu}(x)\psi(x-a\hat{\mu})}{2a} + m\psi(x)\Big). \tag{2.13}$$

This satisfies the requirements that we impose for the QCD action as well as the gauge action. However, as seen later, a "prescription" for this action is necessary to describe physics in continuous spacetime properly.

Fermion doubler problem

From the following, we describe the fermion action as

$$S_F[\psi,\bar{\psi},U] = a^4\sum_{x,y}\ \bar{\psi}_{a,\alpha}(x)D(x|y)^{\alpha\beta}_{ab}\psi_{b,\beta}(y), \tag{2.14}$$

where $D(x|y)^{\alpha\beta}_{ab}$ is called the Dirac operator. For the naive fermion action, it is given by

$$D(x|y)^{\alpha\beta}_{ab} = \sum_{\mu}(\gamma_\mu)_{\alpha\beta}\frac{(U_\mu)_{ab}(x)\delta_{x+a\hat{\mu},y} - (U_{-\mu})_{ab}(x)\delta_{x-a\hat{\mu},y}}{2a} + m\delta_{ab}\delta_{\alpha\beta}\delta_{x,y}. \tag{2.15}$$

For simplicity, we consider the free fermion ($U_\mu(x) = 1$). The discrete Fourier transformation for the Dirac operator gives

$$\begin{aligned}\tilde{D}(p|q) &= \frac{1}{|\Lambda|^4}\sum_{x,y} e^{-ip\cdot x}D(x|y)e^{iq\cdot y} \\ &= \frac{1}{|\Lambda|^4}\sum_{x} e^{-i(p-q)\cdot x}\Big(\sum_{\mu}\gamma_\mu\frac{e^{iq_\mu a} - e^{-iq_\mu a}}{2a} + m\mathbf{1}\Big) \\ &= \delta_{p,q}\tilde{D}(p),\end{aligned} \tag{2.16}$$

where

$$\tilde{D}(p) = m\mathbf{1} + \frac{i}{a}\sum_{\mu}\gamma_\mu\sin(p_\mu a). \tag{2.17}$$

Thus the inverse of the Dirac operator is given by

$$\tilde{D}^{-1}(p) = \frac{m\mathbf{1} - \frac{i}{a}\sum_\mu \gamma_\mu \sin(p_\mu a)}{m^2 + \frac{1}{a^2}\sum_\mu \sin^2(p_\mu a)} \tag{2.18}$$

The poles of this matrix are associated with the physical particles. In the massless case $m = 0$, we have

$$\tilde{D}^{-1}(p) = -ia\frac{\sum_\mu \gamma_\mu \sin(p_\mu a)}{\sum_\mu \sin^2(p_\mu a)}, \tag{2.19}$$

which has not only a pole at $p_\mu = (0,0,0,0)$, corresponding to a physical particle in the continuum QCD theory, but also other 15 poles such as $p_\mu = (\pi/a, 0, 0, 0)$ and $p_\mu = (\pi/a, \pi/a, 0, 0)$. These 15 poles correspond to the particles that do not exist in the continuum QCD theory, which are called doublers. Therefore, lattice QCD theory with such action describes physics in the continuum limit that is different from QCD in continuous spacetime due to the presence of doublers.

Wilson fermion action

Wilson proposed a fermionic action without the doubler in the continuum limit, called the Wilson fermion action. The Fourier-transformed Dirac operator of the Wilson fermion action without the interaction is defined by

$$\tilde{D}(p) = m\mathbf{1} + \frac{i}{a}\sum_{\mu}\gamma_\mu\sin(p_\mu a) + \frac{1}{a}\sum_{\mu}(1 - \cos(p_\mu a))\mathbf{1}. \tag{2.20}$$

The last term is the new term called the Wilson term. Its inverse matrix is given by

$$\tilde{D}^{-1}(p) = \frac{(m + \frac{1}{a}\sum_\mu (1 - \cos(p_\mu a)))\mathbf{1} - \frac{i}{a}\sum_\mu \gamma_\mu \sin(p_\mu a)}{(m + \frac{1}{a}\sum_\mu (1 - \cos(p_\mu a)))^2 + \frac{1}{a^2}\sum_\mu \sin^2(p_\mu a)}, \tag{2.21}$$

which has 16 poles as well. However, each pole has a mass of

$$m + \frac{2l}{a}, \tag{2.22}$$

where l is the number of the components of π/a in the pole position for $m = 0$. Therefore, for the Wilson fermion action, there are one physical particle and doublers with the mass of $\mathcal{O}(1/a)$, and only the physical one survives in the continuum limit.

The Dirac operator of the Wilson fermion action in the real space with the interaction is expressed as

$$D(x|y)^{\alpha\beta}_{ab} = \left(m + \frac{4}{a}\right)\delta_{\alpha\beta}\delta_{ab}\delta_{x,y} - \frac{1}{2a}\sum_{\mu=\pm 1}^{\pm 4}(\mathbf{1} - \gamma_\mu)_{\alpha\beta}U_\mu(x)_{ab}\delta_{x+a\hat{\mu},y}, \tag{2.23}$$

where $\gamma_{-\mu} = -\gamma_\mu$. For the general number of flavors N_f, the Wilson fermion action is given by

$$S_F[\psi, \bar{\psi}, U] = a^4 \sum_f \sum_{x,y} \bar{\psi}^{(f)}_{a,\alpha}(x) D^{(f)}(x|y)^{\alpha\beta}_{ab} \psi^{(f)}_{b,\beta}(y), \tag{2.24}$$

where $D^{(f)}$ is the Wilson operator Eq. (2.23) with the mass parameter $m^{(f)}$.

The Wilson fermion satisfies the following:

$$D^\dagger = \gamma_5 D \gamma_5. \tag{2.25}$$

This property is called γ_5-hermiticity.

Chiral symmetry on lattice and Ginsparg-Wilson relation

The chiral transformation (U(1)×SU(N_f)) in continuous spacetime is given by

$$\begin{aligned} \psi &\to \psi' = e^{i\alpha_i T_i \gamma_5}\psi \\ \bar{\psi} &\to \bar{\psi}' = \bar{\psi} e^{i\alpha_i T_i \gamma_5}, \end{aligned} \tag{2.26}$$

where T_i is a generator of SU(N_f) or U(1). We consider this transformation on the lattice spacetime as well. Here, we consider the massless case.

For the action which has the chiral symmetry, the Dirac operator satisfies

$$D\gamma_5 + \gamma_5 D = 0. \tag{2.27}$$

This holds for the naive fermion action, while it does not for the Wilson fermion action because of the Wilson term, which is proportional to $\mathbf{1}$ in the spinor space. In other words, the Wilson fermion action does not have the chiral symmetry. Nielsen and Ninomiya showed that there are always doublers for the actions on the lattice that satisfy the following requirements simultaneously [24–26]:

- translation symmetry,
- chiral symmetry,
- hermiticity,
- locality.

This indicates no fermion action that removes doublers and satisfies chiral symmetry.

Ginsparg and Wilson introduced an "approximate chiral symmetry" [27] by proposing the equation for the Dirac operator as

$$D\gamma_5 + \gamma_5 D = aD\gamma_5 D \tag{2.28}$$

instead of Eq. (2.27). This is called the Ginsparg-Wilson relation and is obtained from the renormalization transformation in the continuum limit. Of course, the equation coincides with Eq. (2.27) in the continuum limit.

We define the transformation of the "approximate chiral symmetry" as

$$\begin{aligned} \psi' &= \exp\Big(i\alpha_i T_i \gamma_5 (\mathbf{1} - \frac{a}{2}D)\Big)\psi \\ \bar{\psi}' &= \bar{\psi}\exp\Big(i\alpha_i T_i (\mathbf{1} - \frac{a}{2}D)\gamma_5\Big). \end{aligned} \tag{2.29}$$

Fermion actions satisfying the Ginsperg-Wilson relation are invariant under this transformation. The projection operator for the "chirality" is described as

$$\hat{P}_R = \frac{1+\hat{\gamma}_5}{2}, \quad \hat{P}_L = \frac{1-\hat{\gamma}_5}{2}, \tag{2.30}$$

where $\hat{\gamma}_5 = \gamma_5(1-aD)$. Since $\hat{\gamma}_5^2 = \mathbf{1}$, $\hat{P}_R$ and $\hat{P}_L$ satisfy the properties of projection operators;

$$\hat{P}_R^2 = \hat{P}_R, \quad \hat{P}_L^2 = \hat{P}_L, \quad \hat{P}_L\hat{P}_R = \hat{P}_R\hat{P}_L = 0. \tag{2.31}$$

We define fermions of right-handed and left-handed "chirality" on a lattice as

$$\psi_R = \hat{P}_R\psi, \quad \psi_L = \hat{P}_L\psi \quad \bar{\psi}_R = \bar{\psi}\hat{P}_L, \quad \bar{\psi}_L = \bar{\psi}\hat{P}_R. \tag{2.32}$$

When the Ginsparg-Wilson relation is satisfied, the mixing of the "chirality" does not appear in the action, which is the same argument as for the chiral symmetry on continuous space-time.

The mass term for the Wilson fermion is given by

$$m(\bar{\psi}_L\psi_R + \bar{\psi}_R\psi_L) = m\bar{\psi}\Big(\mathbf{1} - \frac{a}{2}D\Big)\psi, \tag{2.33}$$

and then we get the Dirac operator with the mass term D_m as

$$D_m = D + m\Big(\mathbf{1} - \frac{a}{2}D\Big) = \omega D + m\mathbf{1} \quad \Big(\omega = 1 - \frac{a}{2}m\Big). \tag{2.34}$$

One of the Dirac operators satisfying the Ginsparg-Wilson relation is the overlap fermion [28].

2.2.3 Improvement of the action

In this section, we explain the method called the improvement [29, 30], which deforms the lattice action so that it becomes closer to the continuous one. We first explain the improvement of the difference as a simple example, and we then show the improvement of the lattice QCD action.

Improvement of differences

We improve the difference so that the discretization error cancels out. For a continuous function $f(x)$ and for a small number a (corresponding to the lattice spacing), we consider the following difference:

$$\frac{f(x+a)-f(x-a)}{2a} = f'(x) + a^2\frac{1}{6}f'''(x) + \mathcal{O}\big(a^4\big). \tag{2.35}$$

Then we can treat the above difference as the approximation of the first-order derivative $f'(x)$. As shown above, the discretization error is $\mathcal{O}(a^2)$.

Here we add other terms to cancel the third-order derivative term as

$$\frac{f(x+a)-f(x-a)}{2a} + a^2 D^{(3)}[f](x) = f'(x) + \mathcal{O}\big(a^4\big), \tag{2.36}$$

where $D^{(3)}[f](x)$ is linear combinations of $\{f(x+na)\}_{n\in\mathbb{Z}}$ that satisfies $D^{(3)}[f](x) = f'''(x) + \mathcal{O}(a^2)$. This equation no longer has the $\mathcal{O}(a^2)$ error.

In the above case,

$$D^{(3)}[f](x) = -\frac{1}{6}\frac{f(x+2a)-2f(x+a)-2f(x-a)-f(x-2a)}{2a^3}. \tag{2.37}$$

We note that this is not uniquely determined.

Improvement of the lattice QCD action

Here we consider the Wilson gauge action $S_G[U]$ and the Wilson fermion action $S_F[U,\psi,\bar{\psi}]$, which have errors of $\mathcal{O}(a^2)$ and $\mathcal{O}(a)$, respectively. In order to perform the improvement, we first consider the Lagrangian density of the lattice action embedded in the continuous spacetime and its expansion with respect to a as

$$\mathcal{L}(x) = \mathcal{L}^{(0)}(x) + a\mathcal{L}^{(1)}(x) + a^2\mathcal{L}^{(2)}(x) + \mathcal{O}\big(a^3\big). \tag{2.38}$$

Here, $\mathcal{L}^{(0)}(x)$ is the Lagrangian density of QCD theory in continuum, and $\mathcal{L}^{(n)}(x)$ corresponds to the discretization error of $\mathcal{O}(a^n)$. The mass dimension of $\mathcal{L}^{(n)}(x)$ is $n+4$. We can restrict the form of the error $\mathcal{L}^{(n)}(x)$ by considering the invariance under the symmetry of the lattice action.

For example, $\mathcal{L}^{(1)}(x)$ is the linear combination of the following five terms;

$$\begin{aligned}
\mathcal{L}_1^{(1)}(x) &= \bar{\psi}(x)\sigma_{\mu\nu}F_{\mu\nu}(x)\psi(x) \\
\mathcal{L}_2^{(1)}(x) &= \bar{\psi}(x)\overrightarrow{D}_\mu\overrightarrow{D}_\mu\psi(x) + \bar{\psi}(x)\overleftarrow{D}_\mu\overleftarrow{D}_\mu\psi(x) \\
\mathcal{L}_3^{(1)}(x) &= m\,\mathrm{tr}[F_{\mu\nu}(x)F_{\mu\nu}(x)] \\
\mathcal{L}_4^{(1)}(x) &= m(\bar{\psi}(x)\gamma_\mu\overrightarrow{D}_\mu\psi(x) - \bar{\psi}(x)\gamma_\mu\overleftarrow{D}_\mu\psi(x)) \\
\mathcal{L}_5^{(1)}(x) &= m^2\bar{\psi}(x)\psi(x),
\end{aligned} \tag{2.39}$$

where $\sigma_{\mu\nu} = [\gamma_\mu, \gamma_\nu]/2i$ and the arrow on the Dirac operator represents the direction in which the derivative acts (left or right). Since they are related to each other from the Dirac equation $(\gamma \cdot D + m)\psi(x) = 0$ as

$$\begin{aligned}
\mathcal{L}_1^{(1)} - \mathcal{L}_2^{(1)} + 2\mathcal{L}_5^{(1)} &= 0 \\
\mathcal{L}_4^{(1)} + 2\mathcal{L}_5^{(1)} &= 0,
\end{aligned} \tag{2.40}$$

three of the five terms $\mathcal{L}_1^{(1)}$, $\mathcal{L}_3^{(1)}$, and $\mathcal{L}_5^{(1)}$ are independent. Also, since $\mathcal{L}_3^{(1)}$ and $\mathcal{L}_5^{(1)}$ are proportional to $\mathcal{L}^{(0)}(x)$, we can absorb the two terms by redefining the bare parameters g and m, and then only $\mathcal{L}_1^{(1)}$ survives. Therefore, the lattice improved action up to $\mathcal{O}(a)$ is obtained as

$$S_{\text{imp}} = S_G + S_F + c_{\text{sw}}a^5\sum_x\sum_{\mu<\nu}\bar{\psi}(x)\frac{1}{2}\sigma_{\mu\nu}\hat{F}_{\mu\nu}(x)\psi(x), \tag{2.41}$$

where $\hat{F}_{\mu\nu}(x)$ is the quantity which is defined on the lattice and satisfies $\hat{F}_{\mu\nu}(x) = F_{\mu\nu}(x) + \mathcal{O}(a)$. This is not uniquely determined, but the following form is often used [31]:

$$\hat{F}_{\mu\nu}(x) = \frac{-i}{8a^2}(Q_{\mu\nu}(x) - Q_{\nu\mu}(x)), \tag{2.42}$$

where $Q_{\mu\nu}(x)$ is represented as

$$Q_{\mu\nu}(x) = U_{\mu\nu}(x) + U_{\nu-\mu}(x) + U_{-\mu\nu}(x) + U_{-\nu\mu}(x). \tag{2.43}$$

The new term in Eq. (2.41) is represented in Fig. 2.3 and is called the clover term.

The coefficient c_{sw}, called the Sheikholeslami-Wohlert coefficient, has been determined non-perturbatively using the PCAC relation on the lattice[1].

As seen above, the $\mathcal{O}(a)$ improvement changes only the Wilson fermion action since the Wilson gauge action has the error of $\mathcal{O}(a^2)$. We improve the Wilson gauge action up to $\mathcal{O}(a^2)$ by adding the rectangular plaquette variables. Refs. [32, 33] determines the coefficients of each term in the improved gauge action from the real-space block-spin renormalization group. The action with the coefficients is called the Iwasaki gauge action.

[1]The Wilson fermion action provides physical quantities with large discretization error coming from the breaking of the chiral symmetry, which makes it difficult to perform the extrapolation $a \to 0$ in practice. The improvement of the fermion action plays a role in reducing such errors (and the operator). From this point of view, the action satisfying the Ginsparg-Wilson relation has already been improved up to $\mathcal{O}(a)$.

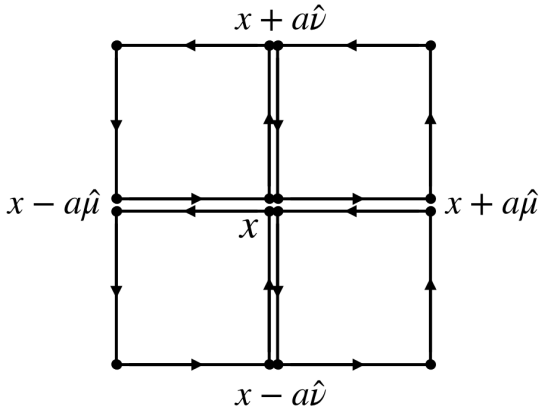

FIGURE 2.3: Diagrammatic picture of the clover term.

2.3 Path-integral formula of Correlation functions in lattice QCD

2.3.1 General correlation functions

The general correlation function is given by

$$\langle O_1(t_1)O_2(t_2)\cdots O_n(t_n)\rangle = \frac{1}{Z}\,\mathrm{tr}[e^{-(T-t_1)\hat{H}}\hat{O}_1 e^{-(t_1-t_2)\hat{H}}\hat{O}_2\cdots e^{-(t_{n-1}-t_n)\hat{H}}\hat{O}_n e^{-t_n\hat{H}}], \quad (2.44)$$

where Z is the partition function defined as

$$Z = \mathrm{tr}[e^{-T\hat{H}}]. \quad (2.45)$$

Here, $\hat{O}_i$ $(i = 1, \cdots, n)$ are (composite) operators acting on the Hilbert space. These operators play roles in the observables or the creations and annihilations of particles. The operator $\hat{H}$ denotes the Hamiltonian of QCD, and t_i are Euclidean times of the operator. The time T is the size of the extension in the time direction and corresponds to the inverse of the temperature.

We can describe Eq. (2.44) in the path integral formula as

$$\begin{aligned}\langle O_1(t_1)O_2(t_2)\cdots O_n(t_n)\rangle = \frac{1}{Z}\int \mathcal{D}[U]\mathcal{D}[\psi,\bar{\psi}]\; e^{-S_G[U]-S_F[\psi,\bar{\psi},U]} \\ \times O_1[\Phi(:,t_1)]O_2[\Phi(:,t_2)]\cdots O_n[\Phi(:,t_n)],\end{aligned} \quad (2.46)$$

with

$$Z = \int D[U]D[\psi,\bar{\psi}]\; e^{-S_G[U]-S_F[\psi,\bar{\psi},U]}. \quad (2.47)$$

Here, $\mathcal{D}[\Phi]$ with $\Phi = \{\psi, \bar{\psi}, U\}$ represents the measure for the integral over each field: the measure for the Grassmann integral for the fermion field and Haar measure for the gauge field. Also, $O_i[\Phi(:,t_i)]$ $(i = 1, \cdots, n)$ is the functional of the fields at time t_i corresponding to $\hat{O}_i$, where ":" denotes the arbitrary spatial dependence.

2.3.2 Calculation of the correlation functions

Integration over fermion fields

Since the fermion action is expressed in the bilinear form of the fermion fields, the path integral for the fermion is the Gaussian integral of the Grassmann variables.

Here we consider $N_f = 1$ for simplicity. The path-integral for the fermion fields whose integrand is a product of n ψs and $\bar{\psi}$s is represented as

$$\begin{aligned}
&\int D[\psi,\bar{\psi}]\, e^{-a^4\sum_{i,j}\bar{\psi}_i D_{ij}\psi_j}\ \psi_{i_1}\bar{\psi}_{j_1}\psi_{i_2}\bar{\psi}_{j_2}\cdots\psi_{i_n}\bar{\psi}_{j_n} \\
&= \frac{\partial}{\partial\theta_{j_1}}\frac{\partial}{\partial\bar{\theta}_{i_1}}\cdots\frac{\partial}{\partial\theta_{j_n}}\frac{\partial}{\partial\bar{\theta}_{i_n}}\int D[\psi,\bar{\psi}]\, e^{-a^4\sum_{i,j}\bar{\psi}_i D_{ij}\psi_j+\sum_i(\bar{\theta}_i\psi_i+\bar{\psi}_i\theta_i)} \\
&= \frac{\partial}{\partial\theta_{j_1}}\frac{\partial}{\partial\bar{\theta}_{i_1}}\cdots\frac{\partial}{\partial\theta_{j_n}}\frac{\partial}{\partial\bar{\theta}_{i_n}}\det\left[-a^4 D\right] e^{\sum_{i,j}\bar{\theta}_i (a^4 D)^{-1}_{ij}\theta_j} \\
&= \det\left[-a^4 D\right]\sum_{P_1,\cdots,P_n=1}^{n}\epsilon^{P_1\cdots P_n}(a^{-4}D^{-1}_{i_1 j_{P_1}})\cdots(a^{-4}D^{-1}_{i_n j_{P_n}}),
\end{aligned} \tag{2.48}$$

where $\epsilon^{P_1\cdots P_n}$ is an antisymmetric tensor which holds $\epsilon^{123\cdots n}=1$, the index $i=(x,c,\alpha)$ with spacetime x, color index c, and spinor index α, and "det" denotes the determinant in the space spanned by i. From this equation, we can get the rule to perform the path integral for the fermion fields, called the Wick contraction law, as follows.

- For the integrand $\psi_{i_1}\bar{\psi}_{j_1}\psi_{i_2}\bar{\psi}_{j_2}\cdots\psi_{i_n}\bar{\psi}_{j_n}$, we make pairs of ψ and $\bar{\psi}$. One example is as follows:

$$\overbrace{\psi_{i_1}\bar{\psi}_{j_1}}\overbrace{\psi_{i_2}\bar{\psi}_{j_2}}\cdots\overbrace{\psi_{i_n}\bar{\psi}_{j_n}}. \tag{2.49}$$

- Each neighboring pair gives the inverse of the Dirac operator with the indices which the pair has. That is,

$$\overbrace{\psi_i\bar{\psi}_j} = a^{-4}D^{-1}_{ij}. \tag{2.50}$$

  If the pair is not neighboring, we move either side to be next to the other side by swapping other fermion fields. Then a negative sign is generated for each swap due to the anticommutation relation of Grassmann numbers.

- The integration results in $\det[-a^4 D]$ multiplying by a summation over $n!$ combinations to make pairs as

$$\overbrace{\psi_{i_1}\bar{\psi}_{j_1}}\overbrace{\psi_{i_2}\bar{\psi}_{j_2}}\cdots\overbrace{\psi_{i_n}\bar{\psi}_{j_n}} + \overbrace{\psi_{i_1}\bar{\psi}_{j_1}\psi_{i_2}\bar{\psi}_{j_2}}\cdots\overbrace{\psi_{i_n}\bar{\psi}_{j_n}} + \cdots, \tag{2.51}$$

  which is equal to Eq. (2.48).

The inverse of the Dirac operator D^{-1} is called the fermion propagator.

Therefore, the path integral for the fermion in Eq. (2.44) can be performed as

$$\langle O_1(t_1)O_2(t_2)\cdots O_n(t_n)\rangle = \frac{\int D[U]\, e^{-S_G[U]}\det[D[U]]\, O[D^{-1}[U],U]}{\int D[U]\, e^{-S_G[U]}\det[D[U]]} \tag{2.52}$$

where $O[D^{-1}[U], U]$ is the result of the integration with the integrand

$$O_1[\psi(:,t_1), \bar{\psi}(:,t_1), U(:,t_1)] O_2[\psi(:,t_2), \bar{\psi}(:,t_2), U(:,t_2)] \cdots O_N[\psi(:,t_N), \bar{\psi}(:,t_N), U(:,t_N)],$$

which depends on the gauge field U explicitly or through the fermion propagator.

Similarly the correlation function for general N_f is represented as

$$\langle O_1(t_1) O_2(t_2) \cdots O_n(t_n) \rangle = \frac{\int D[U]\, e^{-S_G[U]} (\prod_f \det\left[D^{(f)}[U]\right])\, O[D^{-1}[U], U]}{\int D[U]\, e^{-S_G[U]} (\prod_f \det[D^{(f)}[U]])}, \tag{2.53}$$

where $D^{(f)}[U]$ is the Dirac operator of the flavor f. The Wick contraction law in the multi-flavor case is the same as for the single-flavor except for one additional rule that only the fermion fields with the same flavor take contractions.

Integration over gauge fields

We calculate the path-integral for the gauge field numerically. Since the dimension of the integral is quite huge, the Monte Carlo method is used in its calculation.

In this method, the operator-independent part in Eq. (2.53) described as

$$\frac{e^{-S_G[U]} (\prod_f \det[D_f[U]])}{\int D[U]\, e^{-S_G[U]} (\prod_f \det[D_f[U]])} \tag{2.54}$$

is regarded as a probability distribution. The integration is performed as follows. First, we generate samples of link variables $\{U_i\}$ that follow the probability, called the gauge configurations. We then calculate the operator $O[D^{-1}[U_i], U_i]$ for each configuration U_i. Finally, we obtain the correlation function by calculating the average of the operator $O[D^{-1}[U_i], U_i]$ as

$$\langle O_1(t_1) O_2(t_2) \cdots O_n(t_n) \rangle \approx \frac{1}{N} \sum_{i=1}^{N} O[D^{-1}[U_i], U_i]. \tag{2.55}$$

The Monte Carlo method can be applied only if Eq. (2.54) is real and non-negative for any link variable. The Boltzmann weight $e^{-S_G[U]}$ is positive by definition. For $\det[D_f[U]]$, we can prove that it is real by using the γ_5-hermiticity. However, it is not necessarily non-negative. When the number of quark flavors N_f is even and the quark masses degenerate, the determinant part $\det[D_f[U]]^2$ is non-negative and the above method can be applied. As an algorithm for generating the gauge configurations, the hybrid Monte Carlo (HMC) method [34, 35] is used.

For odd N_f, we cannot use the Monte Carlo method in general. However, in the case where $N_f = 3$, and the up and down quarks degenerate, we can use an alternative Monte Carlo method where the strange quark part of the fermion propagator $(D^s[U])^{-1}$ is expanded in terms of polynomials [36–38] or rational functions [39–42] of $D^s[U]$.

2.3.3 Error estimation and jack-knife method

For a physical quantity X, we represent X_i as the value calculated using the gauge configuration U_i ($i = 1, \cdots, N$), and $\langle X \rangle$ as its true expectation value. The unbiased estimator of $\langle X \rangle$ is the

mean value of X_i:

$$\hat{X} = \frac{1}{N}\sum_{i=1}^{N} X_i. \tag{2.56}$$

The variance of $\langle X \rangle$ is given by

$$\sigma_X^2 = \langle (X - \langle X \rangle)^2 \rangle = \langle X^2 \rangle - \langle X \rangle^2, \tag{2.57}$$

and its unbiased estimator is represented as

$$\hat{\sigma}_X^2 = \frac{1}{N-1}\Big[\Big(\frac{1}{N}\sum_{i=1}^{N} X_i^2\Big) - \hat{X}^2\Big]. \tag{2.58}$$

Thus the estimate of $\langle X \rangle$ and its error are given by

$$\hat{X} \pm \hat{\sigma}_{\hat{X}}. \tag{2.59}$$

For the function $f(\{X^{(a)}\})$ of multiple physical quantities $\{X^{(a)}\}$, the error $\hat{\sigma}_f$ is evaluated as

$$\hat{\sigma}_f = \sum_a \left| \Big(\frac{1}{N}\sum_{i=1}^{N} \frac{\partial f}{\partial X^{(a)}}\Big)\hat{\sigma}_{\hat{X}} \right|, \tag{2.60}$$

which is called the error-propagation formula. However, if the correlations among $\{X^{(a)}\}$ are large, the error evaluated in this equation becomes smaller than the true value, that is, the error is underestimated. This problem often occurs in lattice QCD calculations. For example, the mass is calculated by fitting the 2-point correlation function $C(t)$ at several t, which have large correlations to each other.

There are several ways to evaluate the error more properly for such quantities. One is to use the fitting that involves the correlation, where we minimize the following quantity for the fit function $f(t)$:

$$\sum_{t,t'=t_{min}}^{t_{max}} (C(t) - f(t))A(t,t')(C(t') - f(t')). \tag{2.61}$$

Here, $A(t,t')$ is the covariance matrix defined as

$$A(t,t') = \frac{1}{N-1}\sum_{i=1}^{N} \left[(C[U_i,t] - C(t))(C[U_i,t'] - C(t'))\right], \tag{2.62}$$

where $C[U_i,t]$ denotes the 2-point correlation function calculated for a gauge configuration U_i and $C(t) = \frac{1}{N}\sum_{i=1}^{N} C[U_i,t]$. However, it is difficult to use this estimation in practice because the covariance matrix often has so small eigenvalues that the fitting is unstable.

The other is the jackknife method, where we evaluate the error as follows. Let N be the total number of samples. First, for each physical quantity, we pick up $N-1$ samples out of N and

take an average of them. The average without $X_i^{(a)}$ is denoted by $\hat{X}_i^{(a)}$:

$$\hat{X}_i^{(a)} = \frac{1}{N-1}\sum_{k\neq i} X_k^{(a)}, \tag{2.63}$$

and they are called jackknife samples. We calculate the function $f(\{X^{(a)}\})$ for each jackknife sample (described as $f(\{\hat{X}_i^{(a)}\})$). Then the mean value and the error of $f(\{X^{(a)}\})$ are calculated as follows.

$$\begin{aligned}
\hat{f}(\{\hat{X}^{(a)}\}) &= \frac{1}{N}\sum_{i=1}^{N} f(\{\hat{X}_i^{(a)}\}) \\
\hat{\sigma}_f &= \sqrt{(N-1)\Big[\Big(\frac{1}{N}\sum_{i=1}^{N}(f(\{\hat{X}_i^{(a)}\}))^2\Big) - \Big(\frac{1}{N}\sum_{i=1}^{N} f(\{\hat{X}_i^{(a)}\})\Big)^2\Big]}
\end{aligned} \tag{2.64}$$

By removing multiple original samples for one jackknife sample, we can further reduce the contributions from the correlations. The correlations decrease and the value of the error increase as the number of removed samples increases. Then the error saturates to some value, which is regarded as the actual value of the error without correlations. We use the jackknife method to estimate the statistical error in our studies.

2.3.4 Two-point correlation functions and its Euclidean-time dependence

Here we consider Eq. (2.44) for $n = 2$ and set $t_1 = t$ and $t_2 = 0$ for simplicity. We also assume that the vacuum state $|0\rangle$ is unique in this subsection.

The partition function and the correlation function can be expressed in terms of the eigenstates $|n\rangle$ of the Hamiltonian as

$$\begin{aligned}
Z &= \sum_n \langle n|\, e^{-T\hat{H}}\, |n\rangle = \sum_n e^{-TE_n}, \\
\langle O_1(t)O_2(0)\rangle &= \frac{1}{Z}\sum_{m,n} \langle m|\, e^{-(T-t)\hat{H}}\, \hat{O}_1\, |n\rangle\, \langle n|\, e^{-t\hat{H}}\, \hat{O}_2\, |m\rangle \\
&= \frac{1}{Z}\sum_{m,n} e^{-(T-t)E_m}\, \langle m|\, \hat{O}_1\, |n\rangle\, e^{-tE_n}\, \langle n|\, \hat{O}_2\, |m\rangle\,,
\end{aligned} \tag{2.65}$$

where E_n are the energy eigenvalues of the state $|n\rangle$ with the order $E_0 \leq E_1 \leq E_2 \leq \cdots$. From now on, we set the vacuum energy $E_0 = 0$. Thus we obtain

$$\langle O_1(t)O_2(0)\rangle = \frac{\sum_{m,n} \langle m|\, \hat{O}_1\, |n\rangle\, \langle n|\, \hat{O}_2\, |m\rangle\, e^{-tE_n} e^{-(T-t)E_m}}{1 + \sum_{m>0} e^{-TE_m}}. \tag{2.66}$$

Here we assume $\langle 0|\, \hat{O}_1\, |0\rangle = \langle 0|\, \hat{O}_2\, |0\rangle = 0$. If T is sufficiently large, all the terms are suppressed by the exponential function except for the vacuum state $m = 0$, and then the correlation function reads

$$\langle O_1(t)O_2(0)\rangle \underset{T\to\infty}{\to} \sum_n \langle 0|\, \hat{O}_1\, |n\rangle\, \langle n|\, \hat{O}_2\, |0\rangle\, e^{-tE_n}. \tag{2.67}$$

Therefore, by choosing the proper operators, we can extract the energy of the states from the Euclidean-time dependence of the correlation function. From now on we call an operator $\hat{O}$ with nonzero value of $\langle n|\,\hat{O}\,|0\rangle$ (or $\langle 0|\,\hat{O}\,|n\rangle$) "an operator $\hat{O}$ having an overlap with the state $|n\rangle$". Equation (2.67) has only the contributions from the states which both operators $\hat{O}_1$ and $\hat{O}_2$ have an overlap with. When t is sufficiently large, the term for the lowest energy state is dominant, and then the energy of the ground state can be extracted from the t dependence.

From the observation above, hadron masses, for example, can be obtained as follows.

- We set $\hat{O}_1$ and $\hat{O}_2$ to the operators having an overlap with a single hadron in static. We represent such operators as $\hat{O}_H^\dagger$ and $\hat{O}_H$, respectively.
- Then the correlation function is expressed as

$$\langle O_H(t)O_H^\dagger(0)\rangle \underset{T\to\infty}{\to} |\langle H|\,\hat{O}_H^\dagger\,|0\rangle\,|^2 e^{-tm_H} + |\langle H'|\,\hat{O}_H^\dagger\,|0\rangle\,|^2 e^{-tE_{H'}} + \cdots. \tag{2.68}$$

  Here, $|H\rangle$ is the lightest single-hadron state in static which $\hat{O}_H^\dagger$ can create from the vacuum. On the other hand, $|H'\rangle$ is the 2nd lightest single-hadron state or the multiple-hadron state, and $\cdots$ denotes the contribution from the higher energy states.

- Taking a sufficiently large t, only the term for $|H\rangle$ survives. The hadron mass m_H can be obtained by the fitting using a function $f(t) = Ce^{-mt}$.

2.3.5 Variations of fermion and hadron operators

In this section, we express the fermion and hadron operators to have a strong overlap with the states of interest, which provides observables with high accuracy. After that, we explain the method to increase statistics using the symmetry of the theory.

Point, smeared, and wall source

In order to compute the correlation functions in lattice QCD, we compute the inverse matrix of the Dirac operator. Since the Dirac operator itself is a large matrix with indices of spacetime, spinor, and color, it has a high computational cost to calculate the inversion. Instead, we compute the propagator multiplied by a constant vector s;

$$\underset{ab}{D^{-1}(x,y)_{\alpha\beta}} s_{b,\beta}(y) \equiv g_{a,\alpha}(x). \tag{2.69}$$

This is equivalent to the linear equation $Dg = s$. Since the Dirac operator is a sparse matrix, it is possible to solve this equation using the algorithm with reasonable computational costs, for example, the conjugate gradient (CG) method. For fermion operators, this calculation corresponds to substituting $\bar{\psi}_{a,\alpha}(x)$ to $\sum_{x,a,\alpha} s_{a,\alpha}(x)\bar{\psi}_{a,\alpha}(x)$. The function $s(y)_{b,\beta}^{[x_0,\alpha_0,a_0]} = \delta_{y,x_0}\delta_{b,a_0}\delta_{\beta,\alpha_0}$ with fixed indices (x_0, a_0, α_0) is called point source, and Eq. (2.69) with this source is called the point-to-all propagators. In order to compute the propagators for fermion operator $\bar{\psi}_{a_0,\alpha_0}(x_0)$ with arbitrary a_0 and α_0, and fixed x_0, we only need to calculate the solution g for each of the 12 point sources with different color a_0 and spinor α_0 indices.

As a variation of the source operators, we consider the following source called the smeared source:

$$s(y)_{b,\beta}^{[x_0,\alpha_0,a_0]} = \delta_{t_y,t_{x_0}}\delta_{b,a_0}\delta_{\beta,\alpha_0}\sum_{\mathbf{z}} S(\mathbf{y}-\mathbf{z})\delta_{\mathbf{z},\mathbf{x}_0}, \tag{2.70}$$

where $S(\mathbf{y}-\mathbf{z})$ is an arbitrary function called the smearing function. One example of the smearing function which we often use is the following [43]:

$$S_{A,B}(\mathbf{x}) = \begin{cases} Ae^{-B|\mathbf{x}|} & (|\mathbf{x}|< \frac{L-1}{2}) \\ 1 & (|\mathbf{x}|= 0) \\ 0 & (|\mathbf{x}|\geq \frac{L-1}{2}), \end{cases} \tag{2.71}$$

where A and B are tunable parameters. The smeared source is associated with the following fermion operator

$$\sum_{\mathbf{z}} S_{A,B}(\mathbf{x}_0-\mathbf{z})\ \bar{\psi}_{a_0,\alpha_0}(\mathbf{z},t_{x_0}), \tag{2.72}$$

which represents a fermion operator with a broad spatial size of about $1/B$. Qualitatively, such fermion operators represent more realistic quarks rather than point operators. In practice, the 2-point correlation functions using the smeared source with tuned parameters A and B isolate the contribution from the ground state at an earlier timeslice than that for the point source.

Furthermore, the function

$$s(y)_{b,\beta}^{[t_{x_0},\alpha_0,a_0]} = \delta_{t_y,t_{x_0}}\delta_{b,a_0}\delta_{\beta,\alpha_0} \tag{2.73}$$

with Euclidean time t_y and t_{x_0} is called the wall source. As is the case for the point source, we only have to solve g for the 12 sources with arbitrary a_0 and α_0. The wall source corresponds to the fermion operator $\sum_{\mathbf{x}_0}\bar{\psi}_{a_0,\alpha_0}(x_0)$ with spatial coordinate $\mathbf{x}_0$. In other words, using such source can be regarded as using a fermion operator extended uniformly in the spatial volume. Since the hadron operators composed of $\sum_{\mathbf{x}_0}\bar{\psi}_{a_0,\alpha_0}(x_0)$ have rotation invariance, they seem to have a large overlap with the lowest hadron states. However, in practice, the 2-point correlation functions for the wall source do not pick up the contribution from the ground state earlier than those for the smeared source.

The hadron operator with smeared or wall source includes the term where the original local quark operators are separated from each other. For example, there is the following term in the pion operator with the wall source:

$$\sum_{\mathbf{x}\neq\mathbf{y}}\bar{\psi}(\mathbf{x},t)\gamma_5\psi(\mathbf{y},t) \subset \left(\sum_{\mathbf{x}}\bar{\psi}(\mathbf{x},t)\right)\gamma_5\left(\sum_{\mathbf{y}}\psi(\mathbf{y},t)\right). \tag{2.74}$$

Therefore, in order to keep the gauge invariance of the operators, we have to insert link variables into the separations. Instead, we perform the gauge fixing to avoid the problem of the breaking of the gauge invariance of the operators.

Momentum projection of hadron operators

Let $O_H(\mathbf{x}, t_x)$ be a hadron operator at spacetime $(\mathbf{x}, t_x)$. Then the Fourier transform of the operator described as

$$\tilde{O}_H(\mathbf{p}, t_x) = \frac{1}{L^3} \sum_{\mathbf{x}} O_H(\mathbf{x}, t_x) e^{-i\mathbf{p}\cdot\mathbf{x}}, \tag{2.75}$$

has an overlap with hadron states with the same momentum. Therefore, using the operator $\tilde{O}_H(\mathbf{p} = 0)$ for 2-point correlation functions, the corresponding hadron masses can be extracted at early timeslice. Thanks to the total momentum conservation, once the source or sink operator with specific momentum is used, the correlation function gives identical results regardless of the momentum projection of the other operators.

Symmetry of operators

When the theory has symmetry, the correlation function is invariant under the symmetry transformation as

$$\langle O_1(x_1) O_2(x_2) \cdots O_n(x_n) \rangle = \langle O'_1(x_1) O'_2(x_2) \cdots O'_n(x_n) \rangle. \tag{2.76}$$

However, this does not hold in general at the level of one gauge configuration:

$$O_1[U, x_1] O_2[U, x_2] \cdots O_n[U, x_n] \neq O'_1[U, x_1] O'_2[U, x_2] \cdots O'_n[U, x_n], \tag{2.77}$$

due to its fluctuation. Using this fact, we can increase statistics using the transformed operators added to the original one as

$$\begin{aligned} \langle O_1(x_1) O_2(x_2) \cdots O_n(x_n) \rangle \approx \frac{1}{N} \sum_{i=1}^{N} \frac{1}{2} (&O_1[U_i, x_1] O_2[U_i, x_2] \cdots O_n[U_i, x_n] \\ &+ O'_1[U_i, x_1] O'_2[U_i, x_2] \cdots O'_n[U_i, x_n]). \end{aligned} \tag{2.78}$$

One example of the symmetries in which we can easily apply the technique is the translation in the time direction. We can increase statistics of the 2-point correlation functions by using the average of the observables over timeslices as

$$\frac{1}{T} \sum_{t_0} \langle O_1(t + t_0) O_2(t_0) \rangle. \tag{2.79}$$

We note that the computational cost, whose main contribution is the one from the calculation of the inverse of the Dirac operator, enhances as well by the total number of timeslices.

Chapter 3

HAL QCD method

In this chapter, we explain the HAL QCD method, which is one of the methods to extract information on hadron scatterings. In order to obtain it in QCD, we consider the following quantity called the Nambu-Bethe-Salpeter (NBS) wave function:

$$\Psi^W(\mathbf{r}) = \langle 0| \hat{O}_1(\mathbf{r}, 0)\hat{O}_2(\mathbf{0}, 0) |H_1, H_2; W\rangle \,, \tag{3.1}$$

where $|H_1, H_2; W\rangle$ is the two-body hadron state with the total energy W. The detail of the definition will be explained later. In the limit of $|\mathbf{r}|\to\infty$, the NBS wave function asymptotically takes the following form:

$$\Psi^W(\mathbf{r}) \underset{|r|\to\infty}{\propto} \frac{\sin\left(kr - \frac{l}{2}\pi + \delta^l(k)\right)}{kr} e^{i\delta^l(k)} Y^l_m(\Omega), \tag{3.2}$$

where $\delta^l(k)$ is the scattering phase shift of hadron two-body scattering defined by the S-matrix. From this fact, the NBS wave function can be regarded as a wave function in the scattering theory in quantum mechanics. Aoki, Ishii, and Hatsuda proposed a method to obtain the scattering phase shifts by extracting the interaction potential from the NBS wave function and then solving the Schrödinger equation using the interaction potential [14–16], called the HAL QCD method.

In this chapter, we first derive the asymptotic behavior of the NBS wave function, and then we introduce the HAL QCD method. Finally, we describe how to obtain the potentials in the HAL QCD method from the actual lattice QCD calculations.

3.1 Asymptotic behavior of Nambu-Bethe-Salpeter wave function

In this section, we first define the scattering states and then introduce the off-shell T-matrix, which is a key quantity in the derivation. Then we prove that the S-matrix can be represented by one variable, called the scattering phase shift, using its unitarity. Finally, we define the Nambu-Bethe-Salpeter wave function and derive its asymptotic form by using the Lippmann-Schwinger equation. For the convention and derivation in this section, we follow Refs. [44, 45].

3.1.1 Scattering states

We define a free one-particle or multiparticle state $|\alpha_0\rangle$ as a state which satisfies the following conditions:

- $|\alpha_0\rangle$ is an eigenstate of the Hamiltonian without the interaction $\hat{H}_0$:

$$\hat{H}_0 |\alpha_0\rangle = E_\alpha |\alpha_0\rangle . \tag{3.3}$$

- They are normalized as

$$\langle\alpha_0|\alpha_0'\rangle = \delta(\alpha_0 - \alpha_0'). \tag{3.4}$$

  Here, $\delta(\alpha_0 - \alpha_0')$ denotes a product of the Kronecker deltas or delta functions for all quantum numbers that $|\alpha_0\rangle$ has.

- The Hilbert space is spanned by all the free states. That is, any state $|\psi\rangle$ can be expanded as

$$|\psi\rangle = \int d\alpha_0 |\alpha_0\rangle \langle\alpha_0|\psi\rangle . \tag{3.5}$$

We also consider the states $|\alpha_{\text{in}}\rangle$ and $|\alpha_{\text{out}}\rangle$ that satisfy the following conditions.

- They are normalized:

$$\begin{aligned} \langle\alpha_{\text{in}}|\alpha_{\text{in}}'\rangle &= \delta(\alpha_{\text{in}} - \alpha_{\text{in}}'), \\ \langle\alpha_{\text{out}}|\alpha_{\text{out}}'\rangle &= \delta(\alpha_{\text{out}} - \alpha_{\text{out}}'). \end{aligned} \tag{3.6}$$

- $|\alpha_{\text{in}}\rangle$ and $|\alpha_{\text{out}}\rangle$ are energy eigenstates of the full Hamiltonian with the same eigenvalues as those of $|\alpha_0\rangle$:

$$\begin{aligned} \hat{H} |\alpha_{\text{in}}\rangle &= E_\alpha |\alpha_{\text{in}}\rangle , \\ \hat{H} |\alpha_{\text{out}}\rangle &= E_\alpha |\alpha_{\text{out}}\rangle . \end{aligned} \tag{3.7}$$

- For any state $|\psi\rangle$, there exists a state $e^{-i\hat{H}t} |\psi_\pm\rangle$ such that in the limit $t \to \mp\infty$,

$$\begin{aligned} e^{-i\hat{H}t} |\psi_+\rangle &\underset{t\to-\infty}{\to} e^{-i\hat{H}_0 t} |\psi\rangle , \\ e^{-i\hat{H}t} |\psi_-\rangle &\underset{t\to\infty}{\to} e^{-i\hat{H}_0 t} |\psi\rangle , \end{aligned} \tag{3.8}$$

  and they can be expanded in terms of $|\alpha_{\text{in}}\rangle$ and $|\alpha_{\text{out}}\rangle$, respectively, as

$$\begin{aligned} |\psi_+\rangle &= \int d\alpha_{\text{in}}\ g(\alpha_{\text{in}}) |\alpha_{\text{in}}\rangle , \\ |\psi_-\rangle &= \int d\alpha_{\text{out}}\ g(\alpha_{\text{out}}) |\alpha_{\text{out}}\rangle , \end{aligned} \tag{3.9}$$

  where $g(\alpha_{\text{in}}) = g(\alpha_{\text{out}}) = \langle\alpha_0|\psi\rangle$ is the expansion coefficient of $|\psi\rangle$ in terms of $|\alpha_0\rangle$.

The states satisfying these conditions are called scattering states or asymptotic states. In particular, $|\alpha_{\text{in}}\rangle$ ($|\alpha_{\text{out}}\rangle$) is called in (out) states. From the above definitions, we obtain the relation

between in and out states and $|\alpha_0\rangle$ as

$$\begin{aligned}\int d\alpha_{\text{in}}\, g(\alpha_{\text{in}}) e^{-iE_\alpha t} |\alpha_{\text{in}}\rangle &\underset{t\to-\infty}{\to} \int d\alpha_0\, g(\alpha_0) e^{-iE_\alpha t} |\alpha_0\rangle\,, \\ \int d\alpha_{\text{out}}\, g(\alpha_{\text{out}}) e^{-iE_\alpha t} |\alpha_{\text{out}}\rangle &\underset{t\to\infty}{\to} \int d\alpha_0\, g(\alpha_0) e^{-iE_\alpha t} |\alpha_0\rangle\,,\end{aligned} \tag{3.10}$$

which indicates that the scattering state becomes the free state in the limit $t \to \pm\infty$ at the level of the wave packet, which represents the realistic particles.

3.1.2 Off-shell T-matrix and S-matrix

The off-shell T-matrix $T(\beta, \alpha)$ is defined by

$$T(\beta, \alpha) = \langle \beta_0 | \hat{V} | \alpha_{\text{in}} \rangle\,, \tag{3.11}$$

where $\hat{V}$ is the interaction term of the Hamiltonian. The S-matrix is given by

$$S(\beta \leftarrow \alpha) = \langle \beta_{\text{out}} | \alpha_{\text{in}} \rangle\,, \tag{3.12}$$

and the S-matrix operator $\hat{S}$ is defined by $S(\beta \leftarrow \alpha) = \langle \beta_0 | \hat{S} | \alpha_0 \rangle$. Furthermore, we introduce an operator $\hat{T}$ as $\hat{S} = 1 - i\hat{T}$ called the on-shell T-matrix operator.

The off-shell T-matrix and S-matrix have the following relation:

$$S(\beta \leftarrow \alpha) = \delta(\beta - \alpha) - 2\pi i \delta(E_\beta - E_\alpha) T(\beta, \alpha). \tag{3.13}$$

Therefore, we obtain

$$\langle \beta_0 | \hat{T} | \alpha_0 \rangle = 2\pi \delta(E_\beta - E_\alpha) T(\beta, \alpha). \tag{3.14}$$

As seen in this equation, the on-shell T-matrix has zero value at $E_\alpha \neq E_\beta$, while the off-shell T-matrix $T(\beta, \alpha)$ is not necessarily zero even at $E_\alpha \neq E_\beta$. For this reason, $T(\beta, \alpha)$ is called "off-shell".

3.1.3 Unitarity of S-matrices and phase shifts

For simplicity, we consider the elastic scattering of two particles with the same mass. We represent the free particle state as $|\alpha_0\rangle = |\mathbf{p_1}, \mathbf{p_2}, s, s_z\rangle$, where s and s_z are the total spin of the system and its z-component, respectively. The complete set is then described as

$$1 = \int d\beta_0 |\beta_0\rangle\langle\beta_0| = \sum_s \sum_{s_z} \int d^3q_1 d^3q_2 |\mathbf{q_1}, \mathbf{q_2}, s, s_z\rangle\langle \mathbf{q_1}, \mathbf{q_2}, s, s_z|\,. \tag{3.15}$$

Since the scattering process conserves the total momentum and the total energy of the system, the T-matrix becomes

$$\langle \mathbf{k}, s', s'_z | \hat{T} | \mathbf{p}, s, s_z \rangle = \delta(E_k^{\text{tot}} - E_p^{\text{tot}}) \delta^{(3)}(\mathbf{K} - \mathbf{P}) t(\mathbf{k}, s', s'_z \leftarrow \mathbf{p}, s, s_z), \tag{3.16}$$

where $E_K^{\rm tot}$ and $E_P^{\rm tot}$ are the total energy, and $\mathbf{K}$ and $\mathbf{P}$ are the total momentum, $\mathbf{p} = (\mathbf{p}_1 - \mathbf{p}_2)/2$ and $\mathbf{k} = (\mathbf{k}_1 - \mathbf{k}_2)/2$ are the relative momentum, and $s(')$ and $s_z(')$ is the spin and its z component, respectively. Using this equation, the following relation holds for $t(\mathbf{k}, s', s'_z \leftarrow \mathbf{p}, s, s_z)$ and the off-shell T-matrix:

$$T(\mathbf{k}, s', s'_z, \mathbf{p}, s, s_z) = \frac{1}{2\pi}\delta^{(3)}(\mathbf{K} - \mathbf{P})t(\mathbf{k}, s', s'_z \leftarrow \mathbf{p}, s, s_z). \tag{3.17}$$

Since the S-matrix operator is unitary, $\hat{S}\hat{S}^\dagger = \hat{S}^\dagger\hat{S} = 1$, the T-matrix satisfies

$$\hat{T}^\dagger - \hat{T} = i\hat{T}^\dagger\hat{T}. \tag{3.18}$$

Using Eq. (3.15) and Eq. (3.16), the above equation becomes

$$\begin{aligned} &t^*(\mathbf{p}, s, s_z \leftarrow \mathbf{k}, s', s'_z) - t(\mathbf{k}, s', s'_z \leftarrow \mathbf{p}, s, s_z) \\ &= i\sum_{s''}\sum_{s''_z}\int d^3q\, \delta(E_k^{\rm tot} - E_q^{\rm tot})t^*(\mathbf{q}, s'', s''_z \leftarrow \mathbf{k}, s', s'_z)t(\mathbf{q}, s'', s''_z \leftarrow \mathbf{p}, s, s_z). \end{aligned} \tag{3.19}$$

From the following, we consider the center-of-mass frame, where the energy conservation law gives $|\mathbf{k}| = |\mathbf{p}|$ with the momentum of in and out states $\mathbf{k}$ and $\mathbf{p}$, respectively. Then $t(\mathbf{k}, s', s'_z \leftarrow \mathbf{p}, s, s_z)$ can be described as

$$t(\mathbf{k}, s', s'_z \leftarrow \mathbf{p}, s, s_z) = \sum_{l',l}\sum_{j,j_z} t_j(p)_{l's',ls}\mathcal{Y}^{l's'}_{jj_z}(\Omega_{\hat{\mathbf{k}}})_{s'_z}\mathcal{Y}^{ls*}_{jj_z}(\Omega_{\hat{\mathbf{p}}})_{s_z}, \tag{3.20}$$

where l is the orbital angular momentum, j and j_z are the total angular momentum and its z component, respectively. The quantity $\mathcal{Y}^{ls}_{jj_z}(\Omega_{\hat{\mathbf{p}}})_{s_z}$ is given by

$$\mathcal{Y}^{ls}_{jj_z}(\Omega_{\hat{\mathbf{p}}})_{s_z} = \sum_{s_z} Y^l_{l_z}(\Omega_{\mathbf{p}})\,\langle l, l_z, s, s_z | l, s, j, j_z\rangle\,, \tag{3.21}$$

where $\langle l, l_z, s, s_z | l, s, j, j_z\rangle$ is the Clebsch-Gordan coefficients, which behaves as the ordinary spherical harmonics. For example, it follows the orthogonal relation

$$\sum_{s_z}\int d\Omega_{\mathbf{p}}\, \mathcal{Y}^{l's*}_{j'j'_z}(\Omega_{\hat{\mathbf{p}}})_{s_z}\mathcal{Y}^{ls}_{jj_z}(\Omega_{\hat{\mathbf{p}}})_{s_z} = \delta_{l'l}\delta_{j'j}\delta_{j'_zj_z} \tag{3.22}$$

for any spin s. Thus Eq. (3.19) reads

$$t^*_j(p,p)_{ls,l's'} - t_j(p,p)_{l's',ls} = \frac{ipE_p^{\rm tot}}{4}\sum_{l''.s''} t^*_j(p,p)_{l''s'',l's'}\, t_j(p,p)_{l''s'',ls}. \tag{3.23}$$

The meson-baryon system corresponds to a system with spin-$1/2$ and spin-0. In this case, $s = s' = s'' = s'' = 1/2$ and the orbital angular momentum is taken $l = j + 1/2$ or $l = j - 1/2$ for specific j. Since the parity in the two cases is opposite, the orbital angular momentum does not change during the scattering process as long as the theory has the parity symmetry. In other

words, $t_j(p)_{l'1/2,l1/2}$ is diagonal. Thus Eq. (3.23) becomes

$$t_l^{j*}(p) - t_l^j(p) = \frac{ipE_p^{\text{tot}}}{4} t_l^{j*}(p)\, t_l^j(p), \tag{3.24}$$

where we abbreviate $t_l^j(p) = t_j(p)_{l1/2,l1/2}$. This constraint indicates that $t_l^j(p)$ can be described in terms of one real variable $\delta_l^j(p)$ as

$$t_l^j(p) = -\frac{8}{pE_p^{\text{tot}}} e^{i\delta_l^j(p)} \sin\delta_l^j(p). \tag{3.25}$$

The variable $\delta_l^j(p)$ is called the scattering phase shift.

3.1.4 NBS wave function and its asymptotic behavior

For simplicity, here we consider a system of two scalar particles with the same mass. Let $\mathbf{p}_i$ $(i = 1, 2)$ be the momentum of i-th particle and $\alpha = (\mathbf{p}_1, \mathbf{p}_2)$ be a set of the quantum numbers of the two-body system. The NBS wave function is defined as

$$\Psi_\alpha(\mathbf{x}_1, \mathbf{x}_2) = \langle 0_{\text{in}} |\, \phi_1(\mathbf{x}_1, 0)\phi_2(\mathbf{x}_2, 0)\, |\alpha_{\text{in}}\rangle\,, \tag{3.26}$$

where $\phi_i(\mathbf{x}, t)$ $(i = 1, 2)$ are the Heisenberg operators corresponding to i-th particles, $|0_{\text{in}}\rangle$ is the vacuum state of the theory with the interaction (not the free theory).

Any scattering state satisfies the Lippmann-Schwinger equation:

$$|\alpha_{\text{in}}\rangle = |\alpha_0\rangle + \int d\beta_0 \frac{T(\beta, \alpha)}{E_\alpha - E_\beta + i\epsilon} |\beta_0\rangle\,. \tag{3.27}$$

Thus Eq. (3.26) reads

$$\begin{aligned}\Psi_\alpha(\mathbf{x}_1, \mathbf{x}_2) = {} & \frac{1}{Z_\alpha} \langle 0_{\text{in}} |\, \phi_1(\mathbf{x}_1, 0)\phi_2(\mathbf{x}_2, 0)\, |\alpha_0\rangle \\ & + \int d\beta_0 \frac{1}{Z_\beta} \frac{\langle 0_{\text{in}} |\, \phi_1(\mathbf{x}_1, 0)\phi_2(\mathbf{x}_2, 0)\, |\beta_0\rangle\, T(\beta, \alpha)}{E_\alpha - E_\beta + i\epsilon}.\end{aligned} \tag{3.28}$$

Also, the Lippmann-Schwinger equation for $|0_{\text{in}}\rangle$ is given by

$$|0_{\text{in}}\rangle = |0_0\rangle + \int d\gamma_0 \frac{T(\gamma, 0)}{E_0 - E_\gamma + i\epsilon} |\gamma_0\rangle\,, \tag{3.29}$$

where $|0_0\rangle$ is the vacuum state in the free theory. In the limit $|\mathbf{x}_1 - \mathbf{x}_2| \to \infty$, the following relation holds:

$$\langle 0_{\text{in}} |\, \phi_1(\mathbf{x}_1, 0)\phi_2(\mathbf{x}_2, 0)\, |\alpha_0\rangle \simeq \frac{1}{Z_\alpha} \langle 0_0 |\, \phi_1(\mathbf{x}_1, 0)\phi_2(\mathbf{x}_2, 0)\, |\alpha_0\rangle\,, \tag{3.30}$$

where the Z_α is a factor which depends on the states $|\alpha_{\text{in}}\rangle$ and $T(\gamma, 0)$. For the derivation, see Appendix.A in [45]. Using the above equation, Eq. (3.28) becomes

$$\begin{aligned}\Psi_\alpha(\mathbf{x}_1, \mathbf{x}_2) \simeq & \frac{1}{Z_\alpha} \langle 0_0| \phi_1(\mathbf{x}_1, 0)\phi_2(\mathbf{x}_2, 0) |\alpha_0\rangle \\ & + \int d\beta_0 \frac{1}{Z_\beta} \frac{\langle 0_0| \phi_1(\mathbf{x}_1, 0)\phi_2(\mathbf{x}_2, 0) |\beta_0\rangle T(\beta, \alpha)}{E_\alpha - E_\beta + i\epsilon}.\end{aligned} \tag{3.31}$$

Heisenberg fields at $t = 0$ and free particle states are expanded in terms of the creation and annihilation operators as

$$\begin{aligned}\phi_1(\mathbf{x}, 0) &= \int \frac{d^3k_1}{\sqrt{(2\pi)^3 E_{k_1}}} [a_1(\mathbf{k}_1)e^{i\mathbf{k}_1\cdot\mathbf{x}} + b_1^\dagger(\mathbf{k}_1)e^{-i\mathbf{k}_1\cdot\mathbf{x}}], \\ \phi_2(\mathbf{x}, 0) &= \int \frac{d^3k_2}{\sqrt{(2\pi)^3 E_{k_2}}} [a_2(\mathbf{k}_2)e^{i\mathbf{k}_2\cdot\mathbf{x}} + b_2^\dagger(\mathbf{k}_2)e^{-i\mathbf{k}_2\cdot\mathbf{x}}], \\ |\alpha_0\rangle &= |\mathbf{p}_1, \mathbf{p}_2\rangle = a_1^\dagger(\mathbf{p}_1)a_2^\dagger(\mathbf{p}_2) |0\rangle .\end{aligned} \tag{3.32}$$

Using the commutation relation $[a_i(\mathbf{p}), a_j^\dagger(\mathbf{k})] = \delta_{i,j}\delta^{(3)}(\mathbf{p} - \mathbf{k})$, we can rewrite the first term in Eq. (3.31) in terms of the plane waves:

$$\frac{1}{Z_\alpha} \langle 0| \phi_1(\mathbf{x}_1, 0)\phi_2(\mathbf{x}_2, 0) |\alpha_0\rangle = \frac{1}{Z_\alpha} \frac{1}{(2\pi)^3\sqrt{2E_{p_1}2E_{p_2}}} e^{i\mathbf{p}_1\cdot\mathbf{x}_1 + i\mathbf{p}_2\cdot\mathbf{x}_2}. \tag{3.33}$$

Furthermore, since the integrand of the second term survives only in the case where $|\beta_0\rangle$ is the two-particle state, the second term reads

$$\begin{aligned}& \int d\beta_0 \frac{1}{Z_\beta} \frac{\langle 0| \phi_1(\mathbf{x}_1, 0)\phi_2(\mathbf{x}_2, 0) |\beta_0\rangle T(\beta, \alpha)}{E_\alpha - E_\beta + i\epsilon} \\ = & \int \frac{d^3k_1 d^3k_2}{(2\pi)^3\sqrt{2E_{k_1}2E_{k_2}}} \frac{1}{Z_\beta} \frac{T(\beta, \alpha)e^{i\mathbf{k}_1\cdot\mathbf{x}_1 + i\mathbf{k}_2\cdot\mathbf{x}_2}}{E_{p_1} + E_{p_2} - E_{k_1} - E_{k_2} + i\epsilon}.\end{aligned} \tag{3.34}$$

Since the off-shell T-matrix can be expressed in terms of $t(\mathbf{k} \leftarrow \mathbf{p})$ as seen in Eq. (3.17), the above equation becomes

$$\begin{aligned}& \int \frac{d^3K d^3k}{(2\pi)^3\sqrt{2E_{k_1}2E_{k_2}}} \frac{1}{Z_\beta} \frac{1}{2\pi} \delta^{(3)}(\mathbf{K} - \mathbf{P}) \frac{t(\mathbf{k} \leftarrow \mathbf{p})e^{i\mathbf{k}\cdot\mathbf{r} + i\mathbf{K}\cdot\mathbf{X}}}{E_{p_1} + E_{p_2} - E_{k_1} - E_{k_2} + i\epsilon} \\ = & e^{i\mathbf{P}\cdot\mathbf{X}} \int \frac{d^3k}{(2\pi)^3\sqrt{2E_{k_1}2E_{k_2}}} \frac{1}{Z_\beta} \frac{1}{2\pi} \frac{t(\mathbf{k} \leftarrow \mathbf{p})e^{i\mathbf{k}\cdot\mathbf{r}}}{E_{p_1} + E_{p_2} - E_{k_1} - E_{k_2} + i\epsilon},\end{aligned} \tag{3.35}$$

where $\mathbf{X}$ ($\mathbf{P}$) and $\mathbf{x}$ ($\mathbf{p}$) is the total and relative coordinates (momentum), respectively.

In the center-of-mass frame $\mathbf{P} = 0$, the NBS wave function in the limit $|\mathbf{r}| \to \infty$ becomes

$$\Psi_\alpha(\mathbf{r}; \mathbf{p}) \simeq \frac{1}{Z_\alpha} \frac{e^{i\mathbf{p}\cdot\mathbf{r}}}{(2\pi)^3 2E_p} + \frac{1}{4\pi} \int \frac{d^3k}{(2\pi)^3 2E_k} \frac{1}{Z_\beta} \frac{t(\mathbf{k} \leftarrow \mathbf{p})e^{i\mathbf{k}\cdot\mathbf{r}}}{E_p - E_k + i\epsilon}. \tag{3.36}$$

Expanding the plane waves in terms of the spherical harmonics represented as

$$e^{i\mathbf{p}\cdot\mathbf{r}} = 4\pi \sum_{l,m} i^l j_l(pr) Y_m^l(\Omega_\mathbf{r}) Y_m^{l*}(\Omega_\mathbf{p}), \tag{3.37}$$

where $j_l(z)$ is the spherical Bessel function, we obtain

$$\Psi_\alpha^l(r;p) \simeq \frac{1}{(2\pi)^3 2E_p Z_\alpha}\Big[j_l(pr) + \frac{1}{4\pi}\int_0^\infty k^2 dk\, \frac{Z_\alpha E_p}{Z_\beta E_k}\frac{t^l(k,p) j_l(kr)}{E_p - E_k + i\epsilon}\Big]. \tag{3.38}$$

In the energy region of the elastic scattering, $t^l(k,p)$ has no poles or branches on the real axis. Thus in this region, the integral in Eq. (3.38) can be performed as

$$\begin{aligned}
\frac{1}{4\pi}\int_0^\infty k^2 dk\, \frac{Z_\alpha E_p}{Z_\beta E_k}\frac{t^l(k,p) j_l(kr)}{E_p - E_k + i\epsilon} &= -\frac{1}{4\pi}\int_0^\infty k^2 dk\, \frac{Z_\alpha E_p}{Z_\beta E_k}(E_p + E_k) t^l(k,p)\frac{j_l(kr)}{k^2 - p^2 - i\epsilon} \\
&= -\frac{i}{4\pi}\frac{\pi p}{2}\frac{Z_\alpha E_p}{Z_\alpha E_p}(E_p + E_p) t^l(p,p) h^{(1)}(pr) \\
&= -\frac{ipE_p}{4} t^l(p,p) h_l^{(1)}(pr),
\end{aligned} \tag{3.39}$$

where $h_l^{(1)}(z)$ is the spherical Hankel function of the first kind:

$$\begin{aligned}
h_l^{(1)}(z) &= j_l(z) + i n_l(z), \\
h_l^{(2)}(z) &= j_l(z) - i n_l(z),
\end{aligned} \tag{3.40}$$

with the spherical Neumann function $n_l(z)$. Using Eq. (3.39) and Eq. (3.25), Eq. (3.38) becomes

$$\begin{aligned}
\Psi_\alpha^l(r;p) &\underset{r\to\infty}{\simeq} \frac{1}{(2\pi)^3 Z_\alpha 2E_p}\Big[j_l(pr) + i e^{i\delta^l(p)} \sin\delta^l(p) h_l^{(1)}(pr)\Big] \\
&= \frac{1}{(2\pi)^3 Z_\alpha 2E_p} e^{i\delta^l(p)}\Big[\cos\delta^l(p) j_l(pr) + \sin\delta^l(p) n_l(pr)\Big].
\end{aligned} \tag{3.41}$$

Since the solutions of the radial part of the Schrödinger equation in the free particles are the spherical Bessel function and Neumann function, the equation above implies that the NBS wave function satisfies the Helmholtz equation in the limit $r \to \infty$. Furthermore, using the asymptotic behavior of the spherical Bessel function and the spherical Neumann function:

$$\begin{aligned}
j_l(z) &\underset{z\to\infty}{\to} \frac{\cos\big(z - \frac{l+1}{2}\pi\big)}{z} = \frac{\sin\big(z - \frac{l}{2}\pi\big)}{z} \\
n_l(z) &\underset{z\to\infty}{\to} \frac{\sin\big(z - \frac{l+1}{2}\pi\big)}{z} = -\frac{\cos\big(z - \frac{l}{2}\pi\big)}{z},
\end{aligned} \tag{3.42}$$

we consequently obtain

$$\Psi_\alpha^l(r;p) \underset{r\to\infty}{\simeq} \frac{1}{(2\pi)^3 Z_\alpha 2E_p}\frac{\sin\big(pr - \frac{l}{2}\pi + \delta^l(p)\big)}{pr} e^{i\delta^l(p)}, \tag{3.43}$$

which is the asymptotic behavior of the wave function in the scattering theory in quantum mechanics. The phase shift in this equation is the same as the one defined by the S-matrix of the

hadron scattering of interest.

3.2 HAL QCD method

We saw that we could obtain the scattering phase shift from the asymptotic behavior of the NBS wave functions. However, it is difficult to calculate the function directly in lattice QCD. There are two main methods to extract the phase shift indirectly in lattice QCD. One is the finite volume method, in which we use the boundary conditions in the finite volume. The other is the HAL QCD method, which we will explain in this subsection.

In this section, we first explain the HAL QCD method and show one example to derive the next-leading order term of the potential in the derivative expansion. Then we present the naive application of the HAL QCD method in lattice QCD using the n-point correlation functions and its difficulties for systems including baryons. Finally, we express the alternative one, called the time-dependent HAL QCD method, which uses not only the ground state but also the excited elastic states and enables us to simulate in systems including baryons.

3.2.1 Interaction potentials in the HAL QCD method

The NBS wave function at Euclidean time t is written as

$$\Psi^W(\mathbf{r},t) = \Psi^W(\mathbf{r})\, e^{-Wt} = \langle 0|\, \hat{O}_1(\mathbf{x}+\mathbf{r},t)\hat{O}_2(\mathbf{x},t)\,|H_1,H_2,W\rangle\,, \tag{3.44}$$

where $\hat{O}_i(\mathbf{x},t)$ $(i=1,2)$ are the Heisenberg operators of the hadrons at $(\mathbf{x},t)$, and $|H_1,H_2,W\rangle$ is a two-body hadron state with energy $W = \sqrt{k^2+m_1^2}+\sqrt{k^2+m_2^2}$. As seen in Sec. 3.1, in the energy region $W < W_{\text{th}}$ where only elastic scattering occurs, the NBS wave function satisfies the Helmholtz equation at $|\mathbf{r}|\to\infty$.

$$(k^2+\nabla^2)\Psi^W(\mathbf{r}) \simeq 0. \tag{3.45}$$

This equation can be regarded as the Schrödinger equation for a free particle;

$$H_0\Psi^W(\mathbf{r}) \equiv -\frac{\nabla^2}{2\mu}\Psi^W(\mathbf{r}) \simeq \frac{k^2}{2\mu}\Psi^W(\mathbf{r}), \tag{3.46}$$

where μ is the reduced mass.

In the HAL QCD method, we define the potential $U(\mathbf{r},\mathbf{r}')$ as

$$\int d^3r'\, U(\mathbf{r},\mathbf{r}')\Psi^W(\mathbf{r}') = \Big(\frac{k^2}{2\mu} - H_0\Big)\Psi^W(\mathbf{r}). \tag{3.47}$$

The potential is non-local but independent of energy. Also, it becomes zero at $|\mathbf{r}|\to\infty$ by definition. We note that the potential is defined only in the elastic region $W < W_{\text{th}}$, and the definition is not unique, which implies that it is not observable and determined in a certain scheme. For example, different hadron operators $O_i(\mathbf{x},t)$ give different forms of the potentials, but provide the same observable such as the scattering phase shifts in principle.

In practice, we perform the derivative expansion of the non-local potential as

$$U(\mathbf{r},\mathbf{r}') = \sum_{n=0}^{\infty} V^{(n)}(\mathbf{r})(\nabla^2)^n \delta^{(3)}(\mathbf{r}-\mathbf{r}'). \tag{3.48}$$

The leading-order (LO) term is derived from the NBS wave function $\Psi^{W_0}(\mathbf{r})$ for a certain energy as

$$V^{(0)}(r) = \frac{\left(\frac{k_0^2}{2\mu} - H_0\right)\Psi^W(\mathbf{r})}{\Psi^W(\mathbf{r})}. \tag{3.49}$$

In order to derive the higher-order terms, we need the NBS wave functions with different energies. For example, we obtain the LO and next-leading-order (NLO) term from the two NBS wave functions $\Psi^{W_0}(\mathbf{r})$ and $\Psi^{W_1}(\mathbf{r})$ with different energy W_0 and W_1. They satisfy the Schrödinger equation as

$$\begin{aligned}(V^{(0)}(r) + V^{(1)}(r)\nabla^2)\Psi^{W_0}(\mathbf{r}) &= \left(\frac{k_0^2}{2\mu} - H_0\right)\Psi^{W_0}(\mathbf{r}),\\ (V^{(0)}(r) + V^{(1)}(r)\nabla^2)\Psi^{W_1}(\mathbf{r}) &= \left(\frac{k_1^2}{2\mu} - H_0\right)\Psi^{W_1}(\mathbf{r}).\end{aligned} \tag{3.50}$$

The above two equations can then be expressed using matrices:

$$\begin{pmatrix}\Psi^{W_0}(\mathbf{r}) & \nabla^2\Psi^{W_0}(\mathbf{r})\\ \Psi^{W_1}(\mathbf{r}) & \nabla^2\Psi^{W_1}(\mathbf{r})\end{pmatrix}\begin{pmatrix}V^{(0)}(r)\\ V^{(1)}(r)\end{pmatrix} = \begin{pmatrix}\left(\frac{k_0^2}{2\mu} - H_0\right)\Psi^{W_0}(\mathbf{r})\\ \left(\frac{k_1^2}{2\mu} - H_0\right)\Psi^{W_1}(\mathbf{r})\end{pmatrix} \tag{3.51}$$

Thus, the leading-order term $V^{(0)}(r)$ and the next-leading-order term $V^{(1)}(r)$ reads

$$\begin{aligned}\begin{pmatrix}V^{(0)}(r)\\ V^{(1)}(r)\end{pmatrix} &= \begin{pmatrix}\Psi^{W_0}(\mathbf{r}) & \nabla^2\Psi^{W_0}(\mathbf{r})\\ \Psi^{W_1}(\mathbf{r}) & \nabla^2\Psi^{W_1}(\mathbf{r})\end{pmatrix}^{-1}\begin{pmatrix}\left(\frac{k_0^2}{2\mu} - H_0\right)\Psi^{W_0}(\mathbf{r})\\ \left(\frac{k_1^2}{2\mu} - H_0\right)\Psi^{W_1}(\mathbf{r})\end{pmatrix}\\ &= [\Psi^{W_0}(\mathbf{r})(\nabla^2\Psi^{W_1}(\mathbf{r})) - \Psi^{W_1}(\mathbf{r})(\nabla^2\Psi^{W_0}(\mathbf{r}))]^{-1}\\ &\times\begin{pmatrix}(\nabla^2\Psi^{W_1}(\mathbf{r}))\left(\frac{k_0^2}{2\mu} - H_0\right)\Psi^{W_0}(\mathbf{r}) - (\nabla^2\Psi^{W_0}(\mathbf{r}))\left(\frac{k_1^2}{2\mu} - H_0\right)\Psi^{W_1}(\mathbf{r})\\ -\Psi^{W_1}(\mathbf{r})\left(\frac{k_0^2}{2\mu} - H_0\right)\Psi^{W_0}(\mathbf{r}) + \Psi^{W_0}(\mathbf{r})\left(\frac{k_1^2}{2\mu} - H_0\right)\Psi^{W_1}(\mathbf{r}).\end{pmatrix}\end{aligned} \tag{3.52}$$

3.2.2 HAL QCD method in lattice QCD

In order to apply the HAL QCD method to the lattice calculation, we consider the following quantity:

$$F(\mathbf{r},t) = \langle O_1(\mathbf{x}+\mathbf{r}, t+t_0)O_2(\mathbf{x}, t+t_0)\,\bar{\mathcal{J}}(t_0)\rangle, \tag{3.53}$$

where $\bar{\mathcal{J}}(t_0)$ is the operator creating the two-body hadron state, called the source operator, while $O_1(\mathbf{x}+\mathbf{r}, t+t_0)O_2(\mathbf{x}, t+t_0)$ is called the sink operator. We call Eq. (3.53) the n-point correlation function, where n ($n \geq 3$) represents the total number of the single hadron operators at the source and sink together. Inserting the complete set, the n-point correlation function has the

following form at $T \to \infty$:

$$\begin{aligned} F(\mathbf{r},t) &\underset{T\to\infty}{\to} \sum_n \langle 0|\, \hat{O}_1(\mathbf{x}+\mathbf{r},t+t_0)\hat{O}_2(\mathbf{x},t+t_0)\,|H_1,H_2,W_n\rangle \,\langle H_1,H_2,W_n|\, \hat{\bar{\mathcal{J}}}(t_0)\,|0\rangle + \cdots \\ &= \sum_n \langle H_1,H_2,W_n|\, \hat{\bar{\mathcal{J}}}(0)\,|0\rangle\, \Psi^{W_n}(\mathbf{r})\, e^{-W_n t} + \cdots, \end{aligned} \tag{3.54}$$

where the term shown by $\cdots$ is the contributions from the inelastic states such as multi-particle states. Taking t sufficiently large, this reads

$$F(\mathbf{r},t) \underset{t\to\infty}{\simeq} \langle H_1,H_2,W_0|\, \hat{\bar{\mathcal{J}}}(0)\,|0\rangle\, \Psi^{W_0}(\mathbf{r})\, e^{-W_0 t}, \tag{3.55}$$

where W_0 is the energy of the ground state. This equation gives the NBS wave function for the ground state.

However, this technique is not useful for systems that include baryons. Here we note that in the lattice calculation, we always consider a finite-volume system; as seen from Sec. 3.1, we can get the potential correctly only if it is contained within the finite volume of the system, in other words, the potential converges to zero at the boundary. In order to get the correct results, we have to use a sufficiently large volume. In this case, however, we must be careful about another systematic uncertainty. In a finite volume with a spatial extension L, the difference of the energy between the ground state and the first excited state behaves as $\mathcal{O}(1/L^2)$. Therefore, in a large spatial volume, we have to take quite large t to extract the ground-state term as in Eq.(3.55). It is difficult, however, to do so for systems including baryons, where the signal-to-noise ratio for the gauge configurations decreases exponentially when t increases. Therefore, the technique explained above is not efficient for such systems.

3.2.3 Time-dependent HAL QCD method

We introduce the time-dependent HAL QCD method, which is a method to avoid the problem discussed above.

First, we define the following quantity called R-correlator:

$$R(\mathbf{r},t) = \frac{F(\mathbf{r},t)}{C_{H_1}(t)C_{H_2}(t)}, \tag{3.56}$$

where $C_{H_1}(t)$ and $C_{H_2}(t)$ are two-point correlation functions for hadrons H_1 and H_2, respectively. Here we decompose the R-correlator into contributions from elastic and inelastic states as

$$R(\mathbf{r},t) = \sum_n A_n \Psi^{W_n}(\mathbf{r})\, e^{-\Delta W_n t} + (\text{inelastic contributions}), \tag{3.57}$$

where W_n is the energy of the n-th eigen states, A_n is a coefficient independent of $\mathbf{r}$ and t, and $\Delta W_n = W_n - m_1 - m_2$ is an energy difference from the threshold. From Eq. (3.47), each term in the elastic part, $A_n \Psi^{W_n}(\mathbf{r}) e^{-\Delta W_n t}$, satisfies

$$\int d^3r'\, U(\mathbf{r},\mathbf{r}') A_n \Psi^{W_n}(\mathbf{r}') e^{-\Delta W_n t} = \left(\frac{k_n^2}{2\mu} - H_0\right) A_n \Psi^{W_n}(\mathbf{r}) e^{-\Delta W_n t}. \tag{3.58}$$

We express $k_n^2/2\mu$ in terms of ΔW_n as

$$\frac{k_n^2}{2\mu} = \frac{\mathcal{P}(\Delta W_n)}{(\Delta W_n/M+1)^2}, \tag{3.59}$$

with $M = m_1 + m_2$ and

$$\mathcal{P}(\Delta W_n) = \Delta W_n + \frac{\mu+M}{2\mu M}(\Delta W_n)^2 + \frac{1}{2\mu M}(\Delta W_n)^3 + \frac{1}{8\mu M^2}(\Delta W_n)^4. \tag{3.60}$$

In our studies, we expand k_n^2 in terms of ΔW_n as

$$\begin{aligned}\frac{k_n^2}{2\mu} &= \Delta W_n + \frac{1+3\delta^2}{8\mu}(\Delta W_n)^2 + \frac{M^2\delta^2}{8\mu}\sum_{k=3}^{\infty}(k+1)\left(\frac{-\Delta W_n}{M}\right)^k \\ &\equiv \sum_{k=1}^{\infty} C^{(k)}_{m_1,m_2}(\Delta W_n)^k,\end{aligned} \tag{3.61}$$

where $\delta = (m_1 - m_2)/M$. In Eq. (3.58), ΔW_n can be rewritten in terms of time derivatives. Summing over n, therefore, we obtain

$$\int d^3r'\, U(\mathbf{r},\mathbf{r}')R(\mathbf{r}',t) \simeq \left[\sum_{k=1}^{\infty} C^{(k)}_{m_1,m_2}\left(-\frac{\partial}{\partial t}\right)^k - H_0\right] R(\mathbf{r},t). \tag{3.62}$$

for a large enough t to suppress the inelastic contributions. Since the above equation is valid as long as the contribution of inelastic scattering is suppressed, the problem occurring for systems including baryons does not appear.

For meson-baryon systems, we substitute $R(\mathbf{r},t)$ and $U(\mathbf{r},\mathbf{r}')$ in Eq. (3.62) with the ones having the index for upper spin components of the baryon as $R_\alpha(\mathbf{r},t)$ and $U_{\alpha\beta}(\mathbf{r},\mathbf{r}')$. Applying the Okubo-Marshak expansion [46] to meson-baryon systems, the LO term of the potential in the derivative expansion is given by

$$U_{\alpha\beta}(\mathbf{r},\mathbf{r}') \simeq V^{\rm LO}(r)\delta_{\alpha\beta}\delta^{(3)}(\mathbf{r}-\mathbf{r}'), \tag{3.63}$$

where $V^{\rm LO}(r)$ can be extracted from $R_\alpha(\mathbf{r},t)$ for any α as

$$V^{\rm LO}(r) \simeq \frac{1}{R_\alpha(\mathbf{r},t)}\left[\sum_{k=1}^{\infty} C^{(k)}_{m_M,m_B}\left(-\frac{\partial}{\partial t}\right)^k - H_0\right] R_\alpha(\mathbf{r},t). \tag{3.64}$$

Therefore, calculating the R-correlator from the n-point correlation function and the two-point correlation function for each hadron, we can obtain the LO potential from Eq. (3.64).

In practice, we truncate an infinite summation over k in Eq. (3.64)[1]. In this case, we have to be careful about whether the remaining higher-order contributions are negligibly small.

[1]There is an alternative method to derive potentials without the expansion in ΔW by using at most the 3rd time derivatives, which is explained in Appendix A. For the P-wave $N\pi$ and $\Xi\bar{K}$ systems, we have confirmed that this exact one gives no significant differences from our potential results, showing that the higher-order contributions are indeed small.

Chapter 4

Calcualtion of all-to-all propagators and efficient method to increase statistics

Since the propagators for the point or wall source are computationally inexpensive, a wide variety of correlation functions can be computed using such propagators. However, there are systems where the correlation functions require propagators from arbitrary space-time points x_0, called the all-to-all propagators. Calculating the all-to-all propagator is equivalent to computing the inverse matrix of the Dirac operator itself, which has quite expensive computational costs. Although whether we need the all-to-all propagators depends on the details of the correlation functions we calculate, there are two typical cases where they are necessary. One is that we want to pick up hadron states with specific momentum. The other is that we want to see hadron resonances from the corresponding multi-hadron scatterings, where there are the contractions of quarks in the same hadron operator or quarks in different hadron operators at the same timeslice. Such contractions are called quark pair creation and annihilation.

Since it is difficult to calculate the exact all-to-all propagator by the current typical supercomputers, we approximate it. This chapter is organized as follows. First, we describe the stochastic technique to use noise vectors and the dilution. Then we describe the efficient method using noise vectors that can be applied to meson operators, called the one-end trick [47, 48]. Finally, we present the covariant-approximation averaging (CAA) combined with the truncated solver method, which is used together with the all-to-all calculations to increase statistics for reasonable computational cost.

4.1 Stochastic technique and dilution

4.1.1 Stochastic technique

We define the noise vector $\eta_{a,\alpha}(x)$ with the same degrees of freedom as that of the fermion field, such that the following properties are satisfied

$$\begin{aligned} &\langle\langle \eta_{a,\alpha}(x)\eta^*_{b,\beta}(y)\rangle\rangle = \delta_{x,y}\delta_{a,b}\delta_{\alpha,\beta}, \\ &\eta_{a,\alpha}(x)\eta^*_{a,\alpha}(x) = 1 \text{ (for all } x, a, \alpha). \end{aligned} \tag{4.1}$$

Note that the indices in the lower equation are not summed over. Then the fermion propagator $D^{-1}(x|y)^{\alpha\beta}_{ab}$ can be described as

$$\begin{aligned} D^{-1}(x|y)^{\alpha\beta}_{ab} &= \sum_{c,\gamma,z} D^{-1}(x|z)^{\alpha\gamma}_{ac}\delta_{z,y}\delta_{c,b}\delta_{\gamma,\beta} \\ &= \sum_{c,\gamma,z} D^{-1}(x|z)^{\alpha\gamma}_{ac}\langle\langle\eta_{c,\gamma}(z)\eta^*_{b,\beta}(y)\rangle\rangle \\ &= \langle\langle(\underbrace{D^{-1}\eta}_{\equiv\psi})_{a,\alpha}(x)\eta^*_{b,\beta}(y)\rangle\rangle \\ &= \langle\langle(\psi_{a,\alpha}(x)\eta^*_{b,\beta}(y)\rangle\rangle. \end{aligned} \tag{4.2}$$

Here, $\psi_{a,\alpha}(x)$ is the solution of the following linear equation

$$D(x|y)^{\alpha\beta}_{ab}\psi_{b,\beta}(y) = \eta_{a,\alpha}(x). \tag{4.3}$$

Thus, by sampling the noise vectors in accordance with the distribution Eq. (4.1) and calculating Eq. (4.3) for each sample, we obtain D^{-1} as

$$D^{-1}(x|y)^{\alpha\beta}_{ab} = \lim_{N_r\to\infty}\frac{1}{N_r}\sum_{r=1}^{N_r}\psi^{[r]}_{a,\alpha}(x)\eta^{[r]*}_{b,\beta}(y), \tag{4.4}$$

where $[r]$ denotes the label of the samples. In practice, we truncate the number of the samples and then get the approximated all-to-all propagator D^{-1}. Since this method only requires solving N_r linear equations, it has a much low computational cost.

4.1.2 Dilution technique

The dilution technique [49] is a method to suppress errors from the noise vectors. As an example here, we show the dilution for the discrete time coordinate t, but the same can be applied to other indices.

We decompose the noise vector as follows

$$\eta_{a,\alpha}(x) = \sum_j \eta^{(j)}_{a,\alpha}(x), \tag{4.5}$$

where $\eta^{(j)}$ is a vector that satisfies the following equation:

$$\eta^{(j)}_{a,\alpha}(x) = \begin{cases} \eta_{a,\alpha}(x) & (\text{for } j = t) \\ 0 & (\text{for } j \neq t) \end{cases}, \tag{4.6}$$

which is called a diluted vector. In other words, a diluted vector is a vector such that the value of j is zero when it differs from time;

$$\begin{pmatrix} \eta_{a,\alpha}(\mathbf{x},0) \\ \eta_{a,\alpha}(\mathbf{x},1) \\ \eta_{a,\alpha}(\mathbf{x},2) \\ \cdot \\ \cdot \\ \cdot \end{pmatrix} = \underbrace{\begin{pmatrix} \eta_{a,\alpha}(\mathbf{x},0) \\ 0 \\ 0 \\ 0 \\ \cdot \\ \cdot \end{pmatrix}}_{=\eta^{(0)}_{a,\alpha}(\mathbf{x},t)} + \underbrace{\begin{pmatrix} 0 \\ \eta_{a,\alpha}(\mathbf{x},1) \\ 0 \\ 0 \\ \cdot \\ \cdot \end{pmatrix}}_{=\eta^{(1)}_{a,\alpha}(\mathbf{x},t)} + \underbrace{\begin{pmatrix} 0 \\ 0 \\ \eta_{a,\alpha}(\mathbf{x},2) \\ 0 \\ \cdot \\ \cdot \end{pmatrix}}_{=\eta^{(2)}_{a,\alpha}(\mathbf{x},t)} + \cdots . \tag{4.7}$$

Thus Eq. (4.1) reads

$$\sum_{j,k} \langle\langle \eta^{(j)}_{a,\alpha}(x) \eta^{(j)*}_{b,\beta}(y) \rangle\rangle = \delta_{x,y}\delta_{a,b}\delta_{\alpha,\beta} \tag{4.8}$$

and then Eq. (4.2) becomes

$$D^{-1}(x|y)^{\alpha\beta}_{ab} = \sum_{j,k} \langle\langle (\psi^{(j)}_{a,\alpha}(x) \eta^{(k)*}_{b,\beta}(y) \rangle\rangle, \tag{4.9}$$

where $\psi^{(j)}_{a,\alpha}(x)$ is the solution of Eq. (4.3) with the right-hand side replaced by $\eta^{(j)}_{a,\alpha}(x)$. However, the terms for $j \neq k$ in Eq. (4.8) and Eq. (4.9) has zero expectation value by definition and includes only the fluctuations of the noise vector. Therefore, by dropping such terms in Eq. (4.9) by hand, we can reduce the error coming from the noise vector. That is, we evaluate

$$D^{-1}(x|y)^{\alpha\beta}_{ab} = \sum_{j} \langle\langle (\psi^{(j)}_{a,\alpha}(x) \eta^{(j)*}_{b,\beta}(y) \rangle\rangle \tag{4.10}$$

instead of Eq. (4.9).

The dilution technique can be applied to any indices of the Dirac operator, although performing the dilution for all indices eventually leads to solving D^{-1} exactly. In practice, it is likely to be more efficient to increase the number of indices for the dilution than to increase the number of samples of the noise vectors. We use the dilution technique in this thesis.

4.2 One-end trick

The one-end trick [47, 48] is an efficient method to calculate the all-to-all propagators using noise vectors. This can be applied to the correlation functions which include meson operators.

At first, we introduce the noise vector at a time slice defined as

$$\eta^{(t_0)}_{a,\alpha}(\mathbf{x}, t_x) = \delta_{t_x,t_0} \Xi_{a,\alpha}(\mathbf{x}), \tag{4.11}$$

where $\Xi_{a,\alpha}(\mathbf{x})$ is the time-independent noise vector which satisfies the following equation

$$\langle\langle \Xi_{a,\alpha}(\mathbf{x}) \Xi^{\dagger}_{b,\beta}(\mathbf{y}) \rangle\rangle = \delta_{a,b}\delta_{\alpha,\beta}\delta_{\mathbf{x},\mathbf{y}}. \tag{4.12}$$

$\eta^{(t_0)}_{a,\alpha}(\mathbf{x}, t_x)$ is equal to the original noise vector with the dilution for the time index.

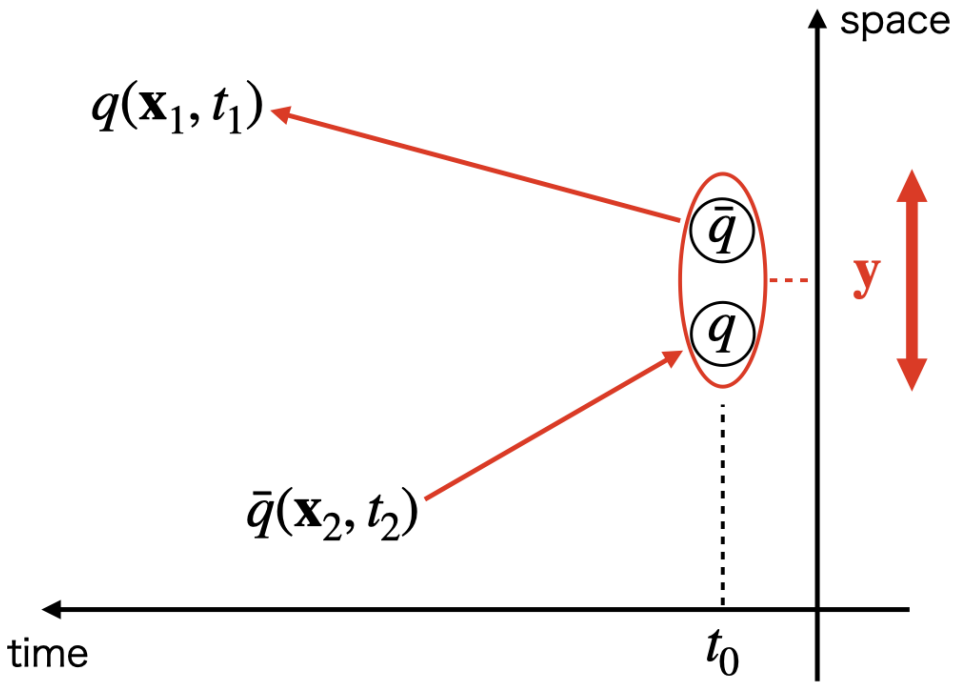

FIGURE 4.1: Quark contraction which corresponds to Eq. (4.13).

We consider the following equation:

$$\sum_{\mathbf{y},t_0} D^{-1}(x_2|\mathbf{y},t_0)^{\alpha\gamma_1}_{ab}(\Gamma)_{\gamma_1\gamma_2}D^{-1}(\mathbf{y},t_0|x_1)^{\gamma_2\beta}_{bc}, \tag{4.13}$$

where $x_1 = (\mathbf{x}_1, t_1)$, $x_2 = (\mathbf{x}_2, t_2)$, and $y = (\mathbf{y}, t_0)$, Γ is the gamma matrix including the meson operator. This is shown diagrammatically in Fig. 4.1. Here we insert the Kronecker deltas and approximate them by the noise vector at t_0 as

$$\begin{aligned}
&\sum_{\mathbf{y},t_0,\mathbf{z},t_z,t_y} D^{-1}(x_2|\mathbf{z},t_z)^{\alpha\delta}_{ad}\delta_{\delta\gamma_1}\delta_{\mathbf{z},\mathbf{y}}\delta_{t_z,t_0}\delta_{t_y,t_0}(\Gamma)_{\gamma_1\gamma_2}D^{-1}(\mathbf{y},t_y|x_1)^{\gamma_2\beta}_{bc} \\
\simeq &\sum_{\mathbf{y},t_0,\mathbf{z},t_z,t_y} D^{-1}(x_2|\mathbf{z},t_z)^{\alpha\delta}_{ad}\left(\eta^{(t_0)}_{d,\delta}(\mathbf{z},t_z)\eta^{(t_0)*}_{b,\gamma_1}(\mathbf{y},t_y)\right)(\Gamma)_{\gamma_1\gamma_2}D^{-1}(\mathbf{y},t_y|x_1)^{\gamma_2\beta}_{bc} \\
= &\sum_{t_0}(D^{-1}\eta^{(t_0)})_{a,\alpha}(x_2)\ (\eta^{(t_0)\dagger}\Gamma D^{-1})_{c,\beta}(x_1).
\end{aligned} \tag{4.14}$$

Using the γ_5-hermiticity, this reads

$$\begin{aligned}
&\sum_{t_0}(D^{-1}\eta^{(t_0)})(x_2)^{\alpha}_{a}\ (\eta^{(t_0)\dagger}\Gamma\gamma_5 D^{-1\dagger})_{c,\delta}(x_1)(\gamma_5)_{\delta\beta} \\
&= \sum_{t_0}(D^{-1}\eta^{(t_0)})(x_2)^{\alpha}_{a}\ (D^{-1}\gamma_5\Gamma^{\dagger}\eta^{(t_0)})^{*}_{c,\delta}(x_1)\ (\gamma_5)_{\delta\beta}
\end{aligned} \tag{4.15}$$

From the above, Eq. (4.13) can be approximately calculated as follows.

- Create a noise vector $\eta^{(t_0)}$ at the timeslice t_0.

- Solve the following two linear equations:

$$\begin{aligned} D\psi^{(t_0)} &= \eta^{(t_0)}, \\ D\chi^{(t_0)} &= \gamma_5\Gamma^\dagger\eta^{(t_0)}. \end{aligned} \tag{4.16}$$

- Eq. (4.13) can be expressed as

$$\sum_{\mathbf{y},t_0} D^{-1}(x_2|\mathbf{y},t_0)_{\substack{\alpha\gamma_1\\ab}}(\Gamma)_{\gamma_1\gamma_2}D^{-1}(\mathbf{y},t_0|x_1)_{\substack{\gamma_2\beta\\bc}} \simeq \sum_{t_0}\psi^{(t_0)}_{a,\alpha}(x_2)\chi^{(t_0)\dagger}_{c,\delta}(x_1)(\gamma_5)_{\delta\beta} \tag{4.17}$$

Since this method uses only one noise vector for two all-to-all propagators, it reduces fluctuations due to the noise vectors. Also, for $\Gamma = \gamma_5$, the lower equation in Eq. (4.16) is equivalent to the upper one. Thus we solve only one linear equation for one noise vector.

From the calculation for the $I = 1$ $\pi\pi$ system [22], the one-end trick has turned out to be efficient for the HAL QCD method together with all-to-all propagator calculations.

4.3 Covariant approximation averaging

The covariant approximation averaging (CAA) [50] is a method that uses the correlation functions both with and without the approximation to increase statistics with a low computational cost.

In this section, we first explain the covariant approximation averaging, and then present the combined method with the truncation solver method [51], namely the all-mode averaging without low modes, which is employed in this thesis.

4.3.1 General idea

First, we consider the operator $O[U]$ with the gauge configuration U, and the discrete symmetry transformation $g \in G$ that satisfies the following two requests:

- There exists a operator $O^g[U]$ which holds

$$O[U^g] = O^g[U], \tag{4.18}$$

  where U^g is the gauge configuration transformed under g. That is, $O[U]$ is covariant under g.

- The operator O satisfies

$$\langle O[U]\rangle = \langle O[U^g]\rangle. \tag{4.19}$$

  That is, the theory has the symmetry G.

For example, a hadron operator and the discrete translation which keeps the lattice invariant satisfy both conditions.

We define $O_G[U]$ as

$$O_G[U] = \frac{1}{N_G}\sum_{g\in G} O[U^g] = \frac{1}{N_G}\sum_{g\in G} O^g[U], \tag{4.20}$$

where N_G denotes the rank of G. For the discrete translation, the above equation corresponds to taking an average of the correlation functions with the hadron operators at different spatial positions.

Using the condition introduced above, we obtain

$$\langle O_G[U] \rangle = \left\langle \frac{1}{N_G} \sum_{g \in G} O^g[U] \right\rangle = \langle O[U] \rangle. \tag{4.21}$$

In the lattice calculation, the expectation value is obtained by taking an average over the gauge configurations;

$$\langle O[U] \rangle \approx \frac{1}{N_U} \sum_U O[U], \tag{4.22}$$

$$\left\langle \frac{1}{N_G} \sum_{g \in G} O^g[U] \right\rangle \approx \frac{1}{N_U} \sum_U \frac{1}{N_G} \sum_{g \in G} O^g[U]. \tag{4.23}$$

From Eq. (4.21), we can use Eq. (4.23) as an estimator of $\langle O[U] \rangle$ instead of Eq. (4.22). In this method, many data are used, as seen in Eq. (4.23), which leads to increasing the statistics. However, calculating Eq. (4.23) is not efficient because it simply enhances the computation cost by a factor of N_G.

Here we define $O^{(\text{appx})}$ as an approximation of O, and define $O_G^{(\text{appx})}$ as

$$O_G^{(\text{appx})} = \frac{1}{N_G} \sum_{g \in G} O^{(\text{appx})g}. \tag{4.24}$$

We assume that $O^{(\text{appx})}$ and $O^{(\text{appx})g}$ also satisfy the assumptions Eq. (4.18) and Eq. (4.19), and have lower computational cost than for O. In the covariant approximation averaging, we calculate the expectation value of the following quantity as an estimator of $\langle O[U] \rangle$:

$$O^{(\text{imp})} = O - O^{(\text{appx})} + O_G^{(\text{appx})}. \tag{4.25}$$

Indeed, applying Eq. (4.21) to $O_G^{(\text{appx})}$, the expectation value of the above equation reads

$$\begin{aligned} \langle O^{(\text{imp})} \rangle &= \langle O \rangle - \langle O^{(\text{appx})} \rangle + \langle O_G^{(\text{appx})} \rangle \\ &= \langle O \rangle - \langle O^{(\text{appx})} \rangle + \langle O^{(\text{appx})} \rangle \\ &= \langle O \rangle, \end{aligned} \tag{4.26}$$

indicating that $O^{(\text{imp})}$ is the correct estimator. Since the computational cost for $O^{(\text{appx})}$ and $O_G^{(\text{appx})}$ is low, this method can increase statistics for the reasonable computational cost.

4.3.2 The CAA combined with the truncation solver method

Here we explain the CAA combined with the truncation solver method, namely all-mode averaging (AMA) without low modes. In this method, we employ $O^{(\text{appx})}$ as

$$O^{(\text{appx})} = O[D_{\text{appx}}^{-1}[U]], \tag{4.27}$$

where D^{-1}_{appx} is the fermion propagator approximated by relaxing the condition to terminate the iteration algorithms to calculate Eq. (2.69) such as the CG method. Thus it is obvious that the computational cost of D^{-1}_{appx} is lower than that of the original propagator, while the calculation of D^{-1}_{appx} is less accurate than the original one.

There are two choices for the condition to terminate the iterations: one is the number of iterations N_{iter} itself, and the other is the convergence condition that the iteration terminates when g satisfies $|Dg - s|/|s| < \epsilon$ for a certain value ϵ. In the actual calculation, we relax these conditions by setting smaller N_{iter} or larger ϵ.

We can apply the method to the bi-conjugate gradient (Bi-CG) method. However, when we relax the convergence condition of the Bi-CG method, we have to be careful about the possibility of breaking the covariance of $O^{(\text{appx})}$. Since the Bi-CG method does not reduce the residual vector monotonically to zero, the magnitude of the approximation may differ among the gauge configurations. Thus the covariance of $O^{(\text{appx})}$ may be broken and $O^{(\text{imp})}$ may not be the correct estimator. In practice, it is shown that such an effect is not significant. In addition, there is an alternative method to avoid the problem even in the Bi-CG method (see Appendix C in Ref. [50] for more details). In this study, we use the alternative method for all analyses in this thesis.

Chapter 5

S-wave kaon–nucleon potentials with all-to-all propagators in the HAL QCD method

In this chapter, we show the analysis of the S-wave nucleon-kaon (NK) interactions, where there exists no quark pair creation and annihilation. We use the all-to-all propagators to employ the hadron operators with zero momenta at both source and sink. As a calculation technique for such propagators, the one-end trick combined with the CAA is used. In this study, we focus on the efficiency of the technique of the all-to-all propagator calculation.

There are several previous calculations in the finite volume method for NK systems [52–56], while a few previous studies have been done in the HAL QCD method [57, 58].

The existence of the pentaquark called $\Theta^+(1540)$ in S-wave NK systems ($I(J^P) = 0(1/2^-)$ and $1(1/2^-)$) is also of interest. The first discovery of $\Theta^+(1540)$ was reported by LEPS Collaboration at SPring-8 [59]. Although the current Particle Data Group shows the negative conclusion for its existence and does not list it in the table [60], it is important to see $\Theta^+(1540)$ from the first-principle calculation of QCD, that is, the lattice QCD. In this study, we search for signals corresponding to $\Theta^+(1540)$ from our results of the phase shifts.

5.1 Hadron operators and 4-point correlation functions for S-wave NK systems

We use the hadron operators defined as

$$\begin{aligned} K^+(x) &= i\bar{s}(x)\gamma_5 u(x), \quad K^-(x) = i\bar{u}(x)\gamma_5 s(x), \\ K^0(x) &= i\bar{s}(x)\gamma_5 d(x), \quad \bar{K}^0(x) = i\bar{d}(x)\gamma_5 s(x), \\ N_\alpha(x) &= \epsilon_{abc} q_{a,\alpha}(x)(u_b^{\mathrm{T}}(x) C\gamma_5 d_c(x)), \end{aligned} \tag{5.1}$$

where $N = (p, n)$ and $q = (u, d)$. We take only the upper components of the spinor indices ($\alpha, \beta = 1, 2$) in the Dirac representation, which corresponds to the even parity.

The 4-point correlation function for the S-wave NK system with the isospin $I = 1$ is given by

$$F^{I=1}_{\alpha\beta}(\mathbf{r}, t; \mathbf{z}_0, t_0) = \langle J^{I=1}_\alpha(\mathbf{r}, t + t_0) \bar{J}^{I=1}_\beta(\mathbf{z}_0, t_0) \rangle, \tag{5.2}$$

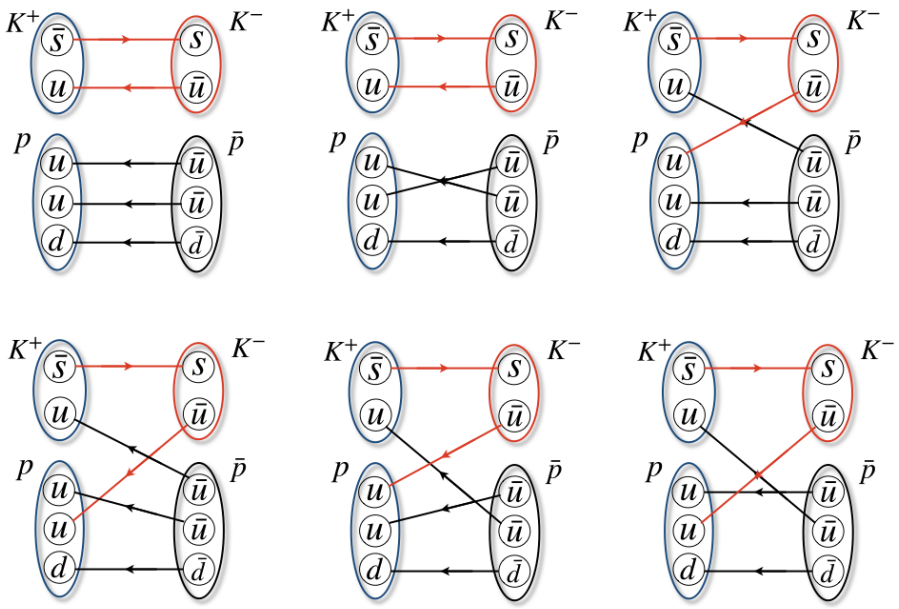

FIGURE 5.1: Quark contraction diagrams for the $I = 1$ NK system. Operators on the left-hand and right-hand sides are sink and source operators, respectively. All-to-all propagators are represented as red lines while point-to-all propagators are shown as black lines.

where $J^{I=1}$ is the sink operator given by

$$\begin{aligned} J^{I=1}_{\alpha}(\mathbf{r}, t+t_0) &= \sum_{\mathbf{x}} K^+(x_1)\, p_\alpha(x_2) \\ &= i \sum_{\mathbf{x}} (\bar{s}(x_1)\gamma_5 u(x_1))\ (\epsilon_{abc} u_{a,\alpha}(x_2)(u_b^{\mathrm{T}}(x_2) C\gamma_5 d_c(x_2)) \end{aligned} \tag{5.3}$$

and $\bar{J}^{I=1}$ is the source operator by

$$\begin{aligned} \bar{J}^{I=1}_{\beta}(\mathbf{z}_0, t_0) &= \sum_{\mathbf{y}} K^-(y)\bar{p}_\beta(z_0) \\ &= -i \sum_{\mathbf{y}} (\bar{u}(y)\gamma_5 s(y))\ (\epsilon_{a'b'c'} \bar{u}_{a',\beta}(z_0)(\bar{u}_{b'}(z_0) C\gamma_5 \bar{d}^{\mathrm{T}}_{c'}(z_0)). \end{aligned} \tag{5.4}$$

Here, $x_1 = (\mathbf{r}+\mathbf{x}, t+t_0)$, $x_2 = (\mathbf{x}, t+t_0)$, $y = (\mathbf{y}, t_0)$, and $z_0 = (\mathbf{z}_0, t_0)$. We take summation over $\mathbf{y}$ for K^- to have zero momentum, and choose $K^+ p_\alpha$ with zero total momentum by summing over $\mathbf{x}$ in Eq. (5.3). In this case, thanks to the conservation of the total momentum, $\bar{p}$ automatically has zero momentum even if $\mathbf{z}_0$ is fixed.

We show in Fig. 5.1 the quark contraction diagrams for the $I = 1$ NK, where there is no quark pair creation and annihilation. Nevertheless, the all-to-all propagators are needed for red lines in Fig. 5.1 due to the summation over the spatial coordinate of the K^- operator (red circles in Fig. 5.1).

For the $I = 0$ channel, the 4-point correlation function is given by

$$F^{I=0}_{\alpha\beta}(\mathbf{r}, t; \mathbf{z}_0, t_0) = \langle J^{I=0}_{\alpha}(\mathbf{r}, t + t_0) \bar{J}^{I=0}_{\beta}(\mathbf{z}_0, t_0) \rangle, \tag{5.5}$$

where

$$\begin{aligned} J^{I=0}_{\alpha}(\mathbf{r}, t + t_0) &= \sum_{\mathbf{x}} (K^0(x_1)\, p_\alpha(x_2) - K^+(x_1)\, n_\alpha(x_2)) \\ &= i \sum_{\mathbf{x}} [(\bar{s}(x_1)\gamma_5 d(x_1))\ (\epsilon_{abc} u_{a,\alpha}(x_2)(u^{\mathrm{T}}_b(x_2) C\gamma_5 d_c(x_2)) \\ &\quad -(\bar{s}(x_1)\gamma_5 u(x_1))\ (\epsilon_{abc} d_{a,\alpha}(x_2)(u^{\mathrm{T}}_b(x_2) C\gamma_5 d_c(x_2))] \end{aligned} \tag{5.6}$$

and

$$\begin{aligned} \bar{J}^{I=0}_{\beta}(\mathbf{z}_0, t_0) &= \sum_{\mathbf{y}} (\bar{K}^0(y)\, \bar{p}_\beta(z_0) - K^-(y)\, \bar{n}_\beta(z_0)) \\ &= -i \sum_{\mathbf{y}} [(\bar{d}(y)\gamma_5 s(y))\ (\epsilon_{a'b'c'} \bar{u}_{a',\beta}(z_0)(\bar{u}_{b'}(z_0) C\gamma_5 \bar{d}^{\mathrm{T}}_{c'}(z_0)) \\ &\quad - (\bar{u}(y)\gamma_5 s(y))\ (\epsilon_{a'b'c'} \bar{d}_{a',\beta}(z_0)(\bar{u}_{b'}(z_0) C\gamma_5 \bar{d}^{\mathrm{T}}_{c'}(z_0))] \end{aligned} \tag{5.7}$$

Thanks to the isospin symmetry in our setup, quark contraction diagrams for $F^{I=0}$ include the same ones as those in $F^{I=1}$ with different coefficients. However, $F^{I=0}$ has additional diagrams which are shown in Fig. 5.2. As is the case for $F^{I=1}$, the kaon source operators represented as red circles in Fig. 5.2 have spatial coordinates which are summed over, giving the all-to-all propagators shown by red lines.

As the all-to-all propagator calculations shown in Fig. 5.1 and Fig. 5.2, the one-end trick is used.

5.2 Simulation details

In our calculation of the NK 4-point correlation functions, we use (2+1)-flavor gauge configurations generated by PACS-CS Collaboration with the improved Iwasaki gauge action and the $\mathcal{O}(a)$-improved Wilson quark action at $\beta = 1.90$ on $32^3 \times 64$ lattice volume [11], which corresponds to $a = 0.0907(13)$ fm for the lattice spacing. The hopping parameters are $\kappa_u = \kappa_d = 0.13727$ and $\kappa_s = 0.13640$. We impose the periodic boundary condition in all spacetime directions. We used 400 configurations with 4 sources at different time slices on each configuration, and average forward and backward propagations to increase statistics. Statistical errors are estimated by the jackknife method with a binsize of 40 configurations.

To the noise vector $\eta(\mathbf{x})$ for the one-end trick, we apply the dilution for color and spinor components and the s2 dilution [61] defined by

$$\eta^{(s_{dil})}(\mathbf{x}) = \begin{cases} \eta(\mathbf{x}) & (x + y + z \equiv s_{dil} \pmod 2) \\ 0 & (x + y + z \equiv s_{dil} + 1 \pmod 2) \end{cases}, \ s_{dil} = 0, 1. \tag{5.8}$$

We employ the smeared quark source Eq. (2.71) with the parameter $(A, B) = (1.2, 0.19)$ for up and down quarks and $(A, B) = (1.2, 0.25)$ for strange quarks in lattice unit.

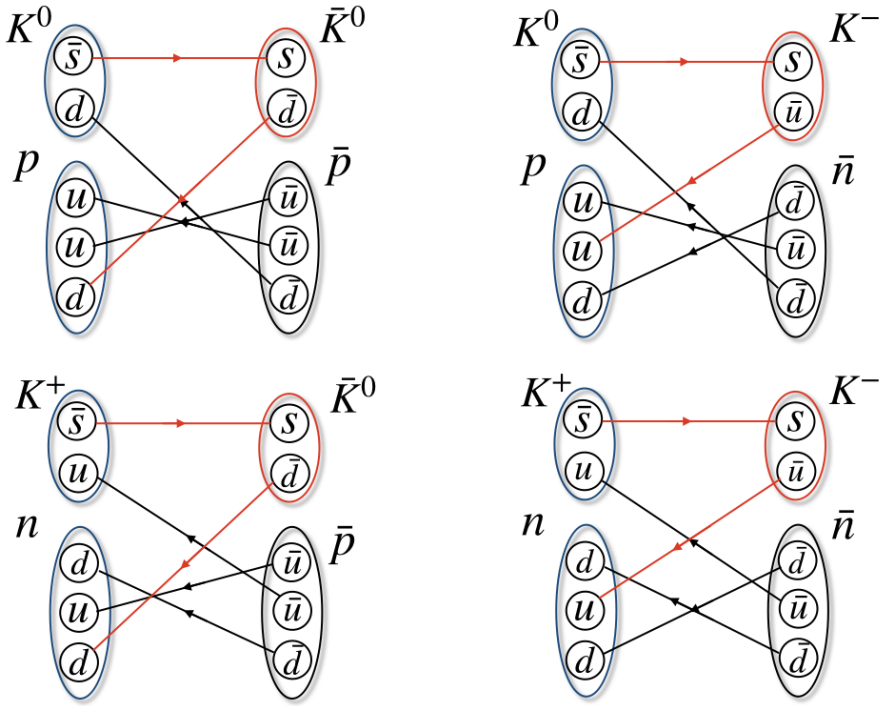

FIGURE 5.2: Quark contraction diagrams of the $I = 0$ NK 4-point correlation function. Red lines represent all-to-all propagators and black lines show point-to-all propagators.

According to the conservation law of the total angular momentum, only the diagonal part of the 4-point correlation functions $F^{I=1(0)}_{\alpha\alpha}(\mathbf{r}, t; \mathbf{z}_0, t_0)$ is the signal while others are noise. We project each spin component of $F^{I=1(0)}_{\alpha\alpha}(\mathbf{r}, t; \mathbf{z}_0, t_0)$ onto the A_1^+ representation of the cubic group O_h, which is associated with the S-wave NBS wave functions (for the details of the cubic group, see Appendix C). Furthermore, since both spin components produce the same leading-order potentials, we take an average over them. For the truncation of the summation in Eq. (3.64), we take $k \leq 2$ for both isospin channels.

We apply the CAA combined with the truncated solver method. For the transformation $g \in G$, we employ the translation of the spatial coordinate of the nucleon source operator: $\Delta\mathbf{z_0} = (0,0,0), (0,0,16), \cdots, (16,16,16)$. In this case, the number of elements of the translation $N_G = 8$. The terminate condition of the Bi-CG solver is set to $\epsilon = 10^{-12}$ as the exact ones, followed by the approximated evaluations with $\epsilon = 10^{-4}$. We employ the method to keep the covariance by choosing the location before the translation $\mathbf{z_0}$ randomly on each configuration.

We calculate the 2-point correlation functions using all-to-all propagators together with the calculation by the one-end trick for the mesons while point-to-all propagators for the nucleons. Also, we employ the smearing to quarks at the source in the same way as for the 4-point correlation functions. The results of the hadron masses are $m_\pi \approx 570$ MeV, $m_K \approx 713$ MeV, and $m_N \approx 1405$ MeV.

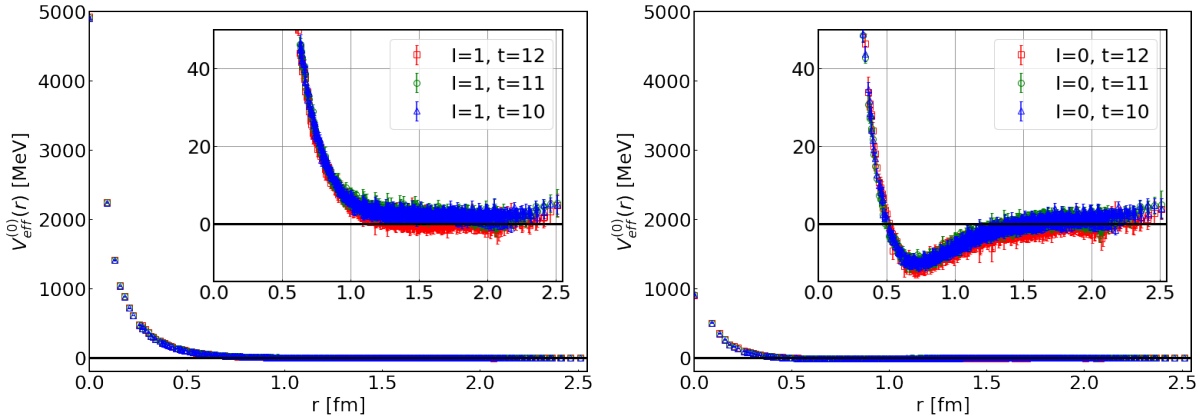

FIGURE 5.3: The leading-order potentials $V_0(r)$ for $I = 1$ (Left) and $I = 0$ (Right) NK systems at $t = 10$–12.

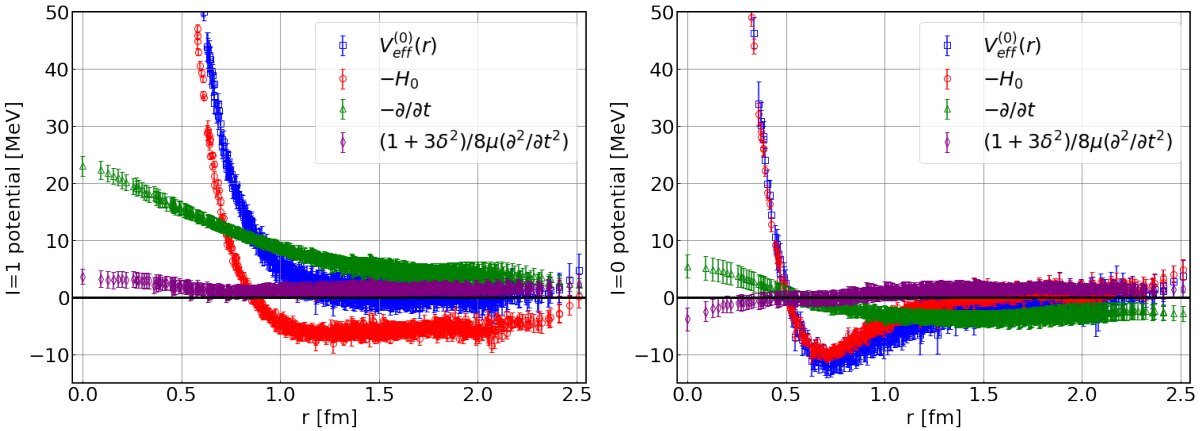

FIGURE 5.4: The potentials and the terms in Eq. (3.64) at $t = 12$ for $I = 1$ (Left) and $I = 0$ (Right).

I	a_0 [MeV]	a_1 [fm]	a_2 [MeV]	a_3 [fm]	a_4 [MeV]	a_5 [fm]	a_6 [MeV]	a_7 [fm]
1	3180(193)	0.08(0.00)	1185(17)	0.18(0.02)	501(97)	0.36(0.08)	61(111)	0.70(0.36)
0	352(121)	0.08(0.01)	381(86)	0.15(0.03)	189(34)	0.33(0.03)	-23(8)	0.90(0.22)

TABLE 5.1: Results of the fit parameters a_i for the potentials at $t = 12$. We employ the uncorrelated fit. $\chi^2/dof = 0.65(0.19)$ for $I = 1$ and $\chi^2/dof = 0.27(0.09)$ for $I = 0$.

5.3 Numerical results

5.3.1 Leading-order potentials

Fig. 5.3 represents the leading-order potentials for the S-wave NK systems at $t = 10$–12. In this time region, the effective masses of both the kaon and nucleon 2-point correlation functions are saturated. Also, both the $I = 1$ and $I = 0$ potentials have very weak t-dependences at the timeslices, which indicates that the contributions from the inelastic states and the higher-order terms in the derivative expansion are well suppressed. In addition, both potentials become zero within errors at long distances ($1.5 < r < 2.5$ fm), indicating the negligible finite volume effect.

The $I = 1$ potential is repulsive everywhere with the repulsive core at short distances ($0 < r < 0.5$ fm), while the $I = 0$ potential has a repulsive core at short distances and a shallow attractive pocket with a depth of about 10 MeV at the middle distances ($0.5 < r < 1.5$ fm). The repulsive core of the $I = 1$ potential is much stronger than that of the $I = 0$ potential.

Fig. 5.4 shows the potentials and their breakups into the laplacian term and the two time-derivative terms in Eq .(3.64) at $t = 12$. The 2nd time-derivative terms (purple diamonds) are small, indicating that the $\mathcal{O}(\Delta W^3)$ corrections in Eq. (3.64), which are ignored in our calculation, are expected to be further reduced. Indeed we find that the potentials with and without these corrections give almost identical results on the phase shifts.

5.3.2 Phase shifts

We use the potentials at $t = 12$ in the fitting. As the fit function, we employ the sum of four Gaussians given by

$$V(r) = a_0 e^{-(r/a_1)^2} + a_2 e^{-(r/a_3)^2} + a_4 e^{-(r/a_5)^2} + a_6 e^{-(r/a_7)^2}, \tag{5.9}$$

where we assume that $a_1 < a_3 < a_5 < a_7$. Table 5.1 lists the results of the fit parameters and Fig. 5.5 depicts the curves of the functions Eq. (5.9) with the parameters.

We solve the Schrödinger equation in the radial direction as

$$-\frac{1}{2\mu}\left(\frac{1}{r}\frac{\mathrm{d}^2}{\mathrm{d}r^2}r - \frac{l(l+1)}{r^2}\right)\psi_R^{l,E}(r) + V(r)\psi_R^{l,E}(r) = \frac{k^2}{2\mu}\psi_R^{l,E}(r), \tag{5.10}$$

where k is the relative momentum, $V(r)$ is the fitted potential, and the angular momentum is set to $l = 0$ for the S-wave channel. The total energy E is related to k^2 as $E = \sqrt{k^2 + m_N^2} + \sqrt{k^2 + m_K^2}$. We then extract a scattering phase shift from its solution. Finally, by varying k^2 (or E), we determine an energy dependence of the scattering phase shift.

We show in Fig. 5.6 the results of the phase shifts as functions of the momentum of the kaon in the laboratory frame P_{lab}. The $I = 1$ phase shift is negative in all the energy regions due to the repulsion of the potential at all distances. On the other hand, the $I = 0$ phase shift

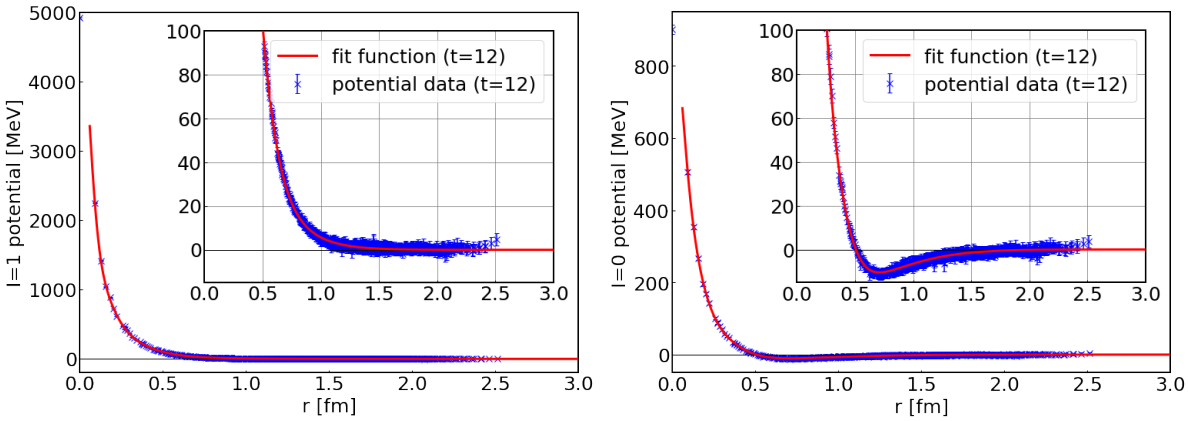

FIGURE 5.5: The fitted potentials (Red lines) for $I = 1$ (Left) and $I = 0$ (Right) at $t = 12$. Blue crosses show the potential data at $t = 12$.

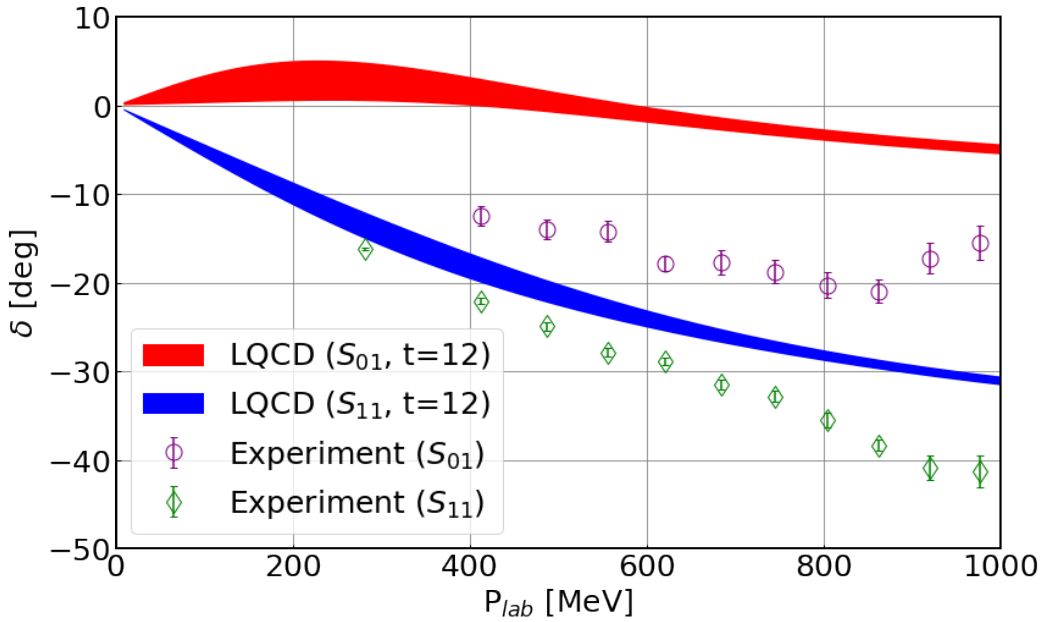

FIGURE 5.6: The S-wave NK scattering phase shifts for $I = 1$ (blue band) and $I = 0$ (red band). The experimental results [62] are plotted by green diamonds for $I = 1$ and by purple circles for $I = 0$.

becomes slightly positive in the low energy region ($0 < P_{lab} < 400$ MeV), coming from the small attractive pocket in the potential, and then turns into negative in the higher energy region ($400 < P_{lab} < 1000$ MeV) due to the repulsion at a short distance. The qualitative behavior of the scattering phase shifts is consistent with that of the experimental results [62]: both the lattice and experimental results decrease as P_{lab} increases, and the $I = 1$ channel is negatively larger than the $I = 0$ channel. At the quantitative level, however, our results are smaller in magnitude than the experimental ones, which is probably due to the difference of the pion mass, 570 MeV in this study and 140 MeV in Nature.

For the comparison to the previous theoretical studies, in the constituent quark model of hadrons [63], both the $I = 1$ and $I = 0$ channels have the repulsive behavior, although the small attraction in the $I = 0$ channel, which can be seen in our results, has not been predicted. The lattice QCD studies in the finite volume method at the lighter pion masses [54–56] give similar but more negative phase shifts than ours. These suggest the absence of the attractive pocket in the $I = 0$ potential at the lighter quark mass. Furthermore, the previous study by the HAL QCD method with the wall source at $m_\pi \approx 700$ MeV [58][1], which is slightly heavier than that in our study, gives the $I = 1$ phase shifts consistent with our study within errors. The deviation may be explained by the difference of the quark masses or by the systematic uncertainty due to the higher-order contributions in the derivative expansion.

For the existence of the pentaquark $\Theta^+(1540)$, we do not observe any behaviors of phase shifts corresponding to resonances or bound states in both channels. Indeed we find that the phase shifts do not pass 90 degrees, which typically indicates an existence of a resonant state. Also, the phase shifts approach zero when we increase P_{lab}, which indicates that no bound states appear according to the Levinson's theorem. These suggests that $\Theta^+(1540)$ does not exist in the S-wave NK systems ($I(J^P) = 0(1/2^-)$ and $1(1/2^-)$ channels) for the quark masses corresponding to $m_\pi \approx 570$ MeV.

[1] There is also an unpublished study with the same technique at $m_\pi \approx 570$ MeV. We have found that the phase shift results are almost the same as those at $m_\pi \approx 700$ MeV.

Chapter 6

Lattice QCD studies on Δ and Ω baryons as meson-baryon bound states in the HAL QCD method

In this chapter, we investigate P-wave $I = 3/2$ $N\pi$ and $I = 0$ $\Xi\bar{K}$ scatterings, which couple to Δ and Ω baryons, respectively, as a first step towards the studies on meson-baryon scatterings having the quark pair creation and annihilation in the HAL QCD method. The two baryons belong to spin $3/2$ baryons symmetric under quark flavor exchanges, called the decuplet baryons. Also, Δ baryon appears as a resonance decaying to $N\pi$ while Ω is a stable particle below the $\Xi\bar{K}$ threshold in Nature. There are several studies on Δ baryon in the other lattice QCD approaches [64–70].

In order to reduce computational costs, we employ the heavy quark masses, where u, d quark masses are close to the s quark mass. In this case, Δ baryon exists as a stable particle as well as Ω. Here, we focus on the origin of the reason why Ω is stable while Δ is resonance in Nature. It is obvious that an inequality $m_N + m_\pi - m_\Delta < m_\Xi + m_{\bar{K}} - m_\Omega$ holds in Nature because the left-hand side is negative while the right-hand side is positive. Furthermore, as seen in the previous lattice QCD results [11], this still holds in the setup with the heavier quark masses. Therefore, we investigate the rephrased question, "what physical origin causes this hierarchy?" in the latter setup. The HAL QCD method, which extracts the interaction potentials directly, enables us to distinguish two possible origins of the hierarchy: one from the difference in interactions and another from the difference in kinematics. We extract the $N\pi$ and $\Xi\bar{K}$ potential in the HAL QCD method and compare them.

6.1 Three-point correlation functions with single-baryon source operators

In order to investigate P-wave $I = 3/2$ $N\pi$ and $I = 0$ $\Xi\bar{K}$ scatterings in the HAL QCD method, we calculate the following 3-point correlation functions,

$$F^{N\pi}_{\alpha,j_z}(\mathbf{r},t) = \langle \pi^+(\mathbf{r}+\mathbf{x}, t+t_0) p_\alpha(\mathbf{x}, t+t_0)\ \bar{\Delta}^{++}_{j_z}(t_0)\rangle, \tag{6.1}$$

$$F^{\Xi\bar{K}}_{\alpha,j_z}(\mathbf{r},t) = \langle \frac{1}{\sqrt{2}}(K^-(\mathbf{r}+\mathbf{x}, t+t_0)\Xi^0_\alpha(\mathbf{x}, t+t_0) - \bar{K}^0(\mathbf{r}+\mathbf{x}, t+t_0)\Xi^-_\alpha(\mathbf{x}, t+t_0))\ \bar{\Omega}^-_{j_z}(t_0)\rangle, \tag{6.2}$$

where sink operators are defined by

$$\begin{aligned}
&\pi^+(x) = -i\bar{d}(x)\gamma_5 u(x), \quad \bar{K}^0(x) = -i\bar{d}(x)\gamma_5 s(x), \quad K^-(x) = i\bar{u}(x)\gamma_5 s(x),\\
&p_\alpha(x) = \epsilon_{abc} u_{a,\alpha}(x)(u_b^{\mathrm{T}}(x) C\gamma_5 d_c(x)),\\
&\Xi^0_\alpha(x) = \epsilon_{abc} s_{a,\alpha}(x)(s_b^{\mathrm{T}}(x) C\gamma_5 u_c(x)), \quad \Xi^-_\alpha(x) = \epsilon_{abc} s_{a,\alpha}(x)(s_b^{\mathrm{T}}(x) C\gamma_5 d_c(x)).
\end{aligned} \tag{6.3}$$

We employ 3-quark-type decuplet baryon operators at the source given by

$$\begin{aligned}
D_{+\frac{3}{2}}(t_0) &= \sum_{\mathbf{z}} \epsilon_{abc}(q_b^T(\mathbf{z},t_0)\Gamma_+ q_c(\mathbf{z},t_0)) q_{a,0}(\mathbf{z},t_0),\\
D_{+\frac{1}{2}}(t_0) &= \frac{1}{\sqrt{3}}\sum_{\mathbf{z}} \epsilon_{abc}[\sqrt{2}(q_b^T(\mathbf{z},t_0)\Gamma_z q_c(\mathbf{z},t_0)) q_{a,0}(\mathbf{z},t_0) + (q_b^T(\mathbf{z},t_0)\Gamma_+ q_c(\mathbf{z},t_0)) q_{a,1}(\mathbf{z},t_0)],\\
D_{-\frac{1}{2}}(t_0) &= \frac{1}{\sqrt{3}}\sum_{\mathbf{z}} \epsilon_{abc}[\sqrt{2}(q_b^T(\mathbf{z},t_0)\Gamma_z q_c(\mathbf{z},t_0)) q_{a,1}(\mathbf{z},t_0) + (q_b^T(\mathbf{z},t_0)\Gamma_- q_c(\mathbf{z},t_0)) q_{a,0}(\mathbf{z},t_0)],\\
D_{-\frac{3}{2}}(t_0) &= \sum_{\mathbf{z}} \epsilon_{abc}(q_b^T(\mathbf{z},t_0)\Gamma_- q_c(\mathbf{z},t_0)) q_{a,1}(\mathbf{z},t_0),
\end{aligned} \tag{6.4}$$

with $\Gamma_\pm = \frac{1}{2}C(\gamma_2 \pm i\gamma_1)$ and $\Gamma_z = \frac{-i}{\sqrt{2}}C\gamma_3$, and $q = (u, s)$ for $D = (\Delta^{++}, \Omega^-)$, respectively. All the source operators in Eq. (6.4) belong to an H_g irreducible representation of the cubic group O_h^D, corresponding to the angular momentum $J^P = 3/2^+$, with different components.

To obtain NBS wave functions with $J^P = 3/2^+$, we project $F_{\alpha,j_z}(\mathbf{r},t)$ onto the same component in the H_g representation of $\bar{D}_{j_z}(t_0)$. For the details, see Appendix C. The projected 3-point correlation functions can be decomposed into the spherical harmonics $Y_{l,m}(\hat{\mathbf{r}})$ and a factor $f_{j_z}(r,t)$ that depends only on $r = |\mathbf{r}|$ and t as

$$\begin{aligned}
&\begin{pmatrix} F_{\uparrow,+\frac{3}{2}}(\mathbf{r},t) \\ F_{\downarrow,+\frac{3}{2}}(\mathbf{r},t) \end{pmatrix} = f_{+\frac{3}{2}}(r,t)\begin{pmatrix} Y_{1,+1}(\hat{\mathbf{r}}) \\ 0 \end{pmatrix}, \quad \begin{pmatrix} F_{\uparrow,+\frac{1}{2}}(\mathbf{r},t) \\ F_{\downarrow,+\frac{1}{2}}(\mathbf{r},t) \end{pmatrix} = f_{+\frac{1}{2}}(r,t)\begin{pmatrix} \sqrt{\frac{2}{3}}Y_{1,0}(\hat{\mathbf{r}}) \\ \sqrt{\frac{1}{3}}Y_{1,+1}(\hat{\mathbf{r}}) \end{pmatrix},\\
&\begin{pmatrix} F_{\uparrow,-\frac{1}{2}}(\mathbf{r},t) \\ F_{\downarrow,-\frac{1}{2}}(\mathbf{r},t) \end{pmatrix} = f_{-\frac{1}{2}}(r,t)\begin{pmatrix} \sqrt{\frac{1}{3}}Y_{1,-1}(\hat{\mathbf{r}}) \\ \sqrt{\frac{2}{3}}Y_{1,0}(\hat{\mathbf{r}}) \end{pmatrix}, \quad \begin{pmatrix} F_{\uparrow,-\frac{3}{2}}(\mathbf{r},t) \\ F_{\downarrow,-\frac{3}{2}}(\mathbf{r},t) \end{pmatrix} = f_{-\frac{3}{2}}(r,t)\begin{pmatrix} 0 \\ Y_{1,-1}(\hat{\mathbf{r}}) \end{pmatrix}.
\end{aligned} \tag{6.5}$$

Thus we extract $f_{j_z}(r,t)$ using a projection to $(l = 1, m)$, defined on a discrete space as

$$f_{j_z}(r,t) = \frac{\sum_{\mathbf{r}'\in\{\mathbf{r}'|r'=r\}} Y^*_{1m}(\hat{\mathbf{r}}') F_{\alpha,j_z}(\mathbf{r}',t)}{\sum_{\mathbf{r}'\in\{\mathbf{r}'|r'=r\}} Y^*_{1,m}(\hat{\mathbf{r}}') Y_{1m}(\hat{\mathbf{r}}')} \tag{6.6}$$

with corresponding (m,α) for each j_z. For $j_z = \pm 1/2$, we can derive $f_{j_z}(r,t)$ in two ways by setting either $(m,\alpha) = (0,\uparrow)$ or $(1,\downarrow)$ for $j_z = +1/2$ and either $(m,\alpha) = (0,\downarrow)$ or $(-1,\uparrow)$ for $j_z = -1/2$, respectively. In this study, we take an average of the factors calculated from the two choices.

Using Eq. (6.5), we obtain an equation alternative to Eq. (3.64);

$$V^{\mathrm{LO}}(r) \simeq \frac{1}{\mathcal{R}_{j_z}(r,t)}\left[\sum_{k=1}^{\infty} C^{(k)}_{m_M,m_B}\left(-\frac{\partial}{\partial t}\right)^k + \frac{1}{2\mu}\left(\frac{1}{r}\frac{\partial^2}{\partial r^2}r - \frac{l(l+1)}{r^2}\right)\right]\mathcal{R}_{j_z}(r,t), \tag{6.7}$$

where the angular momentum $l = 1$ and

$$\mathcal{R}_{j_z}(r,t) = \frac{f_{j_z}(r,t)}{C_M(t)C_B(t)} \tag{6.8}$$

with the meson and baryon 2-point function $C_M(t)$ and $C_B(t)$, respectively. We use this equation to extract the LO potentials in this study. Since $f_{j_z}(r,t)$ for any j_z gives the same LO potential, we take an average over j_z to increase statistics. Furthermore, a charge conjugation symmetry provides a relations among $f_{j_z}(r,t)$ as

$$f_{+\frac{3}{2}}(r,t) = -f^*_{-\frac{3}{2}}(r,t), \quad f_{+\frac{1}{2}}(r,t) = -f^*_{-\frac{1}{2}}(r,t), \tag{6.9}$$

guaranteeing that an average of $f_{j_z}(r,t)$ over j_z is pure imaginary. Therefore, we ignore its real part.

6.2 Simulation details

In this numerical calculation, we employ the gauge configurations with the same setup as that for the analysis of NK systems except for the hopping parameters; we set $\kappa_u = \kappa_d = 0.13754$ and $\kappa_s = 0.13640$ in this study. A periodic boundary condition is imposed in all spacetime directions. We use 450 configurations with 16 sources at different time slices on each configuration and average forward and backward propagations to increase statistics. Statistical errors are estimated by the jackknife method with a binsize of 45 configurations.

We employ a smeared quark source with the smearing function Eq. (2.71) with $(A, B) = (1.2, 0.17)$ for light quarks and $(A, B) = (1.2, 0.25)$ for the strange quark in lattice unit. We also apply the same smearing to quarks at the sink with $(A, B) = (1.0, 1/0.7)$ to reduce singular behaviors of potentials at short distances [22], which are explained in Appendix B.

The quark contraction diagrams corresponding to Eq. (6.1) and the first term of Eq (6.2) are shown in Fig. 6.1 (Left) and Fig. 6.1 (Right), respectively. For $m_u = m_d$, the second term of Eq. (6.2) gives the same contribution as that of the first. The spatial coordinate $\mathbf{z}$ of the source operator is summed over so that it has zero momentum. In this case, quark propagators represented by red lines in this figure are all-to-all propagators. For the calculation, we use the stochastic technique together with dilutions for color/spinor/time components and the s2 (even/odd) dilution for the position $\mathbf{z}$.

We fix the spatial coordinate $\mathbf{x}$ at the sink so that the propagator which corresponds to the quark pair creation and annihilation becomes a point-to-all propagator (black line in Fig. 6.1). Also, we employ the CAA combined with the truncated solver method using the translational invariance of $\mathbf{x}$: $\Delta\mathbf{x} = (0,0,0), (0,0,8), \cdots, (24,24,24)$. The number of elements $N_G = 64$ in this case. For the specific value of $\mathbf{x}$, we choose it randomly for each gauge configuration, as is the case of the S-wave NK scatterings.

Meson 2-point correlation functions are calculated using all-to-all propagators, where the one-end trick is employed, while baryon 2-point correlation functions are calculated using point-to-all propagators. Also, both in the meson and baryon 2-point functions, we employ the smearing to quarks at the source and the sink in the same way as for the 3-point correlation functions. We extract the masses of single hadrons obtained from them in this setup, which are listed in Table 6.1. Since Δ and Ω masses lie below $N\pi$ and $\Xi\bar{K}$ threshold energies, respectively, they appear as bound states in this setup.

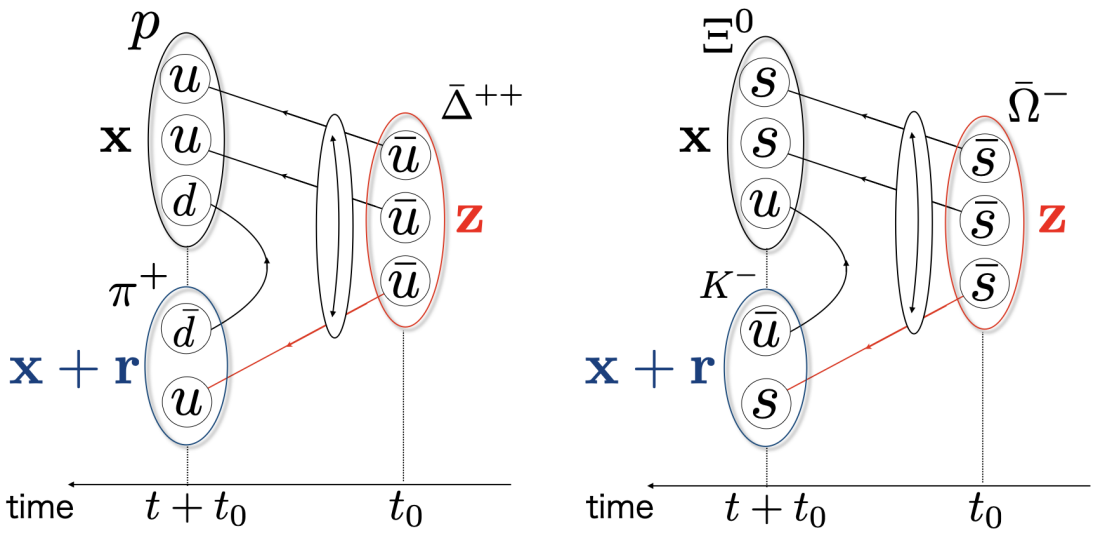

FIGURE 6.1: Quark contraction diagram corresponding to Eq. (6.1) (Left) and the first term in Eq. (6.2) (Right). A circle with a two-way arrow across three lines indicates permutations of quark contractions among them. All-to-all and point-to-all propagators are used in red lines and black lines, respectively.

hadron	π	K	N	Ξ	Δ	Ω
mass	411.2(1.7)	635.1(1.5)	1217.2(4.7)	1505.3(4.5)	1522.9(7.8)	1847.0(6.5)
fit range	[10,30]	[10,30]	[7,20]	[7,20]	[6,15]	[6,20]

TABLE 6.1: Hadron masses in unit of MeV estimated by fitting 2-point functions. The second row shows temporal fitting ranges in lattice unit.

For the truncation of the summation over k in Eq. (6.7), we set $k \leq 2$ for $N\pi$ and $k \leq 3$ for $\Xi\bar{K}$, respectively. We checked that the higher-order contributions are negligible.

6.3 Numerical results

6.3.1 Leading-order potentials

In Fig. 6.2, we present LO potentials for $N\pi$ system at $t = 8$–10 and $\Xi\bar{K}$ system at $t = 8$–11, where effective masses of Δ and Ω reach plateaux, respectively. We do not observe significant t-dependence of potentials, indicating that the contributions from the inelastic states and the higher-order terms in the derivative expansion are well under control.

Both potentials have very strong attractions at short distances ($r \lesssim 0.5$ fm), which can be responsible for producing bound states associated with Δ and Ω. The attraction of the $N\pi$ potential is deeper than that of the $\Xi\bar{K}$ by a few thousand MeV at $r \approx 0.1$ fm.

For the shape of middle and long distances ($r \gtrsim 0.5$ fm), both potentials are similar. Here we suppose that meson-baryon interactions may be dominated by one meson exchange in this region. The $N\pi$ system exchanges a ρ meson while the $\Xi\bar{K}$ system exchanges ϕ/ω meson as well

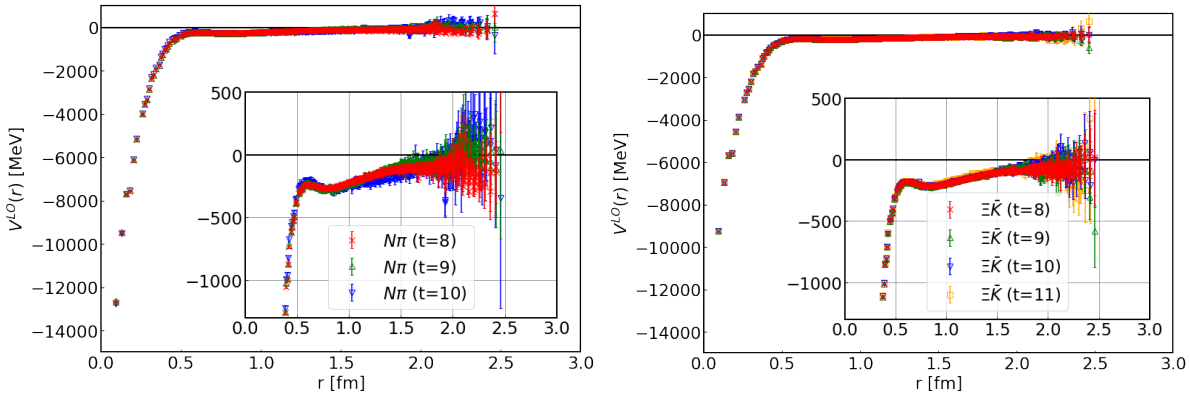

FIGURE 6.2: The LO potentials of the $N\pi$ system at $t = 8$–10 (Left) and the $\Xi\bar{K}$ system at $t = 8$–11 (Right). The laplacian terms are calculated in 4th-order accuracies.

as ρ at middle and long distances. Then we have one possibility to explain the reason for the two similar potentials that the masses of these vector mesons almost degenerate in our lattice setup near the SU(3) flavor symmetric point ($m_\rho/m_\phi \approx 0.80$) [11][1]. If this is a relevant assumption, the two potentials at middle and long distances remain to be similar even at the physical point, since the mass difference of vector mesons is not so large at the point ($m_\rho/m_\phi \approx 0.75$).

From Fig. 6.2, it seems the interaction ranges are longer than half of the box size, $L/2 \approx 1.45$ fm. We therefore carefully check the possible finite-volume effects on observables, as will be explained below.

6.3.2 Estimation of systematic uncertainties of the fitting results

We estimate systematic uncertainties in our analysis as follows.

We evaluate finite-volume effects by using the following two types of fit functions. One is a simple three Gaussians as

$$V^{3G}(\mathbf{r}) = a_0 e^{-(r/a_1)^2} + a_2 e^{-(r/a_3)^2} + a_4 e^{-(r/a_5)^2}, \tag{6.10}$$

where we assume that $a_1 < a_3 < a_5$, and the other is a three Gaussians with its 6 mirror images on the boundaries of the finite box [21] as

$$V_P^{3G}(\mathbf{r}) = V^{3G}(\mathbf{r}) + \sum_{\mathbf{n}} V^{3G}(\mathbf{r} + L\mathbf{n}), \tag{6.11}$$

where $\mathbf{n} \in \{(0,0,\pm1),(0,\pm1,0),(\pm1,0,0)\}$. For the Schrödinger equations, we use only $V^{3G}(\mathbf{r})$ with the parameters in both cases.

We estimate the contributions from the higher-order terms in the derivative expansion, by employing potentials at different t, from $t = 8$ to 10 for $N\pi$ and from $t = 8$ to 11 for $\Xi\bar{K}$.

[1] Note that this discussion is only qualitative because even the Compton wavelength of the lightest pion is 0.5 fm in this setup.

	fit potential	data at $r = a$	accuracy of ∇^2
Fit 1	$V^{3G}(\mathbf{r})$	not included	2nd order
Fit 2	$V^{3G}(\mathbf{r})$	not included	4th order
Fit 3	$V^{3G}(\mathbf{r})$	included	2nd order
Fit 4	$V^{3G}(\mathbf{r})$	included	4th order
Fit 5	$V_P^{3G}(\mathbf{r})$	not included	2nd order
Fit 6	$V_P^{3G}(\mathbf{r})$	not included	4th order
Fit 7	$V_P^{3G}(\mathbf{r})$	included	2nd order
Fit 8	$V_P^{3G}(\mathbf{r})$	included	4th order

TABLE 6.2: A list of combinations of the fitting schemes to estimate systematic uncertainties.

Finite lattice spacing effects are estimated by two approaches. The first is to evaluate the difference between the laplacian term in Eq. (6.7) calculated with 2nd- and 4th-order accuracies:

$$\begin{aligned}(\nabla^2 R(\mathbf{r}))_{\text{2nd}} &= \sum_{\mathbf{i}=\hat{\mathbf{x}},\hat{\mathbf{y}},\hat{\mathbf{z}}} \frac{R(\mathbf{r}+a\mathbf{i}) - 2R(\mathbf{r}) + R(\mathbf{r}-a\mathbf{i})}{a^2}, \\ (\nabla^2 R(\mathbf{r}))_{\text{4th}} &= \sum_{\mathbf{i}=\hat{\mathbf{x}},\hat{\mathbf{y}},\hat{\mathbf{z}}} \frac{-R(\mathbf{r}+2a\mathbf{i}) + 16R(\mathbf{r}+a\mathbf{i}) - 30R(\mathbf{r}) + 16R(\mathbf{r}-a\mathbf{i}) - R(\mathbf{r}-2a\mathbf{i})}{12a^2}.\end{aligned} \tag{6.12}$$

The second is to estimate the difference between fits with and without data at $r = a$. For the fit including data at $r = a$, we find that modification for fit functions is necessary. In fact, if we naively fit with Eqs. (6.10), (6.11), the results fail to reproduce the original potential data. This is probably due to the strong attraction at short distances together with a non-monotonic behavior at middle distances in the potentials, which makes the fitting by three Gaussians too difficult. We also observe similar difficulties for other functions such as four Gaussians or two Gaussians plus one Yukawa potential.

To avoid this difficulty, we employ interpolation combined with the usual fitting in the following way. First, we perform the fitting for the potentials without the data at $r = a, \sqrt{2}a$ with Eqs. (6.10), (6.11). Then we perform quadratic interpolation using the original data at $r = a, \sqrt{2}a$ and the fit result at $r = (\sqrt{3}a + 2a)/2$. Let the function obtained by the interpolation be $V^{\text{int}}(\mathbf{r})$. Finally, we use the following function as the potential for the Schrödinger equation:

$$V(\mathbf{r}) = \begin{cases} V^{3G}(\mathbf{r}) & (r > \frac{\sqrt{3}a+2a}{2}) \\ V^{\text{int}}(\mathbf{r}) & (r \le \frac{\sqrt{3}a+2a}{2}) \end{cases} \tag{6.13}$$

with the parameters determined in the above way. Although smoothness at $r = (\sqrt{3}a + 2a)/2$ is not guaranteed in this method, we do not find any serious non-smoothness in the results of the observables.

In summary, for potentials at a given t, there are $2 \times 2 \times 2 = 8$ combinations of fitting schemes, which are listed in Table 6.2.

As a calculation of the central values of physical observables, we use Fit 2 scheme at $t = 9$ for $N\pi$ and at $t = 10$ for $\Xi\bar{K}$. The results of the fit parameters are listed in Table 6.3, where $\chi^2/dof = 4.5$ for $N\pi$ and $\chi^2/dof = 36.0$ for $\Xi\bar{K}$, where we employ uncorrelated fit. This large χ^2/dof comes mostly from deviations between fit results and original data at short distances,

system	a_0 [MeV]	a_1 [fm]	a_2 [MeV]	a_3 [fm]	a_4 [MeV]	a_5 [fm]
$N\pi$	-13311.7(46.2)	0.24(0.00)	693.8(197.9)	0.56(0.08)	-615.3(217.7)	1.08(0.14)
$\Xi\bar{K}$	-9651.8(12.1)	0.24(0.00)	462.0(67.7)	0.60(0.04)	-427.9(72.4)	1.25(0.10)

TABLE 6.3: Fit parameters $\{a_n\}$ for potential data in Fit 2 at $t = 9$ for $N\pi$ and at $t = 10$ for $\Xi\bar{K}$, used to calculate central values of observables.

which are largely fluctuated by systematic uncertainties rather than statistical ones, even though the most problematic data at $r = a$ are excluded in the Fit 2 scheme. Systematic errors are estimated from the results in other fitting schemes and at other timeslices.

Fig. 6.3 presents original data by red crosses and fitting results by blue bands. The dark blue bands correspond to statistical errors in the Fit 2 scheme at $t = 9$ for $N\pi$ and at $t = 10$ for $\Xi\bar{K}$, whereas light blue bands show statistical and systematic errors added in quadrature, where the latter error is estimated from other fitting schemes and t dependences. Note that systematic uncertainties at short distances, mainly caused by finite lattice spacing effects, are much larger than those at long distances, dominantly caused by finite-volume effects.

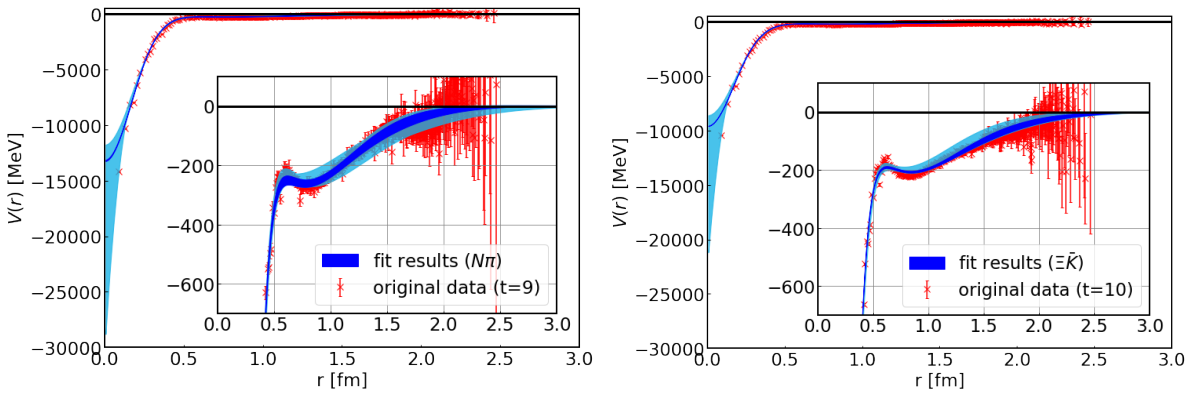

FIGURE 6.3: Fit results for $N\pi$ (Left) and $\Xi\bar{K}$ (Right). Dark (light) blue bands show statistical errors (statistical and systematic errors added in quadrature). Systematic errors are estimated from other fitting schemes and t dependences. Red crosses represent original potential data.

Fig. 6.4 shows the fitted potential plus the centrifugal term for $N\pi$ (Left) and $\Xi\bar{K}$ (Right). Both have a large attractive pocket with a depth of about 3 GeV at $r \approx 0.2$ fm, a small barrier with a height of about a hundred MeV at $r \approx 0.5$ fm, and a shallow pocket with a depth of about a hundred MeV at $r \approx 1.0$ fm.

6.3.3 Physical observables

We solve the Schrödinger equation in the radial direction Eq. (5.10) with $l = 1$ for the P-wave scattering, and then extract scattering phase shifts.

Fig. 6.5 presents the scattering phase shift in both channels as a function of energy measured from the 2-body threshold, $\Delta E = E - m_M - m_B$. Both results show typical attractive behaviors; suddenly rising around $\Delta E = 0$ and then slowly decreasing, which is consistent with the shape of the potentials. As we increase energy further, the scattering phase shift in each channel approach zero degree, suggesting an existence of one bound state according to the Levinson's theorem.

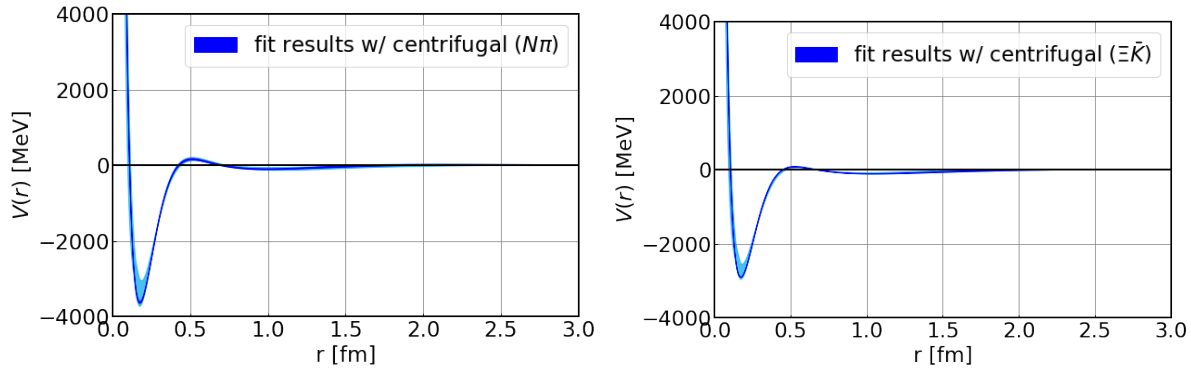

FIGURE 6.4: Fit results with a centrifugal term for $N\pi$ (Left) and $\Xi\bar{K}$ (Right). Dark and light blue bands represent statistical errors and statistical and systematic errors added in quadrature, respectively.

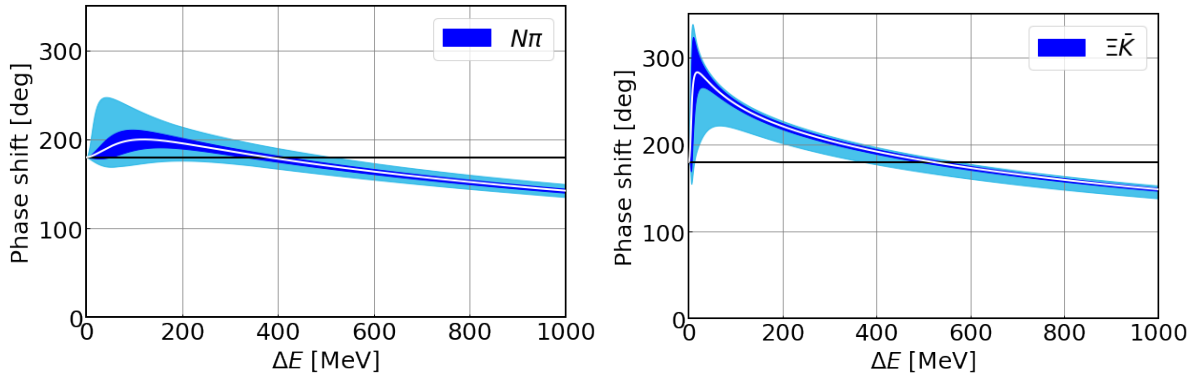

FIGURE 6.5: Scattering phase shifts for $N\pi$ (Left) and $\Xi\bar{K}$ (Right). Dark and light blue bands represent statistical errors and statistical and systematic errors added in quadrature, respectively.

We calculate a binding energy in each channel by solving the Schrödinger equation via the Gaussian Expansion Method (GEM) [71] and converting the negative eigenvalue k^2 to the binding energy through

$$E_{\text{bind}} = \sqrt{-\kappa^2 + m_M^2} + \sqrt{-\kappa^2 + m_B^2} - m_M - m_B, \tag{6.14}$$

where $\kappa^2 = -k^2$ is the absolute value of k^2. The results are

$$E_{\text{bind}}^{N\pi} = 115.6(17.2)\left(^{+54.0}_{-69.3}\right) \text{ MeV}, \tag{6.15}$$
$$E_{\text{bind}}^{\Xi\bar{K}} = 256.6(5.5)\left(^{+88.2}_{-82.2}\right) \text{ MeV}, \tag{6.16}$$

where the first and second errors show statistical and systematic errors, respectively. The results are also shown in Fig. 6.6 (vertical axis). The binding energies in both channels are consistent with the estimate using the decuplet baryon masses measured from 2-point functions;

$$\begin{aligned} m_N + m_\pi - m_\Delta &= 105.5(5.2) \text{ MeV}, \\ m_\Xi + m_{\bar{K}} - m_\Omega &= 293.5(2.8) \text{ MeV}, \end{aligned} \tag{6.17}$$

within large systematic errors.

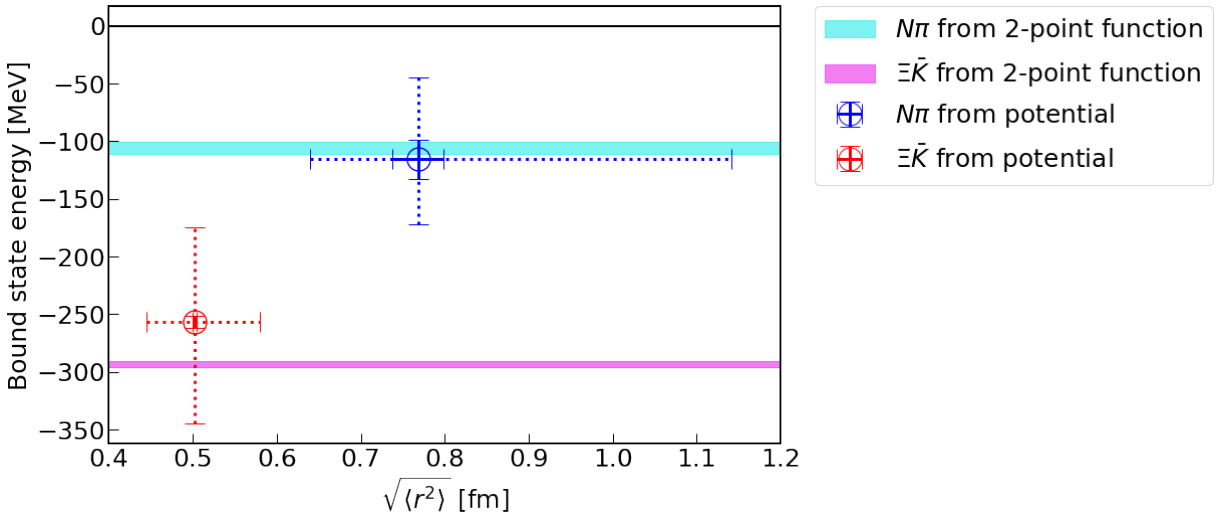

FIGURE 6.6: A binding energy (vertical axis) and a root-mean-square distance (horizontal axis) for $N\pi$ (blue) and $\Xi\bar{K}$ (red). Solid and dotted error bars show statistical errors and statistical and systematic errors added in quadrature, respectively. Cyan and magenta bands show binding energies estimated from Δ and Ω 2-point functions, respectively. Note that there is no constraint for root-mean-square distances from 2-point functions.

The binding energy in the $\Xi\bar{K}$ system is larger than that in the $N\pi$ system by more than a hundred MeV. Combined with the previous observation that the $\Xi\bar{K}$ potential has weaker attraction than the $N\pi$, it is indicated that a reason for a larger binding energy in the $\Xi\bar{K}$ than in the $N\pi$ is not the difference of the two interactions.

We also calculate root-mean-square (RMS) distances of wave functions obtained via the GEM for bound states, which gives

$$\sqrt{\langle r^2\rangle_{N\pi}} = 0.77(0.03)\left(^{+0.37}_{-0.12}\right) \text{ fm}, \tag{6.18}$$

$$\sqrt{\langle r^2\rangle_{\Xi\bar{K}}} = 0.50(0.00)\left(^{+0.08}_{-0.06}\right) \text{ fm}, \tag{6.19}$$

where the first and second errors represent statistical and systematic errors, respectively. The results of RMS distances are also depicted in Fig. 6.6 (horizontal axis). Sizes of both bound states estimated by RMS distances are quite small and similar to ranges of attractive pockets in their potentials. These suggest that Δ and Ω can be regarded qualitatively as composite states of 3 quarks rather than meson-baryon molecule states at this quark mass(?).

More quantitatively, however, their RMS distances are larger than a range of the attractive pocket $r \approx 0.2$ fm in both $N\pi$ and $\Xi\bar{K}$ potentials with the centrifugal term, as seen in Fig. 6.4. This can be explained by shapes of wave functions, shown in Fig. 6.7, which exhibits peak structures at $r \approx 0.2$ fm but has long-range tails.

The RMS distance for $\Xi\bar{K}$ system is smaller than that for $N\pi$. This indicates that the main reason for the larger binding energy in $\Xi\bar{K}$ system is the smaller size of its wave function, as seen explicitly in Fig. 6.7, which leads to a larger contribution from a combination $\int d^3r\, \psi^*(\mathbf{r})V(r)\psi(\mathbf{r})$ to the binding energy. Since such wave function is likely to be formed for systems with a large reduced mass, the difference between the size of the two wave functions mainly comes from the difference between the two reduced masses. Therefore, if we assume that the interaction potentials are not so sensitive to the quark masses, we could predict the behaviors of Δ and Ω in Nature as follows. When we decrease quark masses to the values in Nature, the

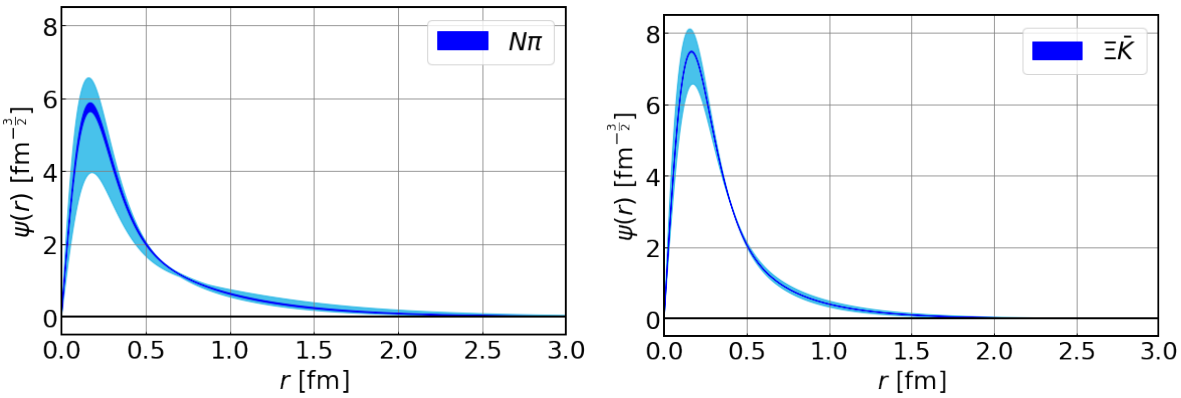

FIGURE 6.7: Normalized wave functions for bound states in $N\pi$ (Left) and $\Xi\bar{K}$ (Right) systems. Dark and light blue bands represent statistical errors and statistical and systematic errors added in quadrature, respectively.

bound state would disappear and Δ would become a resonance in the $N\pi$ system because of its small reduced mass and the broad structure of Δ, while the bound state Ω would remain in the $\Xi\bar{K}$ system due to its large reduced mass leading to the compact size of Ω.

Results of both binding energies and RMS distances suffer from quite large systematic uncertainties compared to statistical errors. Such large uncertainties come dominantly from lattice artifacts at short distances. Fig. 6.8 and Fig. 6.9 show binding energy and RMS distance, respectively, estimated in each fitting scheme and timeslice t. A dependence on an order of the approximation for the Laplacian (2nd/4th for Fit 1/2, 3/4, 5/6, 7/8), or a dependence on treatment of data at $r = a$ (without/with for Fit 1/3, 2/4, 5/7, 6/8), are much larger than dependences on t or fit without/with mirrors (Fit 1/5, 2/6, 3/7, 4/8). Comparing, for example, the magenta and cyan points in Fig. 6.10, the precision of the Laplacian term affects potential data at short distances. Moreover, as we can see, for example, the red and orange lines in the figure, fit results without and with data at $r = a$ (without/with for Fit 1/3, 2/4) deviate from each other around $r = a \approx 0.09$ fm. Consequently, large dependences of binding energies and RMS distances on the accuracy of the Laplacian and the treatment of the data at $r = a$ are caused dominantly by lattice artifacts at short distances, which is associated with rapid changes of potentials around the origin. On the contrary, the results are not so sensitive to finite-volume effects as seen from comparisons between Fit i and Fit $i + 4$ schemes in Fig. 6.8 and Fig. 6.9.

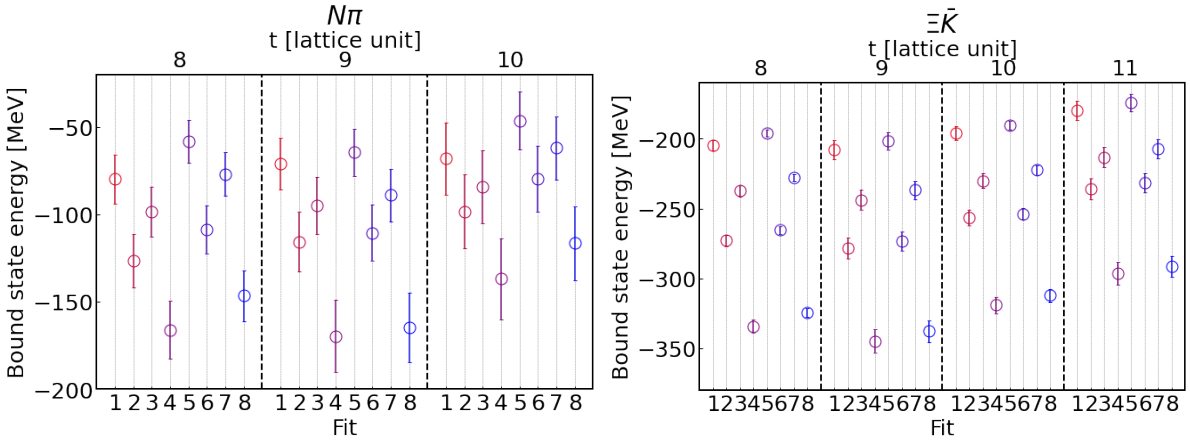

FIGURE 6.8: Bound state energies for different fitting schemes and t for $N\pi$ (Left) and $\Xi\bar{K}$ (Right). Plots are separated for different t by dashed lines.

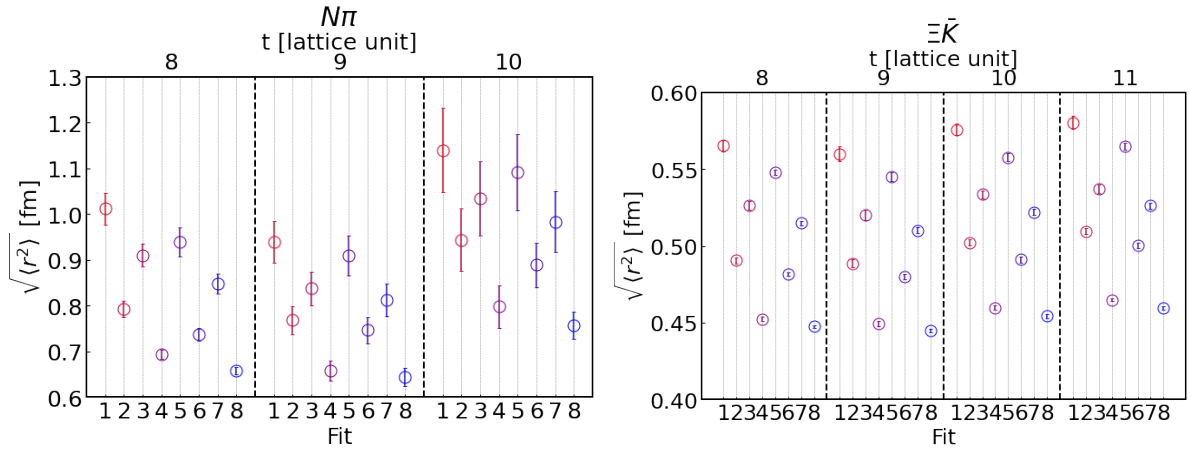

FIGURE 6.9: Root-mean-square distances for different fitting schemes and t for $N\pi$ (Left) and $\Xi\bar{K}$ (Right). Plots are separated for different t by dashed lines.

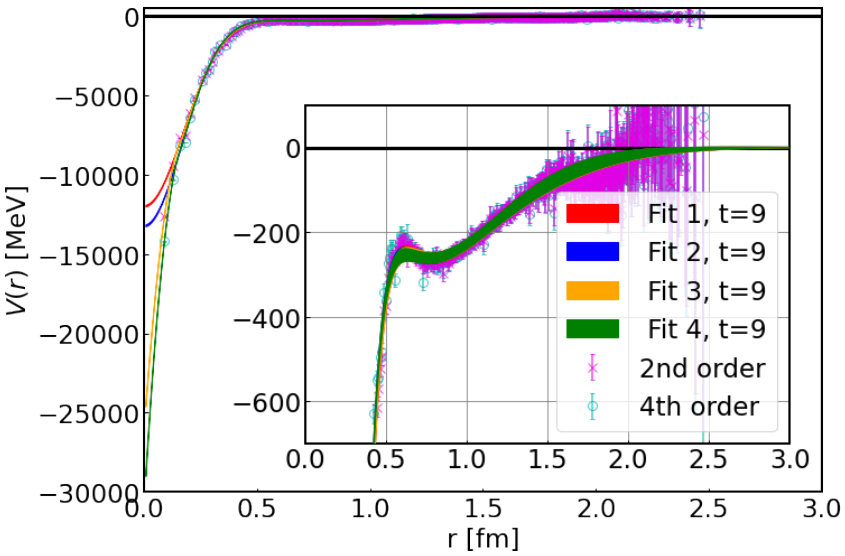

FIGURE 6.10: Original potential data with 2nd (magenta) and 4th (cyan) order accuracies of the Laplacian term for $N\pi$ at $t = 9$, and fit results for Fit 1-4 at the same t.

Chapter 7

Studies on $\Lambda(1405)$ in SU(3) limit in the HAL QCD method

In this chapter, we attempt to study $\Lambda(1405)$, which is a resonance with the quantum number $S = -1$, $I = 0$, and $J^P = 1/2^-$ lying around 1405 MeV, below $N\bar{K}$ threshold and above $\Sigma\pi$ threshold. This hadron is one of the exotic hadrons, that is, $\Lambda(1405)$ cannot be described by a 3-quark state in the quark model. There have been numerous theoretical and experimental studies, suggesting that it is a 5-quark state or a molecule state of $N\bar{K}$ system. There are several previous studies by the chiral unitary model [72], which predict that $\Lambda(1405)$ is represented by not a pole but two poles of the S-matrix in the complex plane.

As a first step of the calculation, we study $\Lambda(1405)$ in the flavor SU(3) limit $m_u = m_d = m_s$, where only the single channel analysis is necessary. The previous work by the chiral unitary model [73] suggests that the two poles associated with $\Lambda(1405)$ correspond to the two at the real axis in the SU(3) limit: one is in the singlet representation and the other is in the octet representation. This indicates that the meson-baryon system in each singlet and octet representation has a bound state. In this study, by analyzing the interaction potential in the HAL QCD method and solving the Schrödinger equation with the potentials, we see whether this scenario is true in the QCD theory.

7.1 Meson-baryon operators and 3-point correlation functions in SU(3) limit

In the SU(3) limit, the lightest meson and baryon belong to the octet representation. Thus the meson-baryon states are characterized by their tensor product, which gives the direct-sum decomposition as

$$8 \otimes 8 = 27 \oplus 10 \oplus 10^* \oplus 8_1 \oplus 8_2 \oplus 1. \tag{7.1}$$

Here, we define that 8_1 and 8_2 are symmetric and anti-symmetric under exchanging the two identical octet representations in the left-hand side of the equation, respectively. The chiral unitary model suggests that the meson-baryon scatterings in the two octet representation 8_1 and 8_2 and one singlet representation 1 have a pole of the S-matrix corresponding to $\Lambda(1405)$ in Nature. Therefore, we use the HAL QCD method to analyze the meson-baryon scatterings belonging to these three representations[1].

[1]The meson-baryon systems for 8_1 and 8_2 representations cannot be distinguished and could mix with each other. We ignore their mixing in this study and such an effect on the observables should be examined in the future.

Each octet meson operator is given by

$$\begin{aligned}
\begin{pmatrix}\pi^+\\ \pi^0\\ \pi^-\end{pmatrix} &= \begin{pmatrix}\bar{d}\gamma_5 u\\ \frac{1}{\sqrt{2}}(-\bar{u}\gamma_5 u+\bar{d}\gamma_5 d)\\ -\bar{u}\gamma_5 d\end{pmatrix}, \quad \begin{pmatrix}K^+\\ K^0\end{pmatrix} = \begin{pmatrix}\bar{s}\gamma_5 u\\ \bar{s}\gamma_5 d\end{pmatrix},\\
\begin{pmatrix}\bar{K}^0\\ K^-\end{pmatrix} &= \begin{pmatrix}\bar{d}\gamma_5 s\\ -\bar{u}\gamma_5 s\end{pmatrix}, \quad \eta^8 = -\frac{1}{\sqrt{6}}(\bar{u}\gamma_5 u+\bar{d}\gamma_5 d-2\bar{s}\gamma_5 s),
\end{aligned} \tag{7.2}$$

and each octet baryon operator is described as

$$\begin{aligned}
\begin{pmatrix}\Sigma^+_\alpha\\ \Sigma^0_\alpha\\ \Sigma^-_\alpha\end{pmatrix} &= \begin{pmatrix}\epsilon_{abc}(sC\gamma_5 u)u\\ \frac{1}{\sqrt{2}}\epsilon_{abc}[-(d_a^T C\gamma_5 s_b)u_{c,\alpha}+(s_a^T C\gamma_5 u_b)d_{c,\alpha}]\\ -\epsilon_{abc}(d_a^T C\gamma_5 s_b)d_{c,\alpha}\end{pmatrix},\\
\begin{pmatrix}p_\alpha\\ n_\alpha\end{pmatrix} &= \begin{pmatrix}\epsilon_{abc}(u_a^T C\gamma_5 d_b)u_{c,\alpha}\\ \epsilon_{abc}(u_a^T C\gamma_5 d_b)d_{c,\alpha}\end{pmatrix}, \quad \begin{pmatrix}\Xi^0_\alpha\\ \Xi^-_\alpha\end{pmatrix} = \begin{pmatrix}\epsilon_{abc}(s_a^T C\gamma_5 u_b)s_{c,\alpha}\\ -\epsilon_{abc}(d_a^T C\gamma_5 s_b)s_{c,\alpha}\end{pmatrix},\\
\Lambda^8_\alpha &= -\frac{1}{\sqrt{6}}\epsilon_{abc}[(d_a^T C\gamma_5 s_b)u_{c,\alpha}+(s_a^T C\gamma_5 u_b)d_{c,\alpha}-2(u_a^T C\gamma_5 d_b)s_{c,\alpha}].
\end{aligned} \tag{7.3}$$

with upper two spinor index α. Here we abbreviate the spacetime coordinates. There are eight bases in the 8_1 and 8_2 representations, and we consider the basis which has the isospin $I=0$ and strangeness $S=-1$. According to Ref. [74], the meson-baryon operators in SU(3) limit can be rewritten by the linear combination of the product of the meson operator Eq. (7.2) and the baryon operator Eq. (7.3). The meson-baryon operators in the 8_1, 8_2, and 1 representations are represented as

$$\begin{aligned}
(MB_\alpha)^{S=-1,I=0}_{8_1} &= \frac{\sqrt{10}}{10}(K\Xi_\alpha)^{I=0}-\frac{\sqrt{10}}{10}(\bar{K}N_\alpha)^{I=0}-\frac{\sqrt{15}}{5}(\pi\Sigma_\alpha)^{I=0}-\frac{\sqrt{5}}{5}\eta^8\Lambda^8_\alpha\\
&= \frac{\sqrt{5}}{10}(K^+\Xi^-_\alpha-K^0\Xi^0_\alpha-\bar{K}^0 n_\alpha+K^- p_\alpha-2(\pi^-\Sigma^+_\alpha-\pi^0\Sigma^0_\alpha+\pi^+\Sigma^-_\alpha)-2\eta^8\Lambda^8_\alpha),\\
(MB_\alpha)^{S=-1,I=0}_{8_2} &= \frac{\sqrt{2}}{2}(K\Xi_\alpha)^{I=0}+\frac{\sqrt{2}}{2}(\bar{K}N_\alpha)^{I=0}\\
&= \frac{1}{2}(K^+\Xi^-_\alpha-K^0\Xi^0_\alpha+\bar{K}^0 n_\alpha-K^- p_\alpha),\\
(MB_\alpha)^{S=-1,I=0}_{1} &= \frac{1}{2}(K\Xi_\alpha)^{I=0}-\frac{1}{2}(\bar{K}N_\alpha)^{I=0}+\frac{\sqrt{6}}{4}(\pi\Sigma_\alpha)^{I=0}-\frac{\sqrt{2}}{4}\eta^8\Lambda^8_\alpha\\
&= \frac{\sqrt{2}}{4}(K^+\Xi^-_\alpha-K^0\Xi^0_\alpha-\bar{K}^0 n_\alpha+K^- p_\alpha+\pi^+\Sigma^-_\alpha-\pi^0\Sigma^0_\alpha+\pi^-\Sigma^+_\alpha-\eta^8\Lambda^8_\alpha).
\end{aligned} \tag{7.4}$$

In spite of that, the ChPT more or less guarantees this approximation in a low-energy region because the two systems in the model do not mix and have equal interactions up to the Born term in the chiral expansion [73].

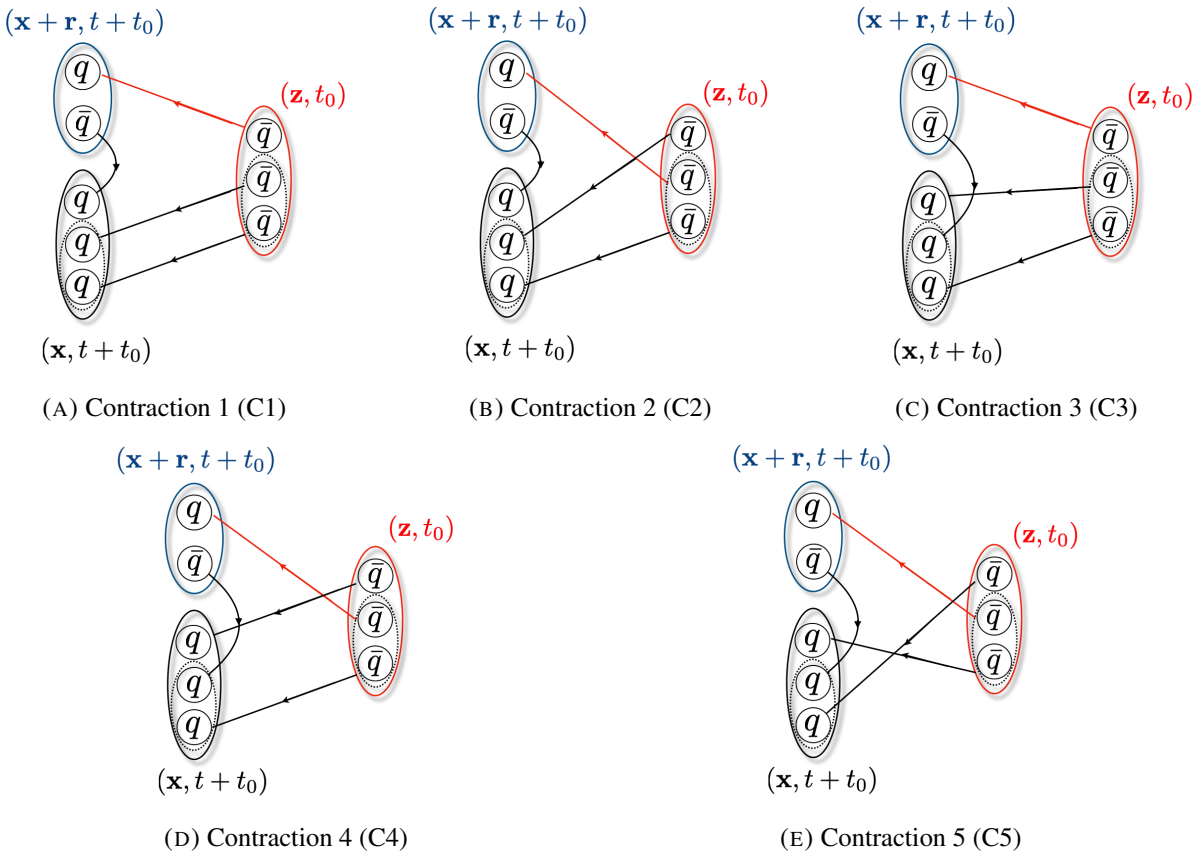

(A) Contraction 1 (C1) (B) Contraction 2 (C2) (C) Contraction 3 (C3)

(D) Contraction 4 (C4) (E) Contraction 5 (C5)

FIGURE 7.1: Quark contraction diagrams which appear in Eq. 7.5. Black dotted circles surrounding two quarks (or antiquarks) represent the diquark part $q^T C\gamma_5 q$ in the baryon operator. All-to-all and point-to-all propagators are used in red lines and black lines, respectively.

In this study, we calculate the following 3-point correlation functions in the 8_1, 8_2, and 1 representations:

$$\begin{aligned} F^{8_1}_{\alpha}(\mathbf{r}, t) &= \langle (M(\mathbf{r}+\mathbf{x}, t+t_0) B_\alpha(\mathbf{x}, t+t_0))^{S=-1, I=0}_{8_1} \sum_{\mathbf{z}} \Lambda^{8\dagger}_{\bar{\alpha}}(\mathbf{z}, t_0) \rangle, \\ F^{8_2}_{\alpha}(\mathbf{r}, t) &= \langle (M(\mathbf{r}+\mathbf{x}, t+t_0) B_\alpha(\mathbf{x}, t+t_0))^{S=-1, I=0}_{8_2} \sum_{\mathbf{z}} \Lambda^{8\dagger}_{\bar{\alpha}}(\mathbf{z}, t_0) \rangle, \\ F^{1}_{\alpha}(\mathbf{r}, t) &= \langle (M(\mathbf{r}+\mathbf{x}, t+t_0) B_\alpha(\mathbf{x}, t+t_0))^{S=-1, I=0}_{1} \sum_{\mathbf{z}} \Lambda^{1\dagger}_{\bar{\alpha}}(\mathbf{z}, t_0) \rangle, \end{aligned} \tag{7.5}$$

where $\Lambda^1_{\bar{\alpha}}$ is the singlet baryon operator defined as

$$\Lambda^1_{\bar{\alpha}} = \frac{1}{\sqrt{3}} \epsilon_{abc} [(d^T_a C\gamma_5 s_b) u_{c,\bar{\alpha}} + (s^T_a C\gamma_5 u_b) d_{c,\bar{\alpha}} + (u^T_a C\gamma_5 d_b) s_{c,\bar{\alpha}}], \tag{7.6}$$

where $\bar{\alpha}$ denotes the lower two spinor components with the same spin as α, which represents a singlet baryon with negative parity with spin α.

The quark contraction diagrams for the general meson-baryon 3-point correlation functions with the octet baryon source are classified into the five types shown in Fig. 7.1. We label each contraction diagram as "Cn" ($n = 1, 2, 3, 4, 5$) as shown in the caption of the figure. For the 8_1, 8_2, and 1 representations, the explicit forms of the 3-point correlation functions in terms of the

contractions in Fig. 7.1 read

$$\begin{aligned} F_\alpha^{8_1}(\mathbf{r},t) &= -\sqrt{10}[(\mathrm{C1})+(\mathrm{C2})+(\mathrm{C3})-(\mathrm{C4})-2(\mathrm{C5})], \\ F_\alpha^{8_2}(\mathbf{r},t) &= -\frac{\sqrt{6}}{2}[(\mathrm{C1})+(\mathrm{C2})+(\mathrm{C3})+(\mathrm{C4})], \\ F_\alpha^{1}(\mathbf{r},t) &= -\frac{4}{\sqrt{3}}[(\mathrm{C1})-2(\mathrm{C2})+(\mathrm{C3})-(\mathrm{C4})+(\mathrm{C5})]. \end{aligned} \tag{7.7}$$

As is the case of the analysis of $N\pi$ and $\Xi\bar{K}$ scatterings, the coordinate $\mathbf{x}$ at the sink is fixed and $\mathbf{z}$ is summed over in order for the operator $\Lambda_{\bar{\alpha}}^{R\dagger}$ $(R = 8, 1)$ to have zero momentum. Then the propagators shown by red lines in Fig. 7.1 are all-to-all propagators, while the propagators represented by black lines are point-to-all.

7.2 Simulation details

In this calculation, we use gauge configurations in flavor-SU(3) limit generated by Inoue (for HAL QCD Collaboration) with the improved Iwasaki gauge action and the $\mathcal{O}(a)$-improved Wilson quark action at $\beta = 1.83$ on 32^4 lattice volume [75], where the lattice spacing $a = 0.121(2)$ fm. The hopping parameters are $\kappa_u = \kappa_d = \kappa_s = 0.13800$. We impose the periodic boundary condition in all spacetime directions. We used 130 configurations with 32 sources at different time slices on each configuration, and average forward and backward propagations to increase statistics. Statistical errors are estimated by the jackknife method with a binsize of 13 configurations.

We employ a quark source with the smearing function Eq. (2.71) with $(A, B) = (1.2, 0.3)$ at the source, and with $(A, B) = (1.0, 1/0.7)$ at the sink to reduce the singular behaviors of potentials at short distances.

For the approximate calculation of all-to-all propagators, we use the conventional stochastic technique combined with the dilutions for color/spinor/time components and the s4 dilution [61] for the position $\mathbf{z}$ defined as

$$\begin{cases} \eta^{(0)}(\mathbf{x}) \neq 0 \iff (x,y,z) = (\text{even},\text{even},\text{even}) \text{ or } (\text{odd},\text{odd},\text{odd}) \\ \eta^{(1)}(\mathbf{x}) \neq 0 \iff (x,y,z) = (\text{odd},\text{even},\text{even}) \text{ or } (\text{even},\text{odd},\text{odd}) \\ \eta^{(2)}(\mathbf{x}) \neq 0 \iff (x,y,z) = (\text{even},\text{odd},\text{even}) \text{ or } (\text{odd},\text{even},\text{odd}) \\ \eta^{(3)}(\mathbf{x}) \neq 0 \iff (x,y,z) = (\text{even},\text{even},\text{odd}) \text{ or } (\text{odd},\text{odd},\text{even}) \end{cases} . \tag{7.8}$$

For the fixed spatial coordinate $\mathbf{x}$ at the sink, we employ the CAA combined with the truncated solver method using the translational invariance of $\mathbf{x}$: $\Delta\mathbf{x} = (0,0,0), (0,0,8), \cdots, (24,24,24)$. The number of elements $N_G = 64$ in this case. For the specific value of $\mathbf{x}$, we choose it randomly for each gauge configuration, as is the case of the S-wave NK scatterings and the $N\pi$ and $\Xi\bar{K}$ scatterings.

We project each spin component of the 3-point correlation functions onto the A_1^+ representation, corresponding to the S-wave wave functions. Also, we take an average over the spin components, which gives the signal only in the real part thanks to the charge conjugation symmetry. We thus ignore its imaginary part.

We calculate the octet meson 2-point correlation functions using all-to-all propagators, where the one-end trick is employed, and the octet and singlet baryon 2-point correlation functions

	Repr.	Octet	
	mass (MeV)	671.2(1.5)	
	fit range	[8,15]	
Repr.	Octet	Octet	Singlet
Parity	+	−	−
mass (MeV)	1488.8(3.9)	2013.2(11.2)	1923.4(9.1)
fit range	[8,13]	[6,11]	[5,11]

TABLE 7.1: Meson (Upper panel) and baryon masses (Lower panel) estimated from the 2-point correlation functions. The third row in the upper panel and the fourth row in the lower panel show temporal fitting ranges in lattice unit.

using point-to-all propagators. We also employ the smearing to quarks at the source and the sink in the 2-point functions with the same parameters as for the 3-point correlation functions. Table. 7.1 lists the results of the hadron masses, which satisfy $m_{8B}^{-} - m_{8B}^{+} - m_M < 0$ and $m_{1B}^{-} - m_{8B}^{+} - m_M < 0$, where m_M is the octet meson mass and m_{RB}^{P} is the mass of baryon with the parity P and the representation R. The two inequalities indicate that there is at least one bound state of each meson-baryon system in this setup.

For the truncation of the summation over k in Eq. (3.64), we set $k \leq 2$.

7.3 Numerical results

7.3.1 3-point functions, LO potentials, and their fitting results

Fig. 7.2 shows the 3-point correlation function in each representation. All three correlation functions have a behavior of changing rapidly and crossing zero in short distances ($r < 0.5$ fm) while smoothly changing in the middle and long distances ($r > 0.5$ fm). Fig. 7.3 depicts the following quantity formed by the 3-point correlation functions:

$$W_{\text{eff}}(t) = -\ln \frac{\sum_{\mathbf{r}} F(\mathbf{r}, t+a)}{\sum_{\mathbf{r}} F(\mathbf{r}, t)}, \tag{7.9}$$

called effective energy. From Eq. (3.55), $W_{\text{eff}}(t)$ at large t becomes the lowest energy W_0 and gets independent of t. From the figure, $W_{\text{eff}}(t)$ in each representation seems to have a plateau near the value of the mass in the corresponding representation with negative parity evaluated from the 2-point correlation function shown in Table 7.1, which implies that the energy of the ground state takes the value around that shown in the table.

We show in Fig. 7.4 the LO potentials at $t = 8$. We find a singular behavior in every potential; it has a quite large value and seems to be non-continuous at a finite radius r. As we see that the zero point of the 3-point correlation function represented by a star plot matches the singular point of the potential, the singular behavior comes from the zero point of the correlation function in the denominator in Eq. (3.64).

Assuming that there is a singular point of the potential at the zero point of the corresponding 3-point correlation functions, we perform the uncorrelated fitting as follows. First, we use the data $(r - r_s)V^{LO}(r)$ in the fitting, where $V^{LO}(r)$ is the original potential data and r_s is the zero point of the 3-point correlation functions. The fit function is the four Gaussians Eq. (5.9). As seen in Fig. 7.5, it seems that the data $(r - r_s)V^{LO}(r)$ is continuous and the fitting works well.

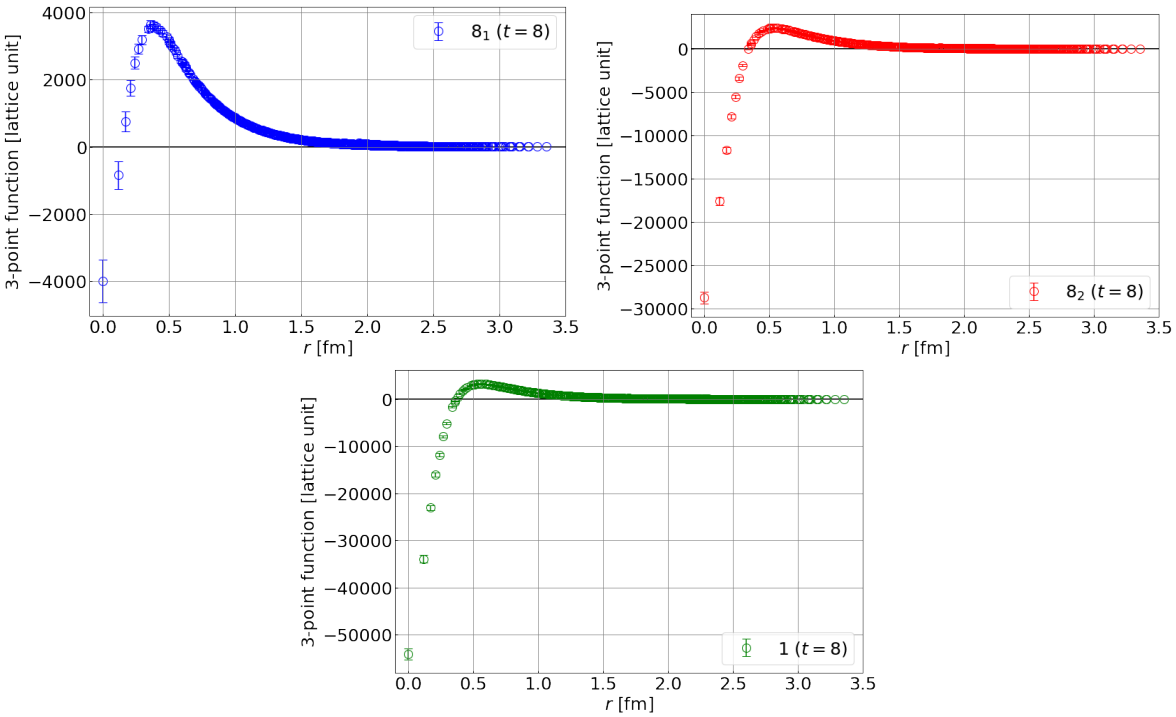

FIGURE 7.2: Three point correlation functions in 8_1 (Upper left), 8_2 (Upper right), and 1 representation (Lower panel) at $t = 8$.

7.3.2 Bound states

We solve the Schrödinger equation in the radial direction Eq. (5.10) with $l = 0$ for the S-wave scatterings and calculate its binding energy in each representation by GEM. For the potential function, since using the fit funciton $V^{4G}(r)$ divided by $r - r_s$ directly fails to solve the Schrödinger equation due to a large value around $r = r_s$, we utilize the following functions:

$$V_\delta(r) = \frac{V^{4G}(r)}{r - (r_s + \delta)}\theta(r_s - r) + \frac{V^{4G}(r)}{r - (r_s - \delta)}\theta(r - r_s), \tag{7.10}$$

where δ is a positive small value, which plays a role of a "cutoff" of the singularity. In our actual calculation, we set $\delta = 0.001a$ with the lattice spacing a.

From the results, we find that there are two bound states in each channel. The value of κ^2 in each state is listed in Table. 7.2. The κ^2 for the ground state is too large, much larger than m_M^2, to be converted to the binding energy. This observation together with the time dependence of effective energy in Fig. 7.3 indicates that the state is not the physical one and may come from the singular behavior of the potential due to the zero point of the 3-point correlation function. On the other hand, the first excited state has κ^2 smaller than m_M^2. The corresponding binding energies are

$$E^{8_1}_{\text{bind}} = 185 \pm 17\ \text{MeV}, \quad E^{8_2}_{\text{bind}} = 167 \pm 11\ \text{MeV}, \quad E^{1}_{\text{bind}} = 206 \pm 56\ \text{MeV}, \tag{7.11}$$

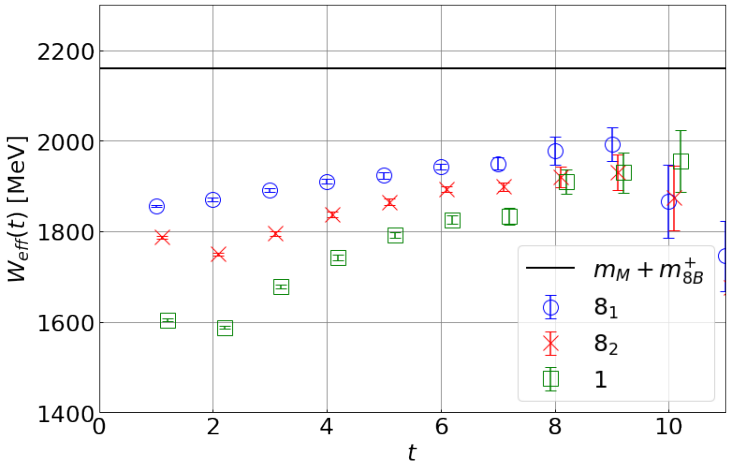

FIGURE 7.3: Effective energies Eq. (7.9) in each representation.

	8_1	8_2	1
ground state	24.14(2.91)	3.65(0.09)	3.59(0.81)
1st excited state	0.35(0.03)	0.32(0.02)	0.39(0.09)

TABLE 7.2: The results of κ^2/m_M^2 for the ground and first excited states.

which are similar to the results from the 2-point correlation functions:

$$\begin{aligned} m_{8B}^+ + m_M - m_{8B}^- &= 146.0 \pm 13.1 \text{ MeV}, \\ m_{8B}^+ + m_M - m_{1B}^- &= 236.7 \pm 8.2 \text{ MeV}, \end{aligned} \tag{7.12}$$

This suggests that the first excited state is the actual physical bound state.

One possible reason for the existence of the unphysical states, that is, the zero point in the 3-point correlation function, is as follows. The operator product expansion (OPE) [76–79] predicts the singular behavior of the NBS wave function with quark pair creation and annihilation at $r \to 0$ as

$$\Psi(\mathbf{r}) \propto \frac{1}{r^3}(\log r)^\alpha \tag{7.13}$$

with a real value α, which is the contribution from the dynamics in a very high-energy region. The correlation function crossing zero may come from the short-distance behavior of the NBS wave function represented by Eq. (7.13) with a negative sign, which comes from the high-energy dynamics, together with the behavior in a long distance, which originates from the low-energy dynamics, with a positive sign. Furthermore, the behavior Eq. (7.13) gives the form of the LO potential $V^{LO}(r) \propto \frac{1}{r^2}$ in a short distance, which is the behavior that we cannot handle on in the quantum scattering theory. One of the solutions to these problems is that we use the source operator which does not have either the form Eq. (7.13) or the behavior of crossing zero. In the actual calculation, this corresponds to preparing correlation functions with different source operators and the same sink operator and then taking linear combinations to cancel out the problematic behaviors which each correlation function has. In order to do so, we should additionally calculate the 4-point correlation function: the correlation function with the meson-baryon source operator. This is left for our future studies.

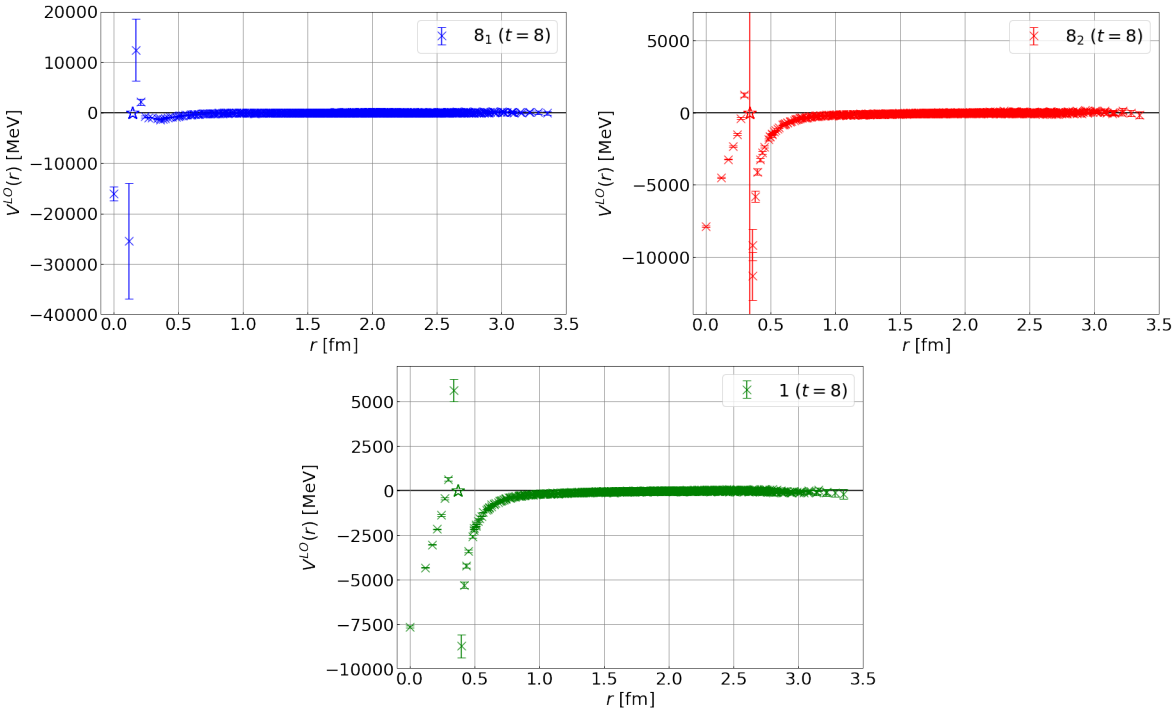

FIGURE 7.4: LO potentials in 8_1 (Upper left), 8_2 (Upper right), and 1 representation (Lower panel) at $t = 8$. The zero points of the corresponding 3-point correlation functions are plotted as star plots in the figures.

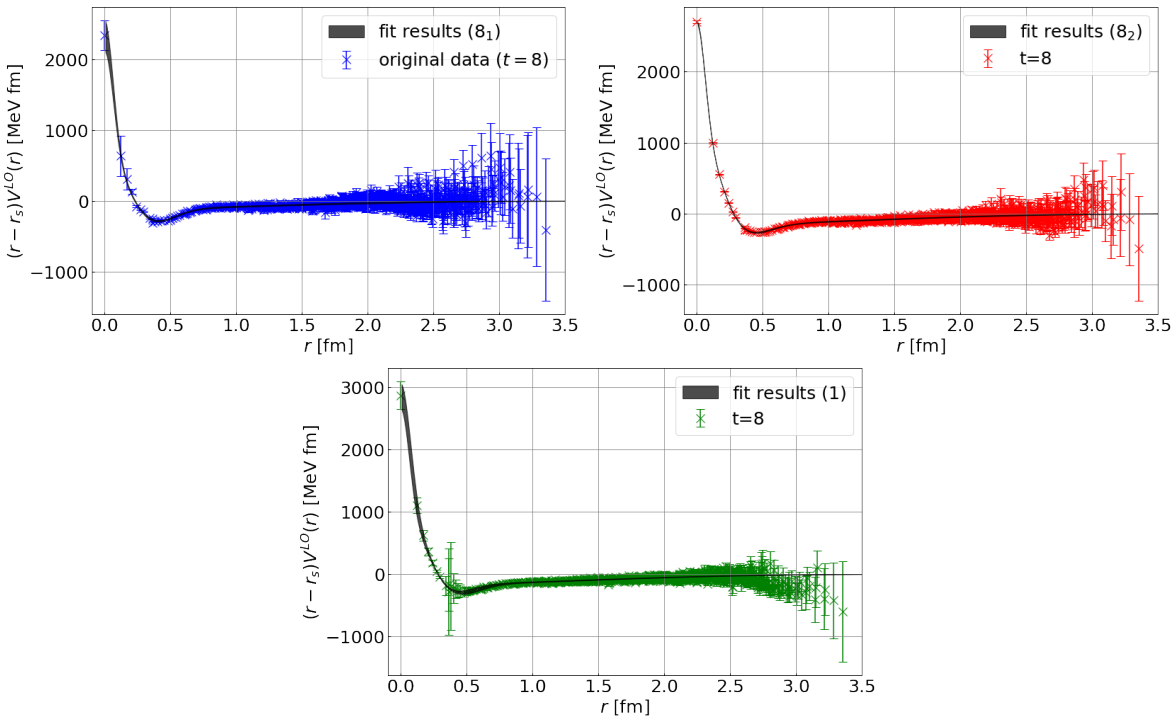

FIGURE 7.5: Fit results of $(r - r_s)V^{LO}(r)$ in 8_1 (Upper left), 8_2 (Upper right), and 1 representation (Lower panel) at $t = 8$ represented by black bands. The plots in each panel show the original data.

Chapter 8

Summary and Discussions

In this thesis, towards the exploration of baryon resonances and pentaquarks from the first-principle calculation of QCD, we have analyzed meson-baryon scatterings in lattice QCD with all-to-all propagators. We employ the calculation technique of all-to-all propagators which is similar to that used in the previous analysis of meson-meson systems. We calculate the leading-order (LO) potential using the time-dependent HAL QCD method and then extracted the scattering phase shifts by solving the Schrödinger equations with the fitted potentials.

8.1 S-wave NK scatterings

We have analyzed S-wave nucleon-kaon (NK) scatterings at $m_\pi \approx 570$ MeV. We have evaluated the 4-point correlation functions with the kaon operator at sources which has zero momentum, where we have employed the one-end trick to calculate all-to-all propagators. In addition, we have used the covariant-approximation averaging (CAA) combined with the truncated solver method, which is equivalent to the all-mode averaging (AMA) without low modes.

Both the $I = 1$ and $I = 0$ potentials have repulsive cores while the $I = 1$ potential is more repulsive than the $I = 0$. The scattering phase shifts for both isospins qualitatively reproduce the energy dependences of the experimental data and are consistent with the previous theoretical results such as the lattice calculations. These results suggest that the all-to-all propagator technique in this study works well to investigate meson-baryon scatterings in the HAL QCD method. Furthermore, we have found that no resonances or bound states appear in the behaviors of the phase shifts, suggesting that $\Theta^+(1540)$ does not exist in the $J^P = 1/2^-$ with $I = 0, 1$ channels at the quark mass in this setup.

The experiment and the previous theoretical studies give completely repulsive behavior of the phase shift for the $I = 0$ NK systems, while our analysis with heavier quark masses produces the attractive pocket in the $I = 0$ potential. This suggests that the attractive pocket disappears at the lighter quark mass. The study from the HAL QCD approach at such quark mass is of interest, which is left to our future works.

8.2 P-wave $I = 3/2$ $N\pi$ and $I = 0$ $\Xi\bar{K}$ interactions

We have studied P-wave $I = 3/2$ $N\pi$ and $I = 0$ $\Xi\bar{K}$ scatterings. We have calculated the 3-point correlation functions, which have 3-quark-type source operators with zero momentum. As a calculation of the all-to-all propagator, we have employed the conventional stochastic technique and the CAA combined with the truncated solver method. We have used gauge configurations at $m_\pi \approx 410$ MeV, where both Δ and Ω baryons exist as bound states in $N\pi$ and $\Xi\bar{K}$ systems, respectively.

From the results of the LO potential, the $\Xi\bar{K}$ system has a weaker attractive interaction than the $N\pi$. On the other hand, the binding energy of the $\Xi\bar{K}$ is larger than that of the $N\pi$. This indicates that the difference between the two interactions does not contribute to the larger binding energy of the $\Xi\bar{K}$, in other words, the inequality $m_N + m_\pi - m_\Delta < m_\Xi + m_{\bar{K}} - m_\Omega$. On the other hand, an RMS distance of a bound state of $\Xi\bar{K}$ system is smaller than that of $N\pi$, which suggests that the inequality is mainly explained by a smaller spatial size of the wave function of the $\Xi\bar{K}$ bound state due to its larger reduced mass. This inequality probably holds even at the physical pion mass, so that Δ exists as a resonance while Ω is a stable particle.

RMS distances of bound states in both systems are very small, which indicates that in this setup, Δ and Ω are tightly bound states and can be regarded qualitatively as 3-quark states.

Binding energies in both systems are consistent with those extracted from 2-point functions of single Δ and Ω baryons, although systematic errors are rather large, mainly due to lattice artifacts at short distances. The RMS distances also have large systematic errors as well. These observations together with the small RMS distances indicate that a short distant part of the potentials is relevant for a compact state such as Δ and Ω in this study while it suffers severely from lattice artifacts. Therefore, further improvement is desirable for the HAL QCD method to handle such states. On the other hand, direct extraction of a single hadron mass from a 2-point correlation function of a single hadron operator is rather insensitive to such problems. However, in a setup where Δ appears as a resonance, the HAL QCD method is expected to become efficient.

In this work, we have performed the LO analysis in the derivative expansion of non-local potentials. Our results of the binding energies consistent with those from 2-point correlation functions imply that the LO analysis is sufficient in the present study. However, when the systematic uncertainties from lattice discretization are improved, the NLO analysis might be required as well, since the bound states lie much below the threshold in this lattice setup. The NLO analysis may be also necessary to study the Δ as a resonance since a resonance peak appears much higher energy than the threshold. The study in this direction is presented in Ref. [22].

This work together with the study of the S-wave NK scatterings is the first step toward the studies on actual baryon resonances in the HAL QCD method. Such studies, where we use lighter quark masses, require additional challenges due to larger statistical fluctuations caused by lighter quarks as well as the necessity of the NLO analysis explained above.

8.3 Studies on $\Lambda(1405)$ in SU(3) limit

We have shown our preliminary analysis of the S-wave meson-baryon scatterings in the two octet representations and one singlet representation in the flavor SU(3) limit, which are expected to have signals associated with $\Lambda(1405)$ according to the previous studies using the chiral unitary model. As well as the analysis of the $N\pi$ and $\Xi\bar{K}$ scatterings, we have calculated the 3-point functions with 3-quark type source operators with zero momentum and employed the conventional stochastic calculation and the CAA technique. We have used the gauge configuration at the octet meson mass $m_M \approx 670$ MeV. The hadron masses calculated from the 2-point correlation functions indicate that there is at least one bound state of each meson-baryon system.

The 3-point correlation function in every representation crosses zero in a short distance, which causes the singular behavior of the LO potential. In the results of the solutions of the Schrödinger equation, there are two bound states in each channel: one is the ground state which has too large κ^2 to be converted to the binding energy, which seems to be unphysical, and the

other is the first-excited state which has the same order of the binding energy as that estimated from the 2-point correlation function, which seems to be physical and the true ground state.

The existence of such a ground state may come from the singular behavior of the potential, that is, the 3-point correlation function crossing zero value. One possible reason is that the NBS wave function has the $1/r^3(\log r)^\alpha$ behavior in a very short distance, which is contributed by the high-energy dynamics, and analytic behavior in a middle and long distance, which is determined by the low-energy dynamics, with opposite signs to each other. To solve this problem, we have to use the source operator to suppress the $1/r^3(\log r)^\alpha$ behavior of the 3-point correlation function so that it has no zero points. In our actual calculation, this solution corresponds to calculating the additional 4-point correlation function with the same sink operator and taking the linear combination of the two correlation functions so that does not cross zero, which should be done in the future.

Acknowledgements

First, I would like to thank my supervisor, Prof. Sinya Aoki, for his tremendous guidance and support of my research activities. I am grateful to my research collaborators, Y. Akahoshi, T. Doi, K. Sasaki, E. Itou, K. Iida, and D. Suenaga, for fruitful discussions and advice. I also gratefully acknowledge helpful discussions with all members of the HAL QCD Collaboration and of the Kochi collaboration for lattice approach to superfluidity in dense 2-color QCD (KATSUO). I wish to thank all my past and present colleagues at the Yukawa Institute for Theoretical Physics and at the Department of Physics in Kyoto University for countless discussions, advice, and daily interactions. I would like to appreciate the economical support and warm encouragement of my parents, Koji Murakami and Michiyo Murakami.

We thank CP-PACS/JLQCD Collaborations [17], PACS-CS Collaboration [11], and ILDG/JLDG [80] for providing us with their gauge configurations. We use lattice QCD code of Bridge++ [81, 82] and its optimized version for the Oakforest-PACS by Dr. I. Kanamori [83]. Our numerical calculation has been performed on Cray XC40 at Yukawa Institute for Theoretical Physics (YITP) at Kyoto University, HOKUSAI BigWaterfall at RIKEN, and Oakforest-PACS in Joint Center for Advanced HighPerformance Computing (JCAHPC). I am supported in part by JST SPRING, Grant Number JPMJSP2110, and by the Japan Society for the Promotion of Science (JSPS). We appreciate Dr. J. Bulava for providing us with meson-baryon operators projected onto the IRs of the cubic group, which are very useful for checking our code in the work pf $N\pi$ and $\Xi\bar{K}$ scatterings.

Appendix A

Exact-relativistic time-dependent HAL QCD method with different masses

In this thesis, we obtain the LO potential from Eq. (3.62) with the truncation of the summation over k, in which the relativistic effect is expressed as the Taylor series in terms of time derivatives. The coefficient of the series $C^{(k)}_{m_1,m_2}$ has a nontrivial value for any k unless the two hadrons have equal mass and the coefficient only for $k = 1, 2$ has nonzero value [16].

In this appendix, we present an alternative formula in which relativistic effect can be exactly included by employing at most the 3rd time derivatives.

A.1 Naive formula

First, we show the direct application of Eq. (3.59) to the time-dependent HAL QCD method [84]. Multiplying Eq. (3.58) by $(\Delta W_n/M + 1)^2$, we have

$$\begin{aligned}&\left[\mathcal{P}(\Delta W_n) - \left(1 + \frac{\Delta W_n}{M}\right)^2 H_0\right] A_n \Psi^{W_n}_\alpha(\mathbf{r}) e^{-\Delta W_n t} \\ &= \int d^3r'\, U_{\alpha\beta}(\mathbf{r}, \mathbf{r}') \left(1 + \frac{\Delta W_n}{M}\right)^2 A_n \Psi^{W_n}_\beta(\mathbf{r}') e^{-\Delta W_n t}.\end{aligned} \tag{A.1}$$

We rewrite ΔW_n in terms of the time derivative as

$$\begin{aligned}&\left[\mathcal{P}\left(-\frac{\partial}{\partial t}\right) - \left(1 - \frac{1}{M}\frac{\partial}{\partial t}\right)^2 H_0\right] A_n \Psi^{W_n}_\alpha(\mathbf{r}) e^{-\Delta W_n t} \\ &= \int d^3r'\, U_{\alpha\beta}(\mathbf{r}, \mathbf{r}') \left(1 - \frac{1}{M}\frac{\partial}{\partial t}\right)^2 A_n \Psi^{W_n}_\beta(\mathbf{r}') e^{-\Delta W_n t}.\end{aligned} \tag{A.2}$$

Taking summation over n, we obtain the exact relativistic form of the relation as

$$\begin{aligned}&\left[\mathcal{P}\left(-\frac{\partial}{\partial t}\right) - \left(1 - \frac{1}{M}\frac{\partial}{\partial t}\right)^2 H_0\right] R_\alpha(\mathbf{r}, t) \\ &= \int d^3r'\, U_{\alpha\beta}(\mathbf{r}, \mathbf{r}') \left(1 - \frac{1}{M}\frac{\partial}{\partial t}\right)^2 R_\beta(\mathbf{r}', t),\end{aligned} \tag{A.3}$$

where

$$\mathcal{P}\left(-\frac{\partial}{\partial t}\right) = -\frac{\partial}{\partial t} + \frac{\mu+M}{2\mu M}\frac{\partial^2}{\partial t^2} - \frac{1}{2\mu M}\frac{\partial^3}{\partial t^3} + \frac{1}{8\mu M^2}\frac{\partial^4}{\partial t^4}. \tag{A.4}$$

The LO potential in this formulation reads

$$V^{\rm LO}(r) = \frac{\left(\mathcal{P}\left(-\frac{\partial}{\partial t}\right) - \left(1-\frac{1}{M}\frac{\partial}{\partial t}\right)^2 H_0\right) R_\alpha(\mathbf{r},t)}{\left(1-\frac{1}{M}\frac{\partial}{\partial t}\right)^2 R_\alpha(\mathbf{r},t)}, \tag{A.5}$$

which requires at most 4th-order time derivative terms.

A.2 Improved formula

Here we present a sophisticated technique that reduces the highest order in the time derivatives. We decompose $\mathcal{P}\left(-\frac{\partial}{\partial t}\right)$ into a term proportional to $(1-\frac{1}{M}\frac{\partial}{\partial t})^2$ and a remnant as

$$\begin{aligned} 2\mu\mathcal{P}\left(-\frac{\partial}{\partial t}\right) &= \left(1-\frac{1}{M}\frac{\partial}{\partial t}\right)^2 2\mu\left[-\frac{\partial}{\partial t} + b\frac{\partial^2}{\partial t^2}\right] \\ &+ 2\mu\left[\left(-b+\frac{1}{2\mu}-\frac{3}{2M}\right)\frac{\partial^2}{\partial t^2} - \frac{1}{M}\left(-2b+\frac{1}{2\mu}-\frac{1}{M}\right)\frac{\partial^3}{\partial t^3} + \frac{1}{M^2}\left(-b+\frac{1}{8\mu}\right)\frac{\partial^4}{\partial t^4}\right]. \end{aligned} \tag{A.6}$$

Here we introduce an arbitrary parameter b, such that terms proportional to b are summed up to zero and the above identity formula holds for any b. Taking $b = \frac{1}{2M}(1+c\,\delta^2)$ with another arbitrary parameter c, where $\delta = (m_M - m_B)/M$, we obtain

$$\begin{aligned} &\left(1-\frac{1}{M}\frac{\partial}{\partial t}\right)^2\left[-\nabla^2 R_\alpha(\mathbf{r},t) + 2\mu\int d^3r'\, U_{\alpha\beta}(\mathbf{r},\mathbf{r}')R_\beta(\mathbf{r}',t)\right] \\ &= \left(1-\frac{1}{M}\frac{\partial}{\partial t}\right)^2 2\mu\left[-\frac{\partial}{\partial t} + \left(\frac{1}{2M}+\frac{\delta^2}{2M}c+\frac{\delta^4}{8\mu}c\right)\frac{\partial^2}{\partial t^2}\right] R_\alpha(\mathbf{r},t) \\ &+ \delta^2\left[\left(-\frac{1}{4}c+1\right)\frac{\partial^2}{\partial t^2} - \frac{1}{M}\left(-\frac{1}{2}c+1\right)\frac{\partial^3}{\partial t^3} + \frac{1}{M^2}\left(-\frac{1}{4}c+\frac{1}{4}\right)\frac{\partial^4}{\partial t^4}\right] R_\alpha(\mathbf{r},t). \end{aligned} \tag{A.7}$$

We then decompose the potential as

$$U_{\alpha\beta}(\mathbf{r},\mathbf{r}') = U^{(0)}_{\alpha\beta}(\mathbf{r},\mathbf{r}') + U^{(1)}_{\alpha\beta}(\mathbf{r},\mathbf{r}'), \tag{A.8}$$

where $U^{(i)}_{\alpha\beta}(\mathbf{r},\mathbf{r}')$ $(i=0,1)$ are defined by the following two equations:

$$\begin{aligned} &\left[-\nabla^2 R_\alpha(\mathbf{r},t) + 2\mu\int d^3r'\, U^{(0)}_{\alpha\beta}(\mathbf{r},\mathbf{r}')R_\beta(\mathbf{r}',t)\right] \\ &= 2\mu\left[-\frac{\partial}{\partial t} + \left(\frac{1}{2M}+\frac{\delta^2}{2M}c+\frac{\delta^4}{8\mu}c\right)\frac{\partial^2}{\partial t^2}\right] R_\alpha(\mathbf{r},t), \end{aligned} \tag{A.9}$$

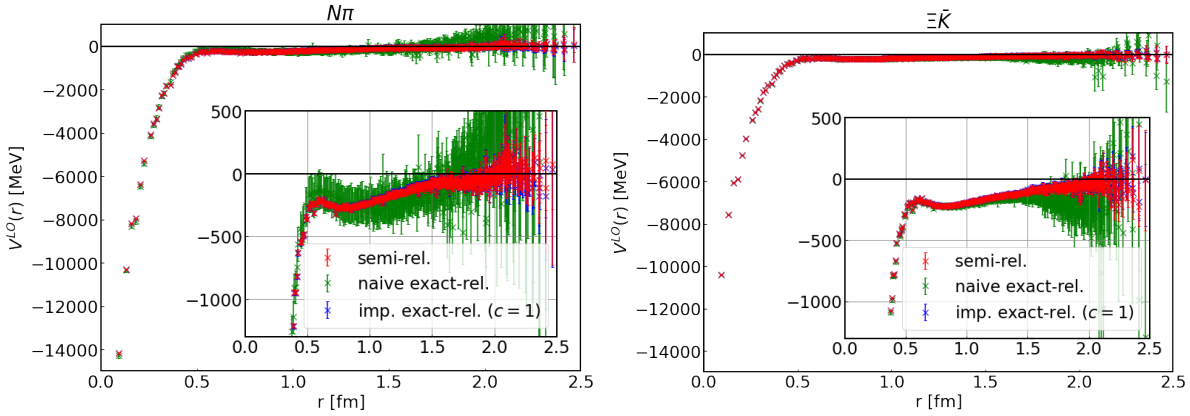

FIGURE A.1: The $N\pi$ LO potential at $t = 9$ (Left) and the $\Xi\bar{K}$ LO potential at $t = 10$ (Right) estimated from Eq. (6.7) (Red), and Eq. (A.5) (Green) and Eq. (A.11) (Blue). Note that blue points are almost invisible in the figure because they are almost the same as red points.

$$\left(1 - \frac{1}{M}\frac{\partial}{\partial t}\right)^2 2\mu \int d^3r'\, U^{(1)}_{\alpha\beta}(\mathbf{r}, \mathbf{r}') R_\beta(\mathbf{r}', t) = \delta^2 \left[\left(-\frac{1}{4}c + 1\right)\frac{\partial^2}{\partial t^2} - \frac{1}{M}\left(-\frac{1}{2}c + 1\right)\frac{\partial^3}{\partial t^3} + \frac{1}{M^2}\left(-\frac{1}{4}c + \frac{1}{4}\right)\frac{\partial^4}{\partial t^4}\right] R_\alpha(\mathbf{r}, t). \tag{A.10}$$

The LO potential in this decomposition reads

$$V^{LO}(\mathbf{r}) = V^{(0)LO}(\mathbf{r}) + V^{(1)LO}(\mathbf{r}), \tag{A.11}$$

where

$$V^{(0)LO}(\mathbf{r}) = \frac{1}{R_\alpha(\mathbf{r}, t)}\left[\left(-\frac{\partial}{\partial t} + \left(\frac{1}{2M} + \frac{\delta^2}{2M}c + \frac{\delta^4}{8\mu}c\right)\frac{\partial^2}{\partial t^2}\right) - H_0\right] R_\alpha(\mathbf{r}, t), \tag{A.12}$$

$$V^{(1)LO}(\mathbf{r}) = \frac{\delta^2\left[\left(-\frac{1}{4}c + 1\right)\frac{\partial^2}{\partial t^2} - \frac{1}{M}\left(-\frac{1}{2}c + 1\right)\frac{\partial^3}{\partial t^3} + \frac{1}{M^2}\left(-\frac{1}{4}c + \frac{1}{4}\right)\frac{\partial^4}{\partial t^4}\right] R_\alpha(\mathbf{r}, t)}{2\mu\left(1 - \frac{1}{M}\frac{\partial}{\partial t}\right)^2 R_\alpha(\mathbf{r}, t)} \tag{A.13}$$

If we set $c = 1$, the 4th-order time derivative term in Eq. (A.10) or Eq. (A.13) vanishes, so that we need only 3rd-order terms at most.

A.3 Comparison of potentials among semi-relativistic and exact-relativistic formulae for P-wave $N\pi$ and $\Xi\bar{K}$ systems

Fig. A.1 shows a comparison of the $N\pi$ and $\Xi\bar{K}$ potentials estimated from Eq. (6.7), and those from Eq. (A.5) and Eq. (A.11). For the truncation in Eq. (6.7), we set $k \leq 2$ for $N\pi$ and $k \leq 3$ for $\Xi\bar{K}$, respectively, as well as the main part of this thesis. All three results are consistent with each other within statistical errors, though results from Eq. (A.5) have larger statistical errors. These are caused by statistical fluctuations of the 4th-order time-derivative terms that appear in the numerator. The results from Eq. (6.7) and Eq. (A.11) agree with each other within

comparable errors, which indicates that systematic uncertainties for the truncation in Eq. (6.7) are well under control.

Appendix B

Singular behaviors of the $N\pi$ LO potential and smeared sink quark operators

B.1 $N\pi$ LO potential with point sink quarks

We have sometimes observed singular behavior of a potential between two hadrons in the HAL QCD method if the n-point correlation function has quark pair creation and annihilation diagrams. As an example, we show in Fig. B.1 (Left) a real part of the normalized 3-point function in the P-wave $I = 3/2$ $N\pi$ system for point sink quark operators in our trial calculation using $2+1$-flavor configurations by the CP-PACS and JLQCD Collaborations [85] at $a \approx 0.12$ fm and $m_\pi \approx 870$ MeV on $16^3 \times 32$ lattice volume. Then the corresponding LO potential, shown in Fig. B.1 (Right), has multi-valued behavior in a short distance. As discussed below, this is due to a complicated structure with rapid changes around the origin of the 3-point correlation function, rather than contaminations of higher partial waves due to a cubic box (long-distance effects). Due to quark pair creation and annihilation which is possible in this channel, the operator-product expansion (OPE) [76–79] predicts the following behavior of the 3-point function at $r \to 0$:

$$F(\mathbf{r}) \propto \frac{1}{r^3} Y_m^l(\Omega), \tag{B.1}$$

where $Y_m^l(\Omega)$ is the spherical harmonics with the angular momentum of the system. We find that the behavior of Eq. (B.1) for $l = 1$ at short distances looks very similar to a plot in Fig.B.1 (Left). Also, the discretized one of the following quantities:

$$\frac{\nabla^2(\frac{1}{r^3} Y_m^l(\Omega))}{\frac{1}{r^3} Y_m^l(\Omega)}, \tag{B.2}$$

which is associated with the laplacian part of the LO potential Eq. (3.64), also becomes multi-valued if the number of discrete data at short distances is too small to reproduce a smooth single-valued behavior. Thus the problem is caused by short-distance discretization effects. Note that a similar singular behavior was already observed in the $I = 1$ P-wave $\pi\pi$ system [22].

One of the possible prescriptions to tame singular behaviors at short distances is the sink smearing at the quark level, which is proposed in Ref. [22]. This corresponds to replacing the sink quark operators with the smeared ones in the NBS wave function, which does not change the physical observables in principle. Fig. B.2 (Left) represents the 3-point function with smeared sink quark operator, while Fig.B.2 (Right) is the corresponding potential. As expected, sink smearings make the behavior of the NBS wave function at short distances much smoother, so

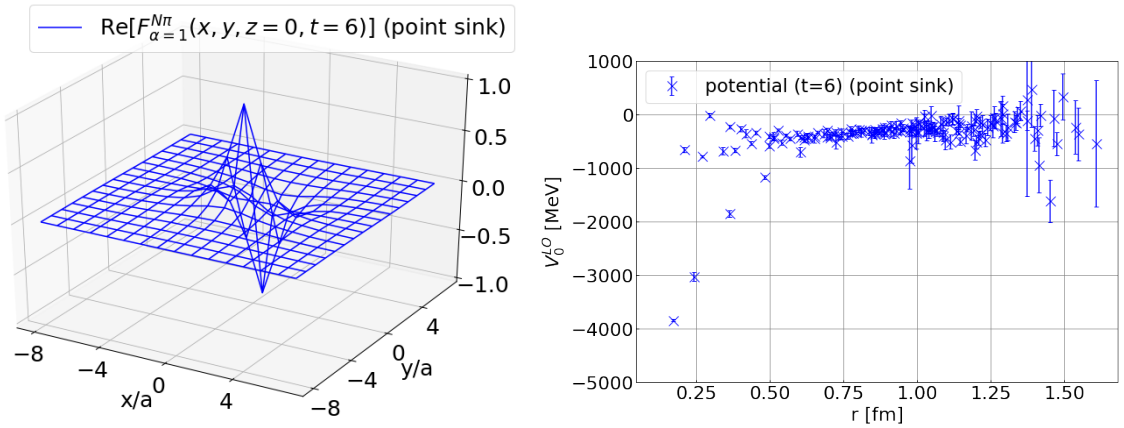

FIGURE B.1: (Left) An upper component ($\alpha = 1$) of the $N\pi$ 3-point function at $t = 6$ and $z = 0$ for point sink quark operators. The function is normalized so that its maximum value is 1. (Right) The corresponding LO potential.

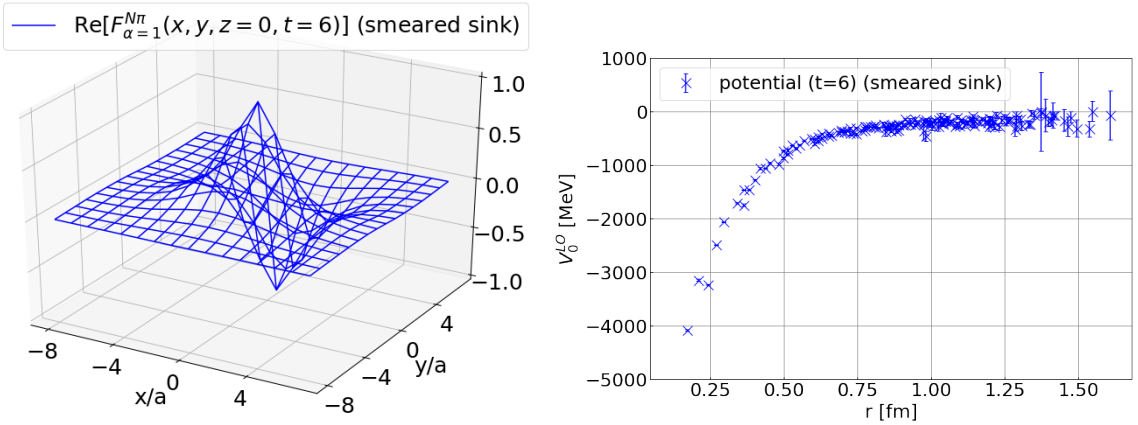

FIGURE B.2: Same as Fig. B.1 but for smeared sink quark operators.

that the potential becomes almost single-valued even at short distances where discrete data points are sparsely located.

B.2 Non-locality effect of sink smearing on the potentials

Although smeared sink operators suppress singular behaviors in potentials at short distances, they may enhance the higher-order terms in the derivative expansion of non-local potentials. This may cause large systematic errors in the LO analysis, as was observed in the case of the LapH method [86]. In order to quantify effects of the non-locality caused by our sink smearing, we compare phase shifts of $I = 1$ S-wave $\Xi\bar{K}$ scattering between point and smeared sink operators in the same setup as in Chapter 5.

Comparisons in Fig. B.3 show that they agree with each other at $\Delta E \lesssim 100$ MeV, where ΔE is an energy difference from the threshold. This suggests that the non-locality effect due to the sink smearing is negligible for physical observables in the low-energy region in this setup.

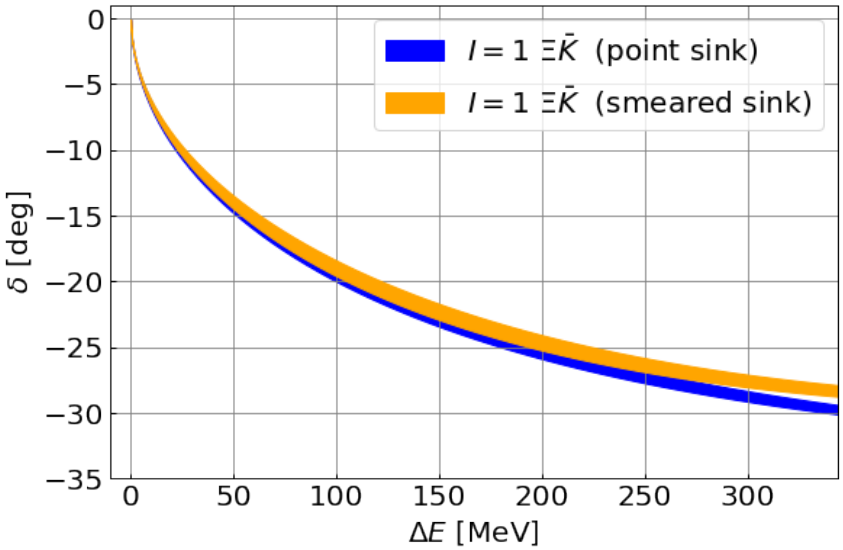

FIGURE B.3: Phase shifts in $I = 1$ $\Xi\bar{K}$ system calculated form potentials at $t = 8$. Blue (orange) bands show results with point (smeared) sink operators.

Appendix C

Rotational symmetry on a lattice

In this appendix, we review the cubic group, which is the discrete rotational symmetry on a three-dimensional isotropic lattice. We first show its conjugate classes and irreducible representations, then present the transformation properties of several hadron operators under the cubic group. Then we define the states and operators which belong to the irreducible representations. Finally, we explain how to project states and operators onto specific representations and the explicit projection of meson-baryon operators utilized in the main part of this thesis.

C.1 Cubic group and its irreducible representations

In the continuum, QCD has three-dimensional rotational symmetry, but the lattice QCD does not. It instead has a symmetry under which a three-dimensional cube does not change, which is called the cubic group or the octahedral group O [87]. O has 24 elements and is classified by five conjugate classes as follows:

- identity: I,
- π rotations along 3 lattice axes: $3C_2$,
- $\pm 2\pi/3$ rotations along 4 space diagonals: $8C_3$,
- $\pm\pi/2$ rotations along 3 lattice axis: $6C_4$,
- $\pm\pi$ rotations along 6 face diagonals: $6C_2'$.

Each conjugate class is shown graphically in Figure C.1. Since the number of the conjugate classes is equal to that of the irreducible representations (IRs), O has five IRs called A_1, A_2, E, T_1, and T_2. The dimensions of the IRs are 1, 1, 2, 3, and 3, respectively.

We consider the spin degree of freedom by introducing the double cover of the cubic group, called O^D. O^D has the same elements as those of O except for an additional action of 2π rotation, which corresponds to multiplying a factor -1 to states with spin in the continuum. O^D thus has 48 elements. The conjugate classes of the double cover of the cubic group O^D are as follows:

- identity: I,
- 2π rotation: J
- π rotations about 3 lattice axes: $6C_4$,
- $\pm 4\pi/3$ rotations about 4 space diagonals: $8C_3$,

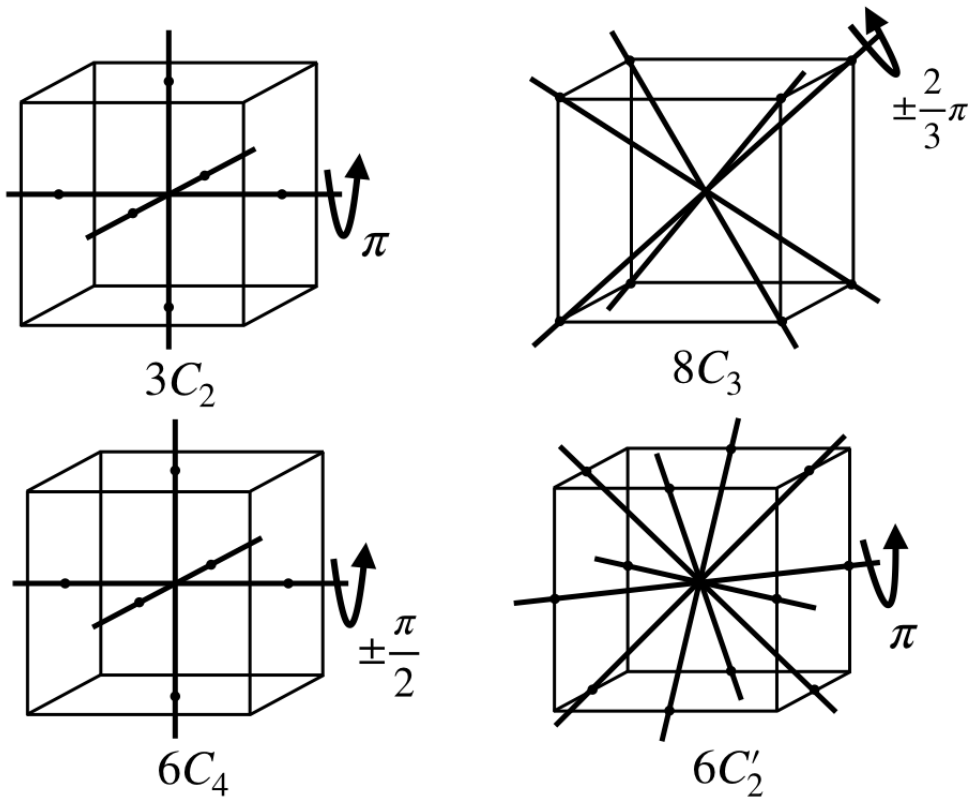

FIGURE C.1: Rotations classified by the conjugate classes.

- $\pm 2\pi/3$ rotations about 4 space diagonals: $8C_6$,
- $\pm 3\pi/2$ rotations about 3 lattice axis: $6C_8$,
- $\pm\pi/2$ rotations 3 lattice axis: $6C_8'$,
- $\pm\pi$ rotations about 6 face diagonals: $12C_4'$.

Here $-\theta$ rotation is identified with $4\pi - \theta$ rotation. Therefore, $8C_3$ and $6C_8$ are same as 2π rotation followed by $8C_6$ and $6C_8'$, respectively. O^D includes the same five IRs of O, which corresponds to spin-integer states, with additional ones called G_1, G_2, and H, which are associated with spin-half-integer states.

QCD also has the parity reflection symmetry I. The double cover of the cubic group together with the reflection, called O_h^D, has 96 elements and 8 additional conjugate classes. The IR of O_h^D are represented as X^P, where X is the IRs of O^D and $P = +$ ($P = -$) denotes parity even (odd).

C.2 Transformation properties of the hadron operators for the cubic group

Here we briefly review the transformation properties of several hadron operators under O_h^D. Here we abbreviate the time component of operators. The pseudo-scalar meson operator with

momentum $\mathbf{p}$ is given by

$$M(\mathbf{p}) = \sum_{\mathbf{x}} \bar{q}(\mathbf{x})\gamma_5 q(\mathbf{x}) e^{i\mathbf{p}\cdot\mathbf{x}}, \tag{C.1}$$

and the octet and decuplet baryon operator by

$$B_\alpha(\mathbf{p}) = \sum_x \epsilon_{abc} q_{a,\alpha}(\mathbf{x})(q_b^{\mathrm{T}}(\mathbf{x})C\gamma_5 q_c(\mathbf{x}))e^{i\mathbf{p}\cdot\mathbf{x}}, \tag{C.2}$$

$$D_{\alpha,i}(\mathbf{p}) = \sum_x \epsilon_{abc} q_{a,\alpha}(\mathbf{x})(q_b^{\mathrm{T}}(\mathbf{x})C\gamma_i q_c(\mathbf{x}))e^{i\mathbf{p}\cdot\mathbf{x}}, \tag{C.3}$$

where $q_{a,\alpha}(\mathbf{x})$ and $\bar{q}_{a,\alpha}(\mathbf{x})$ are the quark operators, C is the charge conjugation matrix acting on the spinor space, and γ_i ($i = 1, 2, 3$) are gamma matrix in the spatial direction.

$M(\mathbf{p})$, $B_{a,\alpha}(\mathbf{p})$ and $D_{\alpha,i}(\mathbf{p})$ transform under rotation R and parity refrection I as

$$\begin{aligned}
U_R M(\mathbf{p})U_R^\dagger &= M(R\mathbf{p}), \quad U_I M(\mathbf{p})U_I^\dagger = -M(-\mathbf{p}), \\
U_R B_\alpha(\mathbf{p})U_R^\dagger &= S(R)^{-1}_{\alpha\beta} B_\beta(R\mathbf{p}), \quad U_I B_\alpha(\mathbf{p})U_I^\dagger = (\gamma_4)_{\alpha\beta} B_\beta(-\mathbf{p}), \\
U_R D_{\alpha,i}(\mathbf{p})U_R^\dagger &= A(R)^{-1}_{ij} S(R)^{-1}_{\alpha\beta} D_{\beta,j}(R\mathbf{p}), \quad U_I D_{\alpha,i}(\mathbf{p})U_I^\dagger = (\gamma_4)_{\alpha\beta} D_{\beta,i}(-\mathbf{p}),
\end{aligned} \tag{C.4}$$

where U_R and U_I are the unitary operators on the Hilbert space, $S(R)_{\alpha\beta}$ is the 4×4 rotation matrix acting on the spinors, and $A(R)_{ij}$ is the 3×3 rotation matrix acting on the index of the gamma matrices.

For a rotation with the axis $\mathbf{n} = (n_1, n_2, n_3)$ ($|\mathbf{n}| = 1$) and the angle θ, $R\mathbf{p}$ is represented as

$$\begin{pmatrix}
n_1^2(1-\cos\theta)+\cos\theta & n_1 n_2(1-\cos\theta)-n_3\sin\theta & n_1 n_3(1-\cos\theta)+n_2\sin\theta \\
n_1 n_2(1-\cos\theta)+n_3\sin\theta & n_2^2(1-\cos\theta)+\cos\theta & n_2 n_3(1-\cos\theta)-n_1\sin\theta \\
n_1 n_3(1-\cos\theta)-n_2\sin\theta & n_2 n_3(1-\cos\theta)+n_1\sin\theta & n_3^2(1-\cos\theta)+\cos\theta
\end{pmatrix}
\begin{pmatrix} p_1 \\ p_2 \\ p_3 \end{pmatrix}, \tag{C.5}$$

and $S(R)_{\alpha\beta}$ and $A(R)_{ij}$ are described as

$$S(R) = \exp\left(\frac{1}{8}\omega_{\mu\nu}[\gamma_\mu, \gamma_\nu]\right), \quad A(R) = \exp(-i\theta\mathbf{n}\cdot\mathbf{J}), \tag{C.6}$$

where $\omega_{jk} = -\epsilon_{ijk} n_i \theta$ and $\omega_{04} = \omega_{40} = 0$, and $(\mathbf{J}_k)_{ij} = -i\varepsilon_{ijk}$ with the total antisymmetric tensor ε_{ijk}. Note that the matrix in Eq. (C.5) and $A(R)$ are identical. In particular, in the Dirac representation, the upper two spinor components $B_s(\mathbf{p})$ and $D_{s,i}(\mathbf{p})$ ($s = \text{up}, \text{down}$) transform as

$$\begin{aligned}
U_R B_s(\mathbf{p})U_R^\dagger &= \exp\left(i\theta\mathbf{n}\cdot\frac{\boldsymbol{\sigma}}{2}\right)_{ss'} B_{s'}(R\mathbf{p}), \quad U_I B_s(p)U_I^\dagger = B_s(-\mathbf{p}), \\
U_R D_{s,i}(\mathbf{p})U_R^\dagger &= \exp(i\theta\mathbf{n}\cdot\mathbf{J})_{ij} \exp\left(i\theta\mathbf{n}\cdot\frac{\boldsymbol{\sigma}}{2}\right)_{ss'} D_{s',j}(R\mathbf{p}), \quad U_I D_{s,i}(\mathbf{p})U_I^\dagger = D_{s,i}(-\mathbf{p}),
\end{aligned} \tag{C.7}$$

where σ_i is the Pauli matrix.

C.3 States and operators in the IR of O_h^D

A state that belongs to IR Γ^P with rth-component (basis) $\left|\Gamma^P, r\right\rangle$ is defined by

$$U_g \left|\Gamma^P, r\right\rangle = \sum_{r'} T^{\Gamma^P}_{r',r}(g) \left|\Gamma^P, r'\right\rangle, \tag{C.8}$$

where U_g is the unitary operator of $g \in O_h^D$ on the Hilbert space and $T^{\Gamma^P}_{r',r}(g)$ is the representation matrix. For example, for a rotation R, $T^{A_1^\pm}(R) = 1$ and $T^{T_1^\pm}_{r',r}(R) = \exp\left(-i\theta^{(R)}\mathbf{n}^{(R)} \cdot \mathbf{J}\right)_{r'r}$, where $\theta^{(R)}$ and $\mathbf{n}^{(R)}$ denote the rotation angle and axis of R, respectively, and $(\mathbf{J}_q)_{r'r} = -i\varepsilon_{r'rq}$ (For the other IRs, see, for example, Appendix A in [88]). For a parity reflection I, $T^{X^\pm}(I) = \pm 1$ for every IR. An operator in the IR Γ^P with the component r is defined as

$$U_g O_{\Gamma^P,r} U_g^\dagger = \sum_{r'} T^{\Gamma^P}_{r,r'}(g^{-1}) O_{\Gamma^P,r'}, \tag{C.9}$$

so that $O^\dagger_{\Gamma^P,r} \left|0\right\rangle$ has the same transformation as $\left|\Gamma^P, r\right\rangle$.

C.4 Projection method

Here we explain the projection of a state $\left|\mathbf{p}\right\rangle$ and an operator $O(\mathbf{p})$ with momentum $\mathbf{p}$ onto specific IR and component [89]. The same technique also can be applied to a state and operator with specific spatial coordinates $\mathbf{x}$. We obtain the states and the operators in the IR Γ^P and row r by the projection as

$$\left|\Gamma^P, r; \mathbf{p}\right\rangle = \frac{d_{\Gamma^P}}{n_{O_h^D}} \sum_{g \in O_h^D} T^{\Gamma^P}_{r,r}(g^{-1})\, U_g \left|\mathbf{p}\right\rangle, \tag{C.10}$$

$$O_{\Gamma^P,r}(\mathbf{p}) = \frac{d_{\Gamma^P}}{n_{O_h^D}} \sum_{g \in O_h^D} T^{\Gamma^P}_{r,r}(g)\, U_g O(\mathbf{p}) U_g^\dagger, \tag{C.11}$$

where r is not summed over. The proof is as follows. According to the completeness relation, $\left|\mathbf{p}\right\rangle$ and $O(\mathbf{p})$ is decomposed into $\left|\Gamma^P, r\right\rangle$ and $O_{\Gamma^P,r}$, respectively as

$$\left|\mathbf{p}\right\rangle = \sum_{\Gamma^P,r} c_{\Gamma^P,r}(\mathbf{p}) \left|\Gamma^P, r\right\rangle, \tag{C.12}$$

$$O(\mathbf{p}) = \sum_{\Gamma^P,r} C_{\Gamma^P,r}(\mathbf{p}) O_{\Gamma^P,r}, \tag{C.13}$$

where $c_{\Gamma^P,r}(p)$ and $C_{\Gamma^P,r}(p)$ are the coefficients. Thus using Eq. (C.8), the right hand side of Eq. (C.10) reads

$$\begin{aligned}
&\sum_{\Gamma^{P'},r'} c_{\Gamma^{P'},r'}(p)\frac{d_{\Gamma^P}}{n_{O_h^D}}\sum_{g\in O_h^D} T^{\Gamma^P}_{r,r}(g^{-1})\, U_g \left|\Gamma^{P'},r'\right\rangle \\
=&\sum_{\Gamma^{P'},r'} c_{\Gamma^{P'},r'}(p)\frac{d_{\Gamma^P}}{n_{O_h^D}}\sum_{g\in O_h^D} T^{\Gamma^P}_{r,r}(g^{-1})\sum_{r''} T^{\Gamma^{P'}}_{r'',r'}(g)\left|\Gamma^{P'},r''\right\rangle \\
=&\sum_{\Gamma^{P'},r'} c_{\Gamma^{P'},r'}(p)\sum_{r''}\underbrace{\frac{d_{\Gamma^P}}{n_{O_h^D}}\sum_{g\in O_h^D} T^{\Gamma^{P'}}_{r'',r'}(g)T^{\Gamma^P}_{r,r}(g^{-1})}_{=\delta_{\Gamma^{P'},\Gamma^P}\delta_{r'',r}\delta_{r',r}}\left|\Gamma^{P'},r''\right\rangle \\
=&c_{\Gamma^P,r}(p)\left|\Gamma^P,r\right\rangle .
\end{aligned} \tag{C.14}$$

Here, from the second to the third line, we use the orthogonal relation of $T^{\Gamma^P}_{r,r'}(g)$. Similarly, using Eq. (C.9), the right-hand side of Eq. (C.11) reads

$$\begin{aligned}
&\sum_{\Gamma^{P'},r'} C_{\Gamma^{P'},r'}(p)\frac{d_{\Gamma^P}}{n_{O_h^D}}\sum_{g\in O_h^D} T^{\Gamma^P}_{r,r}(g)\, U_g O_{\Gamma^{P'},r'}U_g^\dagger \\
=&\sum_{\Gamma^{P'},r'} c_{\Gamma^{P'},r'}(p)\frac{d_{\Gamma^P}}{n_{O_h^D}}\sum_{g\in O_h^D} T^{\Gamma^P}_{r,r}(g)\sum_{r''} T^{\Gamma^{P'}}_{r',r''}(g^{-1})O_{\Gamma^{P'},r''} \\
=&\sum_{\Gamma^{P'},r'} c_{\Gamma^{P'},r'}(p)\sum_{r''}\underbrace{\frac{d_{\Gamma^P}}{n_{O_h^D}}\sum_{g\in O_h^D} T^{\Gamma^P}_{r,r}(g)T^{\Gamma^{P'}}_{r',r''}(g^{-1})}_{=\delta_{\Gamma^P,\Gamma^{P'}}\delta_{r,r''}\delta_{r,r'}} O_{\Gamma^{P'},r''} \\
=&C_{\Gamma^P,r}(p)O_{\Gamma^P,r}.
\end{aligned} \tag{C.15}$$

Therefore, Eq. (C.10) and Eq. (C.11) provide the appropriate projections.

Furthermore, taking summations of Eq. (C.10) and Eq. (C.11) over r, we obtain

$$\left|\Gamma^P;p\right\rangle = \frac{d_{\Gamma^P}}{n_{O_h^D}}\sum_{g\in O_h^D}\chi_{\Gamma^P}(g)\, U_g\left|p\right\rangle , \tag{C.16}$$

$$O_{\Gamma^P}(p) = \frac{d_{\Gamma^P}}{n_{O_h^D}}\sum_{g\in O_h^D}\chi_{\Gamma^P}(g)\, U_g O(p) U_g^\dagger, \tag{C.17}$$

where $\chi_{\Gamma^P}(g)=\sum_r T^{\Gamma^P}_{r,r}(g)=\sum_r T^{\Gamma^P}_{r,r}(g^{-1})$, called character. These equations also represent the projected states and operators onto the IR Γ^P, but the component r cannot be specified. Nevertheless, these are useful since the different elements in the same conjugate class share the same value of $\chi_{\Gamma^P}(g)$. The character in each conjugate class for O_h^D is listed in Table.1 of [87]),

The explicit form of the projected meson-baryon operator in the momentum space is represented as

$$\begin{aligned} O^{MB}_{\Gamma^P,r}(\mathbf{p}) &= \frac{d_{\Gamma^P}}{n_{O_h^D}} \sum_{g\in O_h^D} T^{\Gamma^P}_{r,r}(g)\; U_g M(-\mathbf{p}) B_\alpha(\mathbf{p}) U_g^\dagger \\ &= \frac{d_{\Gamma^P}}{n_{O_h^D}} \sum_{R\in O^D} \left[T^{\Gamma^P}_{r,r}(R)\; U_R M(-\mathbf{p}) B_\alpha(\mathbf{p}) U_R^\dagger + (-1)^P T^{\Gamma^P}_{r,r}(R)\; U_R(-M(\mathbf{p})) B_\alpha(-\mathbf{p}) U_R^\dagger \right] \\ &= \frac{d_{\Gamma^P}}{n_{O_h^D}} \sum_{R\in O^D} T^{\Gamma^P}_{r,r}(R) \exp\!\left(i\theta \mathbf{n}\cdot\frac{\boldsymbol{\sigma}}{2}\right)_{\alpha\beta} \left[M(-R\mathbf{p}) B_\beta(R\mathbf{p}) + (-1)^{P+1} M(R\mathbf{p}) B_\beta(-R\mathbf{p}) \right], \end{aligned} \tag{C.18}$$

and the operator in the real space is described as

$$\begin{aligned} O^{MB}_{\Gamma^P,r}(\mathbf{x}) &= \frac{d_{\Gamma^P}}{n_{O_h^D}} \sum_{g\in O_h^D} T^{\Gamma^P}_{r,r}(g)\; U_g M(\mathbf{x}) B_\alpha(\mathbf{0}) U_g^\dagger \\ &= \frac{d_{\Gamma^P}}{n_{O_h^D}} \sum_{R\in O^D} T^{\Gamma^P}_{r,r}(R) \exp\!\left(i\theta \mathbf{n}\cdot\frac{\boldsymbol{\sigma}}{2}\right)_{\alpha\beta} \left[M(R\mathbf{x}) B_\beta(\mathbf{0}) + (-1)^{P+1} M(-R\mathbf{x}) B_\beta(\mathbf{0}) \right]. \end{aligned} \tag{C.19}$$

The representation matrix of $H^\pm$ IR, which corresponds to spin-3/2, is given by

$$T^{H^\pm}(R) = \exp\!\left(-i\theta \mathbf{n}\cdot \mathbf{J}^{3/2}\right) \tag{C.20}$$

with

$$\begin{aligned} J_x^{3/2} &= \frac{1}{2}\begin{bmatrix} 0 & \sqrt{3} & 0 & 0 \\ \sqrt{3} & 0 & 2 & 0 \\ 0 & 2 & 0 & \sqrt{3} \\ 0 & 0 & \sqrt{3} & 0 \end{bmatrix}, \quad J_y^{3/2} = \frac{1}{2}\begin{bmatrix} 0 & -i\sqrt{3} & 0 & 0 \\ i\sqrt{3} & 0 & -2i & 0 \\ 0 & 2i & 0 & -i\sqrt{3} \\ 0 & 0 & i\sqrt{3} & 0 \end{bmatrix}, \\ J_z^{3/2} &= \frac{1}{2}\begin{bmatrix} 3 & 0 & 0 & 0 \\ 0 & 1 & 0 & 0 \\ 0 & 0 & -1 & 0 \\ 0 & 0 & 0 & -3 \end{bmatrix}. \end{aligned} \tag{C.21}$$

Equation (C.19) together with Eq. (C.21) are used in the main part of this thesis.

Bibliography

[1] C.-N. Yang and R. L. Mills, Phys. Rev. **96**, edited by J.-P. Hsu and D. Fine, 191 (1954).

[2] D. J. Gross and F. Wilczek, Phys. Rev. Lett. **30**, edited by J. C. Taylor, 1343 (1973).

[3] H. D. Politzer, Phys. Rev. Lett. **30**, edited by J. C. Taylor, 1346 (1973).

[4] M. Gell-Mann, Phys. Lett. **8**, 214 (1964).

[5] G. Zweig, "An SU(3) model for strong interaction symmetry and its breaking. Version 2", in *DEVELOPMENTS IN THE QUARK THEORY OF HADRONS. VOL. 1. 1964 - 1978*, edited by D. B. Lichtenberg and S. P. Rosen (Feb. 1964), pp. 22–101.

[6] G. Zweig, (1964).

[7] S. Weinberg, Physica A **96**, edited by S. Deser, 327 (1979).

[8] Y.-R. Liu, H.-X. Chen, W. Chen, X. Liu, and S.-L. Zhu, Prog. Part. Nucl. Phys. **107**, 237 (2019).

[9] K. G. Wilson, Phys. Rev. D **10**, edited by J. C. Taylor, 2445 (1974).

[10] S. Durr et al., Science **322**, 1224 (2008).

[11] S. Aoki et al., Phys. Rev. D **79**, 034503 (2009).

[12] M. Luscher, Nucl. Phys. B **354**, 531 (1991).

[13] K. Rummukainen and S. A. Gottlieb, Nucl. Phys. B **450**, 397 (1995).

[14] N. Ishii, S. Aoki, and T. Hatsuda, Phys. Rev. Lett. **99**, 022001 (2007).

[15] S. Aoki, T. Hatsuda, and N. Ishii, Prog. Theor. Phys. **123**, 89 (2010).

[16] N. Ishii, S. Aoki, T. Doi, T. Hatsuda, Y. Ikeda, T. Inoue, K. Murano, H. Nemura, and K. Sasaki, Phys. Lett. B **712**, 437 (2012).

[17] S. Aoki et al., Phys. Rev. D **76**, 094506 (2007).

[18] T. Iritani, S. Aoki, T. Doi, T. Hatsuda, Y. Ikeda, T. Inoue, N. Ishii, H. Nemura, and K. Sasaki, JHEP **03**, 007 (2019).

[19] S. Aoki and T. Doi, Front. in Phys. **8**, 307 (2020).

[20] D. Kawai, EPJ Web Conf. **175**, edited by M. Della Morte, P. Fritzsch, E. Gámiz Sánchez, and C. Pena Ruano, 05007 (2018).

[21] Y. Akahoshi, S. Aoki, T. Aoyama, T. Doi, T. Miyamoto, and K. Sasaki, PTEP **2020**, 073B07 (2020).

[22] Y. Akahoshi, S. Aoki, and T. Doi, Phys. Rev. D **104**, 054510 (2021).

[23] C. Gattringer and C. B. Lang, *Quantum chromodynamics on the lattice*, Vol. 788 (Springer, Berlin, 2010).

[24] H. B. Nielsen and M. Ninomiya, Nucl. Phys. B **185**, edited by J. Julve and M. Ramón-Medrano, [Erratum: Nucl.Phys.B 195, 541 (1982)], 20 (1981).

[25] H. B. Nielsen and M. Ninomiya, Phys. Lett. B **105**, 219 (1981).

[26] H. B. Nielsen and M. Ninomiya, Nucl. Phys. B **193**, 173 (1981).

[27] P. H. Ginsparg and K. G. Wilson, Phys. Rev. D **25**, 2649 (1982).

[28] H. Neuberger, Phys. Lett. B **417**, 141 (1998).

[29] K. Symanzik, Nucl. Phys. B **226**, 187 (1983).

[30] K. Symanzik, Nucl. Phys. B **226**, 205 (1983).

[31] B. Sheikholeslami and R. Wohlert, Nucl. Phys. B **259**, 572 (1985).

[32] Y. Iwasaki, (1983).

[33] Y. Iwasaki, Nucl. Phys. B **258**, 141 (1985).

[34] S. Duane and J. B. Kogut, Phys. Rev. Lett. **55**, 2774 (1985).

[35] S. Duane and J. B. Kogut, Nucl. Phys. B **275**, 398 (1986).

[36] P. de Forcrand and T. Takaishi, Nucl. Phys. B Proc. Suppl. **53**, edited by C. Bernard, M. Golterman, M. Ogilvie, and J. Potvin, 968 (1997).

[37] R. Frezzotti and K. Jansen, Phys. Lett. B **402**, 328 (1997).

[38] T. Takaishi and P. de Forcrand, Int. J. Mod. Phys. C **13**, 343 (2002).

[39] A. D. Kennedy, I. Horvath, and S. Sint, Nucl. Phys. B Proc. Suppl. **73**, edited by T. A. DeGrand, C. E. DeTar, R. Sugar, and D. Toussaint, 834 (1999).

[40] M. A. Clark and A. D. Kennedy, Nucl. Phys. B Proc. Suppl. **129**, edited by S. Aoki, S. Hashimoto, N. Ishizuka, K. Kanaya, and Y. Kuramashi, 850 (2004).

[41] M. A. Clark, P. de Forcrand, and A. D. Kennedy, PoS **LAT2005**, edited by C. Michael, 115 (2006).

[42] M. A. Clark, PoS **LAT2006**, edited by T. Blum, M. Creutz, C. DeTar, F. Karsch, A. Kronfeld, C. Morningstar, D. Richards, J. Shigemitsu, and D. Toussaint, 004 (2006).

[43] T. Iritani et al., JHEP **10**, 101 (2016).

[44] S. Weinberg, *The quantum theory of fields*, Vol. 1 (Cambridge University Press, 1995).

[45] S. Aoki, N. Ishii, T. Doi, Y. Ikeda, and T. Inoue, Phys. Rev. D **88**, 014036 (2013).

[46] S. Okubo and R. E Marshak, Annals Phys. **4**, 166 (1958).

[47] M. Foster and C. Michael, Phys. Rev. D **59**, 074503 (1999).

[48] C. McNeile and C. Michael, Phys. Lett. B **556**, 177 (2003).

[49] J. Foley, K. Jimmy Juge, A. O'Cais, M. Peardon, S. M. Ryan, and J.-I. Skullerud, Comput. Phys. Commun. **172**, 145 (2005).

[50] E. Shintani, R. Arthur, T. Blum, T. Izubuchi, C. Jung, and C. Lehner, Phys. Rev. D **91**, 114511 (2015).

[51] G. S. Bali, S. Collins, and A. Schafer, Comput. Phys. Commun. **181**, 1570 (2010).

[52] M. Fukugita, Y. Kuramashi, M. Okawa, H. Mino, and A. Ukawa, Phys. Rev. D **52**, 3003 (1995).

[53] G.-w. Meng, C. Miao, X.-n. Du, and C. Liu, Int. J. Mod. Phys. A **19**, 4401 (2004).

[54] A. Torok, S. R. Beane, W. Detmold, T. C. Luu, K. Orginos, A. Parreno, M. J. Savage, and A. Walker-Loud, Phys. Rev. D **81**, 074506 (2010).

[55] W. Detmold and A. N. Nicholson, Phys. Rev. D **88**, 074501 (2013).

[56] W. Detmold and A. Nicholson, Phys. Rev. D **93**, 114511 (2016).

[57] Y. Ikeda, S. Aoki, T. Doi, T. Hatsuda, T. Inoue, N. Ishii, K. Murano, H. Nemura, and K. Sasaki, EPJ Web Conf. **3**, edited by E. Epelbaum, H. W. Hammer, and U.-G. Meissner, 03007 (2010).

[58] Y. Ikeda, PoS **LATTICE2011**, edited by P. Vranas, 159 (2011).

[59] T. Nakano et al., Phys. Rev. Lett. **91**, 012002 (2003).

[60] P. Zyla et al., PTEP **2020**, and 2021 update, 083C01 (2020).

[61] Y. Akahoshi, S. Aoki, T. Aoyama, T. Doi, T. Miyamoto, and K. Sasaki, PTEP **2019**, 083B02 (2019).

[62] INS GW Data Analysis Center [SAID], `http://gwdac.phys.gwu.edu/`.

[63] T. Barnes and E. S. Swanson, Phys. Rev. C **49**, 1166 (1994).

[64] C. Alexandrou, J. W. Negele, M. Petschlies, A. Strelchenko, and A. Tsapalis, Phys. Rev. D **88**, 031501 (2013).

[65] C. Alexandrou, J. W. Negele, M. Petschlies, A. V. Pochinsky, and S. N. Syritsyn, Phys. Rev. D **93**, 114515 (2016).

[66] C. W. Andersen, J. Bulava, B. Hörz, and C. Morningstar, Phys. Rev. D **97**, 014506 (2018).

[67] S. Paul et al., PoS **LATTICE2018**, 089 (2018).

[68] C. W. Andersen, J. Bulava, B. Hörz, and C. Morningstar, PoS **LATTICE2019**, 039 (2019).

[69] G. Silvi et al., Phys. Rev. D **103**, 094508 (2021).

[70] J. Bulava, A. D. Hanlon, B. Hörz, C. Morningstar, A. Nicholson, F. Romero-López, S. Skinner, P. Vranas, and A. Walker-Loud, (2022).

[71] E. Hiyama, Y. Kino, and M. Kamimura, Prog. Part. Nucl. Phys. **51**, 223 (2003).

[72] J. A. Oller and U. G. Meissner, Phys. Lett. B **500**, 263 (2001).

[73] D. Jido, J. A. Oller, E. Oset, A. Ramos, and U. G. Meissner, Nucl. Phys. A **725**, 181 (2003).

[74] J. J. de Swart, Rev. Mod. Phys. **35**, [Erratum: Rev.Mod.Phys. 37, 326–326 (1965)], 916 (1963).

[75] T. Inoue, PoS **CD15**, 020 (2016).

[76] S. Aoki, J. Balog, and P. Weisz, PoS **LAT2009**, edited by C. Liu and Y. Zhu, 132 (2009).

[77] S. Aoki, J. Balog, and P. Weisz, JHEP **05**, 008 (2010).

[78] S. Aoki, J. Balog, and P. Weisz, JHEP **09**, 083 (2010).

[79] S. Aoki, J. Balog, T. Doi, T. Inoue, and P. Weisz, Int. J. Mod. Phys. E **22**, 1330012 (2013).

[80] T. Amagasa et al., J. Phys. Conf. Ser. **664**, 042058 (2015).

[81] S. Ueda, S. Aoki, T. Aoyama, K. Kanaya, H. Matsufuru, S. Motoki, Y. Namekawa, H. Nemura, Y. Taniguchi, and N. Ukita, J. Phys. Conf. Ser. **523**, edited by J. Wang, 012046 (2014).

[82] http://bridge.kek.jp/Lattice-code/.

[83] I. Kanamori and H. Matsufuru, in (Nov. 2018).

[84] N. Ishii et al., PoS **LATTICE2015**, 087 (2016).

[85] T. Ishikawa et al., Phys. Rev. D **78**, 011502 (2008).

[86] D. Kawai, S. Aoki, T. Doi, Y. Ikeda, T. Inoue, T. Iritani, N. Ishii, T. Miyamoto, H. Nemura, and K. Sasaki, PTEP **2018**, 043B04 (2018).

[87] R. C. Johnson, Phys. Lett. B **114**, 147 (1982).

[88] V. Bernard, M. Lage, U.-G. Meissner, and A. Rusetsky, JHEP **08**, 024 (2008).

[89] S. Prelovsek, U. Skerbis, and C. B. Lang, JHEP **01**, 129 (2017).